UNCLASSIFIED

AD NUMBER

AD813906

NEW LIMITATION CHANGE

TO

Approved for public release, distribution unlimited

FROM

Distribution authorized to U.S. Gov't. agencies and their contractors; Critical Technology; JAN 1967. Other requests shall be referred to Air Force Rocket Propulsion Laboratory, Attn: RPPR-STINFO, Edwards AFB, CA 93523.

AUTHORITY

AFRPL ltr, 20 Dec 1971

THIS PAGE IS UNCLASSIFIED

Form 1473

(18) AFRPL (14) TR-66-350

(14) LPC-[redacted]751-F

AD 813906

(6) 156-INCH DIAMETER MARAGING STEEL CASE
HYDROBURST AND MATERIALS EVALUATION.

(9) Final technical rept. Mar — Dec 66,

~~Lockheed Propulsion Company~~
~~Redlands, California~~

TECHNICAL REPORT NO. AFRPL-TR-66-350

(11) Jan[redacted]67

(12) 152p.

(10) J. S. Coverdale,
Norbert Wells,
Gilbert Skopp
George Broeker

Air Force Rocket Propulsion Laboratory
Research and Technology Division
Air Force Systems Command
United States Air Force
Edwards, California

(15) AF 04(611)-11615

STATEMENT #2 UNCLASSIFIED

This document is subject to special export controls and each transmittal to foreign governments or foreign nationals may be made only with prior approval of AFRPL (RPPR-STINFO) Edwards AFB Calif. 93523

Best Available Co[illegible]

(210 150)

Best
Available
Copy

FOREWORD

This Final Technical Report covers all work performed under Contract No. AF 04(611)-11615. The report was prepared by J. S. Coverdale, Program Engineering Manager, Norbert Wells, Metallurgist, Gilbert Skopp, Stress Analyst, and George Broeker, Nondestructive Test Engineer, of Lockheed Propulsion Company (LPC).

The program was monitored by Air Force Rocket Propulsion Laboratory (AFRPL), Edwards, California (W. F. Payne, Project Engineer).

This report contains information regarding a 156-inch diameter maraging steel case hydroburst and hydroburst analysis. The report is unclassified.

The report has been reviewed and is approved.

W. F. Payne
Project Engineer
Edwards Air Force Base
California

UNCLASSIFIED ABSTRACT

Activities in the hydroburst of a previously fired 156-inch diameter, maraging steel motor case are described. The program encompassed discontinuity stress analysis of the large, welded vessel, an evaluation of ultrasonic inspection methods by post-test sectioning, and a detailed failure analysis.

The water-filled motor case, consisting of forward and aft case segments joined by a tapered pin joint, was pressurized from a gaseous-nitrogen source through a water accumulator. At 800 psi, 85 percent of the planned cyclic pressure level, the nozzle adapter-to-case bolts failed; secondary origins were found in the pin joint and the nozzle adapter forging. Concurrent examinations of the previously used bolts by LPC, Mellon Institute, and SPS Laboratories, agreed in findings of evidence of stress corrosion in the 260,000-psi strength level H-11 bolts.

The discontinuity stress analysis showed a forty percent indicated stress riser around the longitudinal welds caused by "sea-gulling" contour deviations. These findings were based on the use of a finite element, nonlinear plane strain computer routine modified from a program written by Dr. L. R. Herrmann. This determination was verified by strain measurements taken during the pressure test.

Shear wave ultrasonic testing methods proved effective in detecting and defining parent metal and weld deposit flaws.

TABLE OF CONTENTS

Section		Page
I	INTRODUCTION AND SUMMARY	1
	1. INTRODUCTION	1
	2. SUMMARY	1
	a. Pretest Evaluation	2
	b. Test Operations	2
	c. Post-Burst Analysis	2
II	BACKGROUND DATA	5
	1. DETAILS OF MOTOR CASE HISTORY	5
	2. NOZZLE ADAPTER BOLT HISTORY	9
III	TEST OPERATIONS	11
IV	ANALYSIS OF STRAIN GAGE DATA	15
V	FAILURE ANALYSIS	23
	1. INTRODUCTION	23
	2. POST-TEST CONDITION AND FAILURE SEQUENCE	23
	3. FAILURE DISCUSSION	27
	4. MICROSTRUCTURE	27
	5. TENSILE TEST	35
	6. MELLON INSTITUTE ANALYSIS	41
	7. BOLT MATERIAL CONSIDERATIONS	41
	8. MELLON INSTITUTE REPORT	43
	9. APPENDIXES TO MELLON INSTITUTE REPORT	47
VI	DISCONTINUITY STRESS ANALYSIS	79
	1. INTRODUCTION	79
	2. STRUCTURAL DESCRIPTION	81

TABLE OF CONTENTS (Continued)

Section		Page
	3. HYDROSTATIC TEST METHODS	82
	4. METHOD OF DISCONTINUITY STRESS ANALYSIS	85
	a. Large Deformation Analysis	85
	b. Material Properties	89
	c. Iterative Solution Procedure	91
	d. Conclusion	96
	5. DISCUSSION OF ANALYSES	97
	a. Discontinuity Stress Analysis	97
	b. Bolt Adapter-Aft Closure	97
	c. Pin Joint Analysis	99
	6. EMPIRICAL DATA VERSUS ANALYTICAL RESULTS OF DISCONTINUITY STRESS ANALYSIS	99
	7. CONCLUSIONS	100
	8. STRUCTURAL ANALYSIS OF DISCONTINUITY STRESSES	101
VII	NONDESTRUCTIVE TESTING EVALUATION	103
	1. INTRODUCTION AND SUMMARY	103
	2. NONDESTRUCTIVE TESTING	103
	a. Pre-Hydroburst Inspection	103
	b. Post-Hydroburst Inspection	110
	c. Metallurgical Investigation	112
	d. Mellon Institute Report	117
VIII	CASE CUTTING BY LINEAR-SHAPED CHARGE	141
Appendix		
	BOLT STRESS ANALYSIS	143

ILLUSTRATIONS

Figure		Page
1	Pre-Test (a) and Post-Test (b) Hardware Arrangement	3
2	Schematic Diagram of Hydroburst Pressurization System	12
3	Strain Gage Locations, 156-Inch Case Hydroburst	13
4	First Hydrotest Cycle, 156-Inch Motor Chamber	13
5	Microstrain versus Pressure, Gages 1H, 1L, 101H and 101L. Thickness = 0.424 Inch	16
6	Microstrain versus Pressure, Gages 2H, 2L, 102H and 102L. Thickness = 0.422 Inch	17
7	Microstrain versus Pressure, Gages 3H, 3L, 103H and 103L. Thickness = 0.420 Inch	17
8	Microstrain versus Pressure, Gages 4H, 4L, 104H and 104L. Thickness = 0.417 Inch	18
9	Microstrain versus Pressure, Gages 5H, 5L, 105H and 105L. Thickness = 0.407 Inch	18
10	Microstrain versus Pressure, Gages 6H, 6L, 106H and 106L. Thickness = 0.376 Inch	19
11	Microstrain versus Pressure, Gages 7H, 7L, 107H and 107L. Thickness = 0.384 Inch	19
12	Microstrain versus Pressure, Gages 8H, 8L, 108H and 108L. Thickness = 0.375 Inch	20
13	Microstrain versus Pressure, Gages 9H, 9L, 109H and 109L. Thickness = 0.388 Inch	20
14	Type and Location of Bolt Failures, Depicting a Typical Shear to Tensile Mode Transition	24
15	Aft Section of 156-Inch Diameter Chamber Showing Oval Condition after Hydroburst and Cracked Clevis Joint Forging on Left-hand Side	24
16	Close-up of Clevis Joint Fracture	25
17	Primary Origin of Failure of Adapter Forging	25
18	One View of Adapter Forging Remnant on Aft Segment. Closure Lying on Ground	26

ILLUSTRATIONS (Continued)

Figure		Page
19	Close-up View of Adapter Forging Remnant on Chamber and Attached to Closure	26
20	Assembled Fragments of Adapter Forging	28
21	Thread Damage Found on Many of the Bolts	28
22	Pitting Experienced by Many of the Bolts	29
23	Tensile Type Failure which Nucleated at a Point and Propagated Through the Bolt	29
24	Shear Type Fracture Exhibited by Many of the Bolts	30
25	Typical Photograph of Cupped Tensile Failure Mode, 20 Bolts, Batch 5	30
26	Typical Photograph of Shear Failure Mode, 16 Bolts, Batch 5	31
27	Photomicrographs of the Normal Hardened and Tempered Martensite Exhibited by the Bolts	32
28	Thread Rolling Defect in the Crest of a Thread (Note plating on thread surface)	33
29	Another Thread Rolling Defect in Crest of Thread	33
30	Transverse Microstructure Crack Propagating from a Check in the Crest of a Thread	33
31	Transverse Microstructure -- Crack Propagating from Crest of a Thread	34
32	Secondary Cracking Noted at the Origin of the Fracture	34
33	Secondary Crack in the Root of the First Thread under the Fracture	34
34	Example of Severe Thread Damage of Unfailed Bent Part	36
35	Thread Damage at Original Point of Cracking (Failure) Indicated by Arrow	36
36	Thread Failure As-Received. Note Pitted Shank and Damaged Thread Area	37
37	After Strip of Plating - Note Pitted Shank and Thread Area	37

ILLUSTRATIONS (Continued)

Figure		Page
38	Fracture Face of Failed EWB 26-12 As-Received	38
39	Fracture Face of Unused EWB 26-12 Following a Tensile Test with a 3^0 Angle Under the Nut	38
40	Secondary Cracking from Fracture Surface	39
41	Final Section (Opposite Origin) of Fracture - Secondary Cracking. Note Shear Lip at End of Fracture	39
42	Origin of Failure Area (As-Received). Note Pitting of Thread Area	40
43	Tensile Test Specimen - Unused EWB 26 Bolt	42
44	Tensile Test Specimen After 24-Hour Exposure to H_2O (Unused EWB 26)	42
45	Photograph of the Fractured Surface of H-11 Steel Bolt Sample, Mellon Code A, and Pertinent Information	49
46	Fractograph Showing an Intergranular Mechanism of Fracture Propagation. Arrows Point Out Corrosion Products	50
47	Fractograph Showing an Intergranular Mechanism of Fracture Propagation. Arrows Point Out Corrosion Products	50
48	Fractograph Showing a Mixed Intergranular and Quasi-Cleavage Fracture Mechanism. The Dark Material on the Fractograph is a Remnant of Surface Oxide Initially Contaminating the Surface	50
49	Fractograph Showing a Mixed Intergranular and Quasi-Cleavage Fracture Mechanism	50
50	Photograph of the Fractured Surface of H-11 Steel Bolt Sample, Mellon Code B, and Pertinent Information	51
51	Fractograph Showing a Mixed Intergranular and Quasi-Cleavage Fracture Mechanism	52
52	Fractograph Showing a Mixed Quasi-Cleavage and Dimpled Rupture Fracture Mechanism	52
53	Fractograph Showing Quasi-Cleavage Fracture Mechanism	52

ILLUSTRATIONS (Continued)

Figure		Page
54	Fractograph Showing a Mixed Quasi-Cleavage and Dimpled Rupture Fracture Mechanism	52
55	Photograph of the Fractured Surface of H-11 Steel Bolt Sample, Mellon Code C, and Pertinent Information	53
56	Fractograph Showing a "Mud-Crack" Pattern, a Phenomenon of Corrosive Attack, Commonly Found Accompanying Stress Corrosion Failures	54
57	Fractograph Showing Large Amounts of Corrosion Products (see arrows) on What Appeared to be Intergranular Fracture Facets	54
58	Fractograph Showing a Mixed Intergranular and Quasi-Cleavage Fracture Mechanism. Arrows Point Out Corrosion Products on the Fracture Facets	54
59	Fractograph Showing a Quasi-Cleavage Fracture Mechanism in the Presence of a Smooth Corrosion Product (see arrows)	54
60	Fractograph Showing a Material Defect Type of Fracture Mechanism. In This Case, the Material Defect is Large Amounts of Banded and Clustered Secondary Phase Particles	55
61	Fractograph Showing a Material Defect Type of Fracture Mechanism. In This Case, the Material Defect is Large Amounts of Banded and Clustered Secondary Phase Particles	55
62	Photograph of the Fractured Surface of H-11 Steel Bolt Sample, Mellon Code D, and Pertinent Information	55
63	Fractograph Showing a Quasi-Cleavage Fracture Mechanism with Numerous Fine-Line Markings on the Fracture Facets	56
64	Fractograph Showing a Quasi-Cleavage Fracture Mechanism with Numerous Fine-Line Markings on the Fracture Facets	56
65	Fractograph Showing a Mixed Quasi-Cleavage and Intergranular Fracture Mechanism with Numerous Fine-Line Markings on the Fracture Facets	56

ILLUSTRATIONS (Continued)

Figure		Page
66	Fractograph Showing a Quasi-Cleavage Fracture Mechanism with Numerous Fine-Line Markings on the Fracture Facets	56
67	Fractograph Showing a Mixed Quasi-Cleavage and Intergranular Fracture Mechanism	57
68	Fractograph Showing a Mixed Quasi-Cleavage and Dimpled Rupture Fracture Mechanism	57
69	Fractograph Showing a Mixed Quasi-Cleavage and Dimpled Rupture Fracture Mechanism	57
70	Photograph of the Fractured Surface of H-11 Steel Bolt Sample, LPC Code 2, and Pertinent Information	58
71	Fractograph Showing Complete Lack of Ductile Fracture Features	59
72	Fractograph Showing Complete Lack of Ductile Fracture Features	59
73	Fractograph Showing Signs of an Intergranular Fracture Mechanism	59
74	Fractograph Showing Mixed Quasi-Cleavage and Dimpled Rupture Fracture Mechanism	59
75	Photograph of the Fractured Surface of H-11 Steel Bolt Sample, LPC Code [illegible], and Pertinent Information	60
76	Fractograph Showing a Mixed Quasi-Cleavage and Intergranular Fracture Mechanism with Fine-Line Markings on the Fracture Facets	61
77	Fractograph Showing Quasi-Cleavage Fracture Mechanism with Fine-Line Markings on the Fracture Facets	61
78	Fractograph Showing a Quasi-Cleavage and Intergranular Fracture Mechanism	61
79	Fractograph Showing Quasi-Cleavage Fracture Mechanism	61
80	Photograph of the Fractured Surface of H-11 Steel Bolt Sample, LPC Code 86, and Pertinent Information	62

ILLUSTRATIONS (Continued)

Figure		Page
81	Fractograph Showing Complete Lack of Ductile Fracture Features	63
82	Fractograph Showing a Mixed Quasi-Cleavage and Dimpled Rupture Fracture Mechanism	63
83	Fractograph Showing a Directional Dimpled Rupture Mechanism of Fracture Propagation with an Etching Effect on the Fracture Facets	63
84	Fractograph Showing a Directional Dimpled Rupture Mechanism of Fracture Propagation with an Etching Effect on the Fracture Facets	63
85	Photograph of the Fractured Surface of H-11 Steel Bolt Sample, LPC Code 95, and Pertinent Information	64
86	Fractograph Showing an Intergranular Fracture Mechanism with Corrosion Products (see arrows) Present in Fracture Facets	65
87	Fractograph Showing An Intergranular Fracture Mechanism with Corrosion Products (see arrows) Present in Fracture Facets	65
88	Fractograph Showing Quasi-Cleavage Fracture Mechanism with Corrosion Products Present on all Fracture Facets	65
89	Fractograph Showing "Mud-Crack" Patterns and Corrosion Products Obscuring the Fracture Pattern	65
90	Fractograph Showing a "Mud-Crack" Corrosion Pattern Completely Obscuring the Fracture Pattern	66
91	Fractograph Showing a Needle-Like Corrosion Product Completely Obscuring the Fracture Pattern	66
92	Photograph of the Fractured Surface of H-11 Steel Bolt Sample, LPC Code 99, and Pertinent Information	66
93	Fractograph Showing a Quasi-Cleavage Fracture Mechanism with Many Fine-Line Markings on the Fracture Facets	67
94	Photograph of the Fractured Surface of H-11 Steel Bolt Sample, LPC Code 106, and Pertinent Information	67

ILLUSTRATIONS (Continued)

Figure		Page
95	Fractograph Showing Quasi-Cleavage Fracture Mechanism with the Presence of a Smooth Corrosion Product (see arrows)	68
96	Fractograph Showing Quasi-Cleavage Fracture Mechanism with the Presence of a Smooth Corrosion Product (see arrows)	68
97	Fractograph Showing a Mixed Quasi-Cleavage and Dimpled Rupture Fracture Mechanism with the Presence of a Smooth Corrosion Product (see arrows)	68
98	Photograph of the Fractured Surface of H-11 Steel Bolt Sample, LPC Code 146, and Pertinent Information	69
99	Fractograph Showing Quasi-Cleavage Fracture Mechanism.	70
100	Fractograph Showing Quasi-Cleavage Fracture Mechanism	70
101	Fractograph Showing Quasi-Cleavage Fracture Mechanism	70
102	Photograph of the Fracture Surface of the Section From the Adapter Forging and Pertinent Information	71
103	Fractograph Showing a Micro-Void Coalescense Mechanism of Fracture Propagation Characterized by Directional Dimples	71
104	Fractograph Showing a Micro-Void Coalescense Mechanism of Fracture Propagation Characterized by Directional Dimples	72
105	Figure 105 Fractograph Showing a Micro-Void Coalescense Mechanism of Fracture Propagation Characterized by Directional Dimples	72
106	Fractograph Showing a Brittle Fracture Mechanism in an Area where Secondary Phase Material is Present (see arrows). A Needle-Like Corrosion Product is Shown by the Open Arrows	72
107	Fractograph Showing a Brittle Fracture Mechanism in an Area where Secondary Phase Material is Present (see arrows)	72

ILLUSTRATIONS (Continued)

Figure		Page
108	Photomicrographs Showing the Profile of the Fracture Origin, (a) and (b), of Bolt Sample 86. A Deformation Band Present at the Root of a Thread and the Occasional Cracking Found in the Bands are Shown in (c) and (d), Respectively	73
109	Photomicrographs Showing the Location, (a) and (b), and the Profile, (c) and (d), of the Fracture Origin in Bolt Sample 2	74
110	Photomicrographs, (a), Showing the Location of the Fracture Origin with Respect to the Thread Deformation Band in Bolt Sample 2, and (b) Cracking in the Deformation Band Associated with the First Thread Below the Fracture	75
111	Fractograph Showing a Fine Network of Cracks Penetrating into the Cadmium Plate at the Root of the Thread Immediately Below the Fracture in Bolt Sample 95	76
112	Photograph of the Fractured Surface of the Bolt Sample Sent from Rocket Propulsion Laboratory. The Arrow Shows the Area of Initial Fracture where Replication was Conducted	77
113	Fractograph Showing a Transgranular Fracture Mechanism with Many Fine-Line Marking on the Fracture Facets	77
114	Fractograph Showing a Transgranular Fracture Mechanism with Many Fine-Line Markings on the Fracture Facets	77
115	Fractograph Showing a Transgranular Fracture Mechanism with Many Fine-Line Markings on the Fracture Facets	78
116	Fractograph Showing a Transgranular Fracture Mechanism with Many Fine-Line Markings on the Fracture Facets	78
117	Fractograph Showing a Transgranular Fracture Mechanism with Many Fine-Line Markings on the Fracture Facets	78
118	Fractograph Showing a Transgranular Fracture Mechanism with Many Fine-Line Markings on the Fracture Facets	78

ILLUSTRATIONS (Continued)

Figure		Page
119	Typical Contour Measurement Depicting Peaking	83
120	Coordinate Systems	87
121	Location of Two Points in the Deformed and Undeformed Body	87
122	Anticipated Stress State Occurring in the Pressurized Case	90
123	Finite Element Representation of Chamber	94
124	Detailed View of the Elements Surrounding Node Point n	94
125	Division of Quadrilateral into Four Triangles	97
126	Hoop Stress versus Circumferential Position at Point of Greatest Discontinuity	98
127	Ejection Force versus Coefficient of Friction	100
128	156-Inch Diameter Hydroburst Weld Identification	104
129	Forward Head Section, Weld C-5, Igniter Boss Weld, View AA	105
130	Forward Head Section, Weld C-3, Forward Girth Weld, View CC	105
131	Aft Head Section, Weld C-1, Joint to Cylinder Section Weld, View DD	106
132	Aft Head Section, Weld C-3, Cylinder to Dome Weld, View EE	106
133	Aft Head Section, Weld C-4, Nozzle Adapter to Dome Weld, View BB	107
134	Ultrasonic Calibration, LPC Shear Wave Test Plate, 250 Grade Marage, 0.375 to 0.400-Inch Thickness	108
135	Ultrasonic Signal Indication from Shear Wave Calibration	109
136	156-Inch Diameter Hydroburst Weld Identification and Test Plate Location (Post-Hydroburst)	111
137	Shear Wave Indication From 32-3	113

ILLUSTRATIONS (Continued)

Figure		Page
138	Aft Section Plate 18A, Weld C-4	115
139	Aft Segment Plate 28A Containing Girth Weld C-3	116
140	Photograph of Defect No. 13, Illustrating the Delaminations Found in Plate 28A. The Thick White Line is the Delamination and the Thin White Lines are Segregated Stringers of Titanium Carbonitrides	118
141	Photograph of Defect No. 2, Illustrating the Delaminations Found in Plate 18A. The Thick White Line is the Delamination and the Thin White Lines are Segregated Stringers of Titanium Carbonitride	118
142	Photomicrograph of Delamination Exhibited by Defect No. 2, Located in Plate 28A	119
143	Photomicrograph of Delamination Exhibited by Defect No. 3, Located in Plate 28A	119
144	Photomicrograph of Delamination Exhibited by Defect No. 4, Located in Plate 28A	119
145	Photomicrograph of Delamination Exhibited by Defect No. 5, Located in Plate 28A	119
146	Photomicrograph of a Small Delamination Exhibited by Defect No. 10, Located in Plate 18A	120
147	Photomicrograph of Delamination Exhibited by Defect No. 11, Located in Plate 18A	120
148	Photomicrograph of Delamination Exhibited by Defect No. 12, Located in Plate 18A	120
149	Photomicrograph of Delamination Exhibited by Defect No. 13, Located in Plate 18A	120
150	Photomicrograph of Defect No. 12, Located in Plate 18A	121
151	"Lead-Off" Page for Sample 1 Showing (a) a Sketch of the Sample, (b) a Sketch of the Sectioned Metallographic Specimen, (c) an Oscillograph Display of the Defect, and (d) a Photomicrograph of the "Most Open" Portion of the Crack	125

ILLUSTRATIONS (Continued)

Figure		Page
152	Photomicrographs Showing the Association of the Cracks with the Banding (a) and the Stringers of Secondary Phase Particles, (b) and (c) in Sample 1	126
153	"Lead-Off" Page for Sample 3 Showing (a) a Sketch of the Sample, (b) Sketches of the Section Metallographic Specimens, (c) an Oscillograph Display of the Defect, and (d) Photomicrographs of the "Most Open" Portion of the Cracks in Specimens 3A and 3B, Respectively	127
154	Photomicrographs Showing the Association of the Cracks with Stringers of Secondary Phase Particles in (a) Sample 3A and (b) Sample 3B	128
155	Photomicrographs Showing the Association of the Cracks with (a) and (b) Banding and (c) and (d) Stringers of Secondary Phase Particles in Sample 3A	129
156	Photomicrographs Showing the Association of the Cracks with Banding in Sample 3B	130
157	Photomicrographs Showing the Association of the Cracks with Stringers of Secondary Phase Particles in Sample 3B	131
158	"Lead-Off" Page for Sample 4 Showing (a) a Sketch of the Sample, (b) a Sketch of the Sectioned Metallographic Specimen, (c) an Oscillograph Display of the Defect, and (d) a Photomicrograph of the "Most Open" Portion of the Crack	132
159	Photomicrograph Showing the Association of the Cracks with Banding (a) and Stringers of Secondary Phase Particles (b), (c) and (d) in Sample 4	133
160	"Lead-Off" Page for Combination Samples 5, 6, and 7 Showing (a) a Sketch of the Sample, (b) Sketches of the Corresponding Metallographic Specimens, (c) an Oscillograph Display of the Defects, and (d) Photomicrographs of the "Most Open" Portion of the Cracks in Specimens 5 and 7, Respectively	134
161	Photomicrographs Showing the Association of the Cracks with (a) Banding and (b), (c) and (d) Stringers of Secondary Phase Particles in Sample 5	135

ILLUSTRATIONS (Continued)

Figure		Page
162	Photomicrographs Showing the Association of the Cracks with (a) Banding and (b) Stringers of Secondary Phase Particles in Sample 7	136
163	"Lead-Off" Page for Combination Samples 8 and 9 Showing (a) a Sketch of the Sample, (b) Sketches of the Sectioned Metallographic Samples, (c) an Oscillograph Display of the Defects, and (d) Photomicrographs of the "Most Open" Portion of the Crack in Samples 9 and 8, Respectively	137
164	Photomicrographs Showing the Association of the Cracks with (a) Banding and (b), (c) and (d) Stringers of Secondary Phase Particles in Sample 9	138
165	Photomicrographs Showing the Association of the Cracks with (a) Banding and (b), (c), and (d) Stringers of Secondary Phase Particles in Sample 8	139
166	Sketch Showing Mounting of Linear Shaped Charge	141
167	Motor Case Forward Section Cutting Operation	142

LIST OF TABLES

Table		Page
I	156-INCH DIAMETER MOTOR CASE FABRICATION RECORDS	6
II	TYPICAL MATERIAL CERTIFICATION SHEET	6
III	ULTRASONIC THICKNESS MEASUREMENTS	7
IV	ULTRASONIC THICKNESS MEASUREMENTS: FORWARD SEGMENT, P/N 200001	7
V	AFT SEGMENT PLATE THICKNESS MEASUREMENTS	8
VI	156-INCH DIAMETER CHAMBER; CALCULATED ACTUAL STRESS AT 300 psi	16
VII	COMPARISON OF HERRMANN AND SWEDLOW PROGRAMS	80
VIII	TENSILE STRENGTHS AND CALCULATED PRESSURES FOR 156-INCH DIAMETER MOTOR CASE	84
IX	CALCULATED PRESSURES TO ACHIEVE MEMBRANE HOOP STRESSES, ASSUMING NOMINAL RADIUS CYLINDER WITH MINIMUM MEASURED THICKNESS	84
X	156-INCH DIAMETER HYDROBURST WELD IDENTIFICATION AND DEFECT LOCATION	104
XI	ULTRASONIC TEST INDICATION FROM PLATE 18A	114
XII	ULTRASONIC TEST INDICATIONS FROM PLATE 28A, AFT HEAD SECTION WELD C-3	114
XIII	SIZE OF DELAMINATIONS	122
XIV	DESCRIPTION OF THE RESULTS OF THE DEFECT SEARCH	123

LIST OF SYMBOLS

A	Area of cross-section (in.^{2})
b	Subscript (bending)
C	Coefficient
c	Distance from neutral axis to extreme fiber (in.)
c	Subscript (compression, chamber)
D	Diameter (in.)
D	Flexural rigidity = $\frac{Et^3}{12(1-\nu^2)}$ (lb-in.^{2})
E	Modulus of elasticity (psi)
e	Elongation or displacement (in.)
F	Allowable stress (psi)
f	Calculated stress (psi)
h	Height or depth (in.)
h	Subscript (hoop)
i	Subscript (inside)
I	Moment of inertia (in.^{4})
L	Length (in.)
M	Bending moment (in.-lb or in.-lb/in.)
m	Subscript (meridional)
N	Normal force (lb/in.)
o	Subscript (outside)
P	Applied load (lb or lb/in.)
P_b	Allowable bolt load (lb/bolt)
p	Pressure (psi)
Q	Radial shear (lb/in.)
Q	Moment of the area of the section above or below the plane containing the points where the transverse shear is to be determined (in.^{3}).

R	Radius (in.)
R_2	Circumferential radius of curvature (in.)
r	Subscript (reference)
s	Subscript (shear)
t	Thickness (in.)
t	Subscript (tension)
T	Applied load (lb/in.)
u	Subscript (ultimate)
V	Shear force (lb/in.)
W	Weight (lb)
w	Uniform weight distribution (lb/in.)
x	Distance along x-axis
y	Distance along y-axis
y	Subscript (yield)
β	Damping function $= \left[\frac{3\,(1-\nu^2)}{R_2^2\ t^2}\right]^{1/4}$ (in.$^{-1}$)
ω	Deflection (in.)
ν	Poisson's ratio
ϵ	Expansion ratio
ϵ	Strain (in./in.)
θ	Change in slope (radians or degrees)
θ	Subscript (hoop direction)
ϕ	Angle of rotation
μ	Coefficient of friction
ϕ	Subscript (meridional direction)
τ	Shear stress
avg.	Average

c.g.	Center of gravity
eq.	Equivalent
in.	Inch
int.	Interlaminar
Ksi	Kilo pounds per square inch
lb	Pounds
max	Maximum
MEOP	Maximum expected operating pressure
min	Minimum
M.S.	Margin of safety
psia	Pounds per square inch, absolute
psig	Pounds per square inch, gage

SECTION I

INTRODUCTION AND SUMMARY

1. INTRODUCTION

This report is issued by Lockheed Propulsion Company (LPC) pursuant to the requirements of Contract No. AF 04(611)-11615 "156-Inch Diameter Maraging Steel Case Hydroburst and Materials Evaluation" dated 11 April 1966. The objectives of the program were to develop improved methods of case performance predictions by the hydroburst, failure analysis, and material mechanical testing of an available 156-inch diameter, 18% nickel maraging steel case.

Significant work was accomplished in contour discontinuity elastic stress analysis in the longitudinal weld region and ultrasonic inspection correlation, and the failure analysis provided additional data on the stress corrosion cracking of high-strength steel bolts.

The motor case was fabricated between May 1963 to March 1964 by Excelco Developments, Inc. It was the first 156-inch diameter motor case ever built, and also the first large motor to utilize 18 % nickel maraging steel. The case was made from 0.390-inch thick, 250 grade air-melted plate from U.S. Steel Corporation; all forgings were 250 grade VAR maraging steel from Standard Steel Works Division of Baldwin-Lima-Hamilton Corporation. Manufactured under Contract No. AF04(695)-364, "156-Inch Diameter Motor Jet Tab TVC Program," the motor case was fired twice, in May and September, 1964. The final report of that contract, Technical Report No. AFRPL-TR-64-167 contains detailed material, fabrication, inspection, and testing data. Section II of this report summarizes only data pertinent to the program analysis and testing efforts. The case was subsequently fired as a gas generator for the hot gas valve development program under Contract No. AF 04(611)-9960.

Early in the fabrication process, material deficiency of chemical segregation associatiated with heavy banding was noted. These strata of inclusions, containing heavy austenite concentration, became visible delaminations under conditions of shear or transverse stress imposed by bending or welding heat. During case pressurizations, however, no evidence of flaw extension had been noted in any of the motor hardware based on ultrasonic definition of the defect limits. Welding defects such as light porosity, inclusions, lack of penetration (fusion) and interface cracks are often detectable by ultrasonic means. To define the limits of detectability and the conditions under which extension may occur, constituted program goals.

2. SUMMARY

On 17 May 1966, the motor case was pressurized in 100-psi increments to the planned cyclic maximum pressure of 935 psi. Following a 10-minute data-reading hold at 800 psi, burst occurred by failure of the nozzle adapter-to-case bolts. Subsequent movement of the parts caused secondary failure

origin in the large adapter forging and in the pin joint, rupturing the female tangs of the joint and ejecting the tapered pins. Program activity, including the results of post-test analysis and conclusions as to the failure mechanism are summarized below.

a. Pretest Evaluation

Review of the case fabrication inspection records and prior membrane contour measurements in the vicinity of the longitudinal welds indicated that these welds were the only structurally critical regions of the case. This was corroborated by the visual examination (see Section VI). Additional longitudinal weld contour measurements were taken, and formed the basis for selecting strain gage locations. Comparison of these readings with the previous records showed that permanent set around these welds had occurred during prior motor pressurizations (see Section II for pressurization history of case hardware).

Review of the ultrasonic inspection records was conducted, and indicated defects were marked out on the case for ultrasonic verification. Paint was removed from the longitudinal weld regions. The Excelco records showed no indications in the longitudinal welds, and mixed light and heavy delaminations in the less critical girth welds. The LPC inspection generally substantiated the Excelco results, although six previously unreported longitudinal weld region delamination indications, a single within-specification porosity, and one 0.30-inch lack of weld fusion were detected and verified by X ray. Exceptional weld quality and cleanliness was obvious, considering the defective material. The indications were marked for monitoring during hydrotest cycling.

b. Test Operations

The motor case was stored in position in the large motor bay. Following removal of loose insulation char, the motor case was positioned horizontally in pillow blocks, supported by the forward and aft skirts, and prepared for inspection and instrumentation. Instrumentation and test procedures are summarized in Section III. Figure 1 pictures pre-and post-test hardware arrangement.

c. Post-Burst Analysis

Following hydroburst, the failed hardware was recovered and fracture surfaces preserved; the nozzle adapter was assembled for tracing of the fracture path.

The adapter joint bolt circle was partially intact (see Figure 1); the adapter and bolts indicated a mixed tensile and tearing failure, with probable primary fracture damage to the adapter on impact with a proximate restraing cable. Of the 256 EWB 926-12-20 bolts, 133 showed tensile failure, 50 showed shear failure, and 73 remained in place. Concurrent evaluation by LPC, Mellon Institute, and SPS Laboratories was conducted. The three agencies concur in their findings of stress corrosion/hydrogen embrittlement damage to the bolts. The reports are included in Section V.

(a)

(b)

Figure 1 Pre-Test (a) and Post-Test (b) Hardware Arrangement

A reasonably specific sequence of events can be determined from the post-test hardware condition: (1) adapter failure, driving the motor forward skirt into the asphalt pavement, (2) movement of the motor upward into the restraining cables, creating severe ovality with cracking of the female joint at the lateral point of maximum curvature, and (3) sequential ejection of pins causing separation movement of the segments.

A discontinuity stress analysis of the longitudinal weld region was performed utilizing a finite element nonlinear plane strain computer program written by Dr. L. R. Herrmann. This program was selected principally because of its ability to analyze non-axisymmetric configurations and account for nonlinear material properties and large deformations by a successive iterative technique, in effect, performing an elastic-plastic solution. In the finite element approximation of solids, the continuous structure is replaced by a system of elements which are interconnected at joints or nodal points. Equilibrium equations, in terms of unknown nodal point displacements are developed at each nodal point, and the complete set of equations for all elements in the structure are solved by means of an elimination simultaneous equation procedure.

The most severe discontinuity was analyzed. Results show that the premature failure of the motor case at 800 psi could not be attributed to the contour deviations at the longitudinal weld. At the point of maximum stress, a magnitude of 226,000 psi was computed, resulting in a 40 % increase over the anticipated stress in a similar cylinder that is perfectly round, a margin of safety of 0.14 based on a minimum yield strength of 240,000 psi and bending modulus of 1.25 times the minimum yield strength.

A structural analysis of the adapter-aft closure bolts showed an anticipated margin of safety of 1.28 at 800 psi due to the basic tensile load and the additional load from reacting the interface bending.

This stress level is sufficiently high to sustain a stress corrosion reaction, when a corrosive media is present and the protective cadmium coating is damaged. The motor case had been exposed to inclement weather with the bolts in a pretorqued condition, and it is shown in Section V of this report that damage to the bolt coating had been incurred in reuse of the bolts.

SECTION II

BACKGROUND DATA

1. DETAILS OF MOTOR CASE HISTORY

Details of the motor case history are given in the final program report on Contract No. AF 04(695)-364 "156-Inch Diameter Motor Jet Tab TVC Program," Report No. AFRPL-TR-64-167, Volumes I and V, dated 29 January 1965. Table I indicates the data location. For reference purposes, a typical material certification sheet is given in Table II.

The pressurization history of the forward and aft segments is tabulated below:

Date	Operation	Pressure (psig)
Feb 1964	Hydrotest	685
29 May 1964	L-71 Firing	579
June 1964	Hydrotest	810
30 Sep 1964	L-72 Firing	651
25 Nov 1965	Hydrotest	750
7 Apr 1965	HGI TVC Firing	654
17 May 1965	Hydroburst	800

Vidigage readings of the case wall thickness were taken in the vicinity of the longitudinal welds. These readings, given in Tables III, IV, and V indicate a minimum value of 0.375 inches located in the aft course weld of the aft segment. The data obtained orginially by Pittsburgh-Des Moines Steel Company after surface grinding and the thickness measurements made by LPC prior to hydrotest are not directly correlative. The original thickness testing was conducted at the intersect points of a 12-inch drid pattern prior to net trimming of the plates. Thickness tests at LPC were made ajacent to the welds for purposes of strain gage location and stress analysis. The average thickness readings obtained at LPC are higher than those originally recorded for the plate; this is possibly due to weld metal filling adjacent to the joint. Data on two typical plates of material are compared below:

	Pittsburgh-Des Moines Ultrasonic Plate Thickness After Surface Grinding			LPC Ultrasonic Plate Thickness Adjacent to Weld		
	Min.	Max.	AVG			
Plate 47826 Ref C-1284	0.376	0.401	0.3915	0.402	0.424	0.4150
Plate 42294 Ref C-1285	0.384	0.408	0.3971	0.382	0.426	0.3950

TABLE I

156-INCH DIAMETER MOTOR CASE FABRICATION RECORDS

Subject	Volume	Pages
Development of Ultrasonic Methods	V	App. D
"Analysis of Fracture Aspects and Experimental Results - Maraging Steel Investigation," by J. L. Swedlow and R. A. Westmann	V	App. C
"Materials and Fabrication Evaluation and Related Metallurgical and Performance Reliability Studies Pertaining to the Lockheed 156-Inch Diameter Booster Case," by G. K. Bhat	V	App. B
"Stress Analysis of the 156-Inch Diameter Motor Case," by L. E. Colbert	V	App. A
Delamination Locations	V	App. D D-7 - D-12
Design Description	I	3-1 - 3-9
Materials Data		
Typical Furnace Record Heat and Slab Number Identification and Application Forging and Bar Stock Identification and Application Chemical Analyses Mechanical Properties Certifications Weld Wire Composition Physical Properties of Tensile Coupons Aged with the Case Sections	I	3-10 - 3-23
Case Fabrication Description	I	3-24 - 3-30
Hydrotesting Procedures, Instrumentation Locations, and Hydrotest Results	I	3-31 - 3-45
Material and Fabrication Evaluation Program Results	I	3-48 - 3-58

TABLE II

TYPICAL MATERIAL CERTIFICATION SHEET

UNITED STATES [illegible] CORPORATION

[illegible]

[illegible]

Best Available Copy

TABLE III

ULTRASONIC THICKNESS MEASUREMENTS

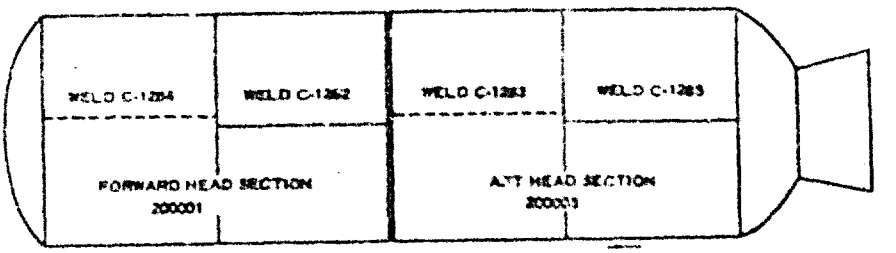

		6*	12	18	24	30	36	42	48	54	60	66	72	78	84	90
Weld C-1284	Above	416	414	420	420	420	420	420	420	418	416	416	410	412	410	
	Below	416	416	422	420	422	420	418	420	418	420	414	416	412	408	
Weld C-1282	Above	412	418	417	420	422	420	418	427	422	424	418	420	422	416	
	Below	412	416	412	417	418	420	416	416	420	420	419	418	424	419	
Weld C-1283	Above	388	380	382	383	382	381	382	382	384	385	388	304	420	420	390
	Below	382	390	390	392	392	392	392	392	392	390	382	392	390	392	415
Weld C-1285	Above	382	390	380	392	382	422	390	390	390	390	396	388			
	Below	386	380	393	382	394	396	400	400	386	400	388	394			

* Measurements taken with Branson Model 21 Vidigage 4/29/66 - Readings taken 1-inch above and 1-inch below center of long weld read at 6-inch intervals along the weld.

TABLE IV

ULTRASONIC THICKNESS MEASUREMENTS, FORWARD SEGMENT P/N 200001

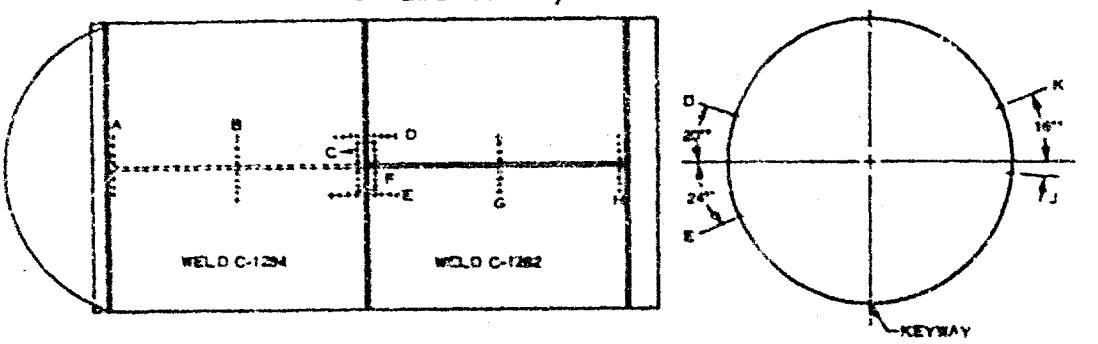

		-6 (in.)	-4 (in.)	-2 (in.)	-1 (in.)	0	+1 (in.)	+2 (in.)	+4 (in.)	+6 (in.)
A	1-in. aft of fwd. dome girth weld	408	410	410	408	Center of Long. Weld	406	405	410	404
B	Midway between fwd and center girth welds (43.5)	420	422	424	422		420	420	417	418
C	1-in. fwd of center girth weld	408	408	406	402		404	402	404	408
D	20-in. clockwise across center girth	438	440	438	437		420	424	422	424
E	24-in. counter-clockwise across center girth	390	400	400	390		424	424	420	422
F	1-in. aft of center girth weld	411	407	409	407		408	409	406	405
G	Midway between center and aft girth welds	416	415	421	416		417	417	414	422
H	1-in. fwd of aft girth weld	420	412	410	405		408	409	419	416
J	+1-in. clockwise across center girth	424	424	420	416		402	406	418	414
K	-16-in. counter-clockwise across center girth	426	422	420	420		412	416	416	414

Plus values above long. weld. Minus values below weld.
Plus values are forward of girth weld. Minus values aft.
Thickness taken with Branson Model 21 Vidigage.

TABLE V

AFT SEGMENT PLATE THICKNESS MEASUREMENTS

			(Distance in inches from center of weld bead)							
			-6	-4	-2	-1	+1	+2	+4	+6
Weld C-1283	1-in. Aft of fwd girth weld	A	420	412	418	420	406	428	412	414
	10-in. Aft of fwd girth weld	B	388	387	387	386	376	378	380	376
	22-in. Aft of fwd girth weld	C	390	390	390	392	384	384	380	380
	57-in. Aft of fwd girth weld	D	390	390	392	392	384	380	382	382
	22-in. Fwd of center girth weld	E	386	388	390	390	380	380	380	380
	10-in. Fwd of center girth weld	F	424	426	430	428	416	416	414	416
	1-in. Fwd of center girth weld	G	392	430	418	422	422	420	420	418
	18-in. Above long weld	H	422	420	420	420	414	416	413	412
	24-in. Below long weld	J	394	392	394	390	426	390	390	392
Weld C-1235	1-in. Aft of center girth weld	K	424	422	426	414	375	418	418	416
	10-in. Aft of center girth weld	L	386	388	386	388	382	382	384	380
	22-in. Aft of center girth weld	M	383	384	384	382	394	394	392	392
	57-in. Aft of center girth weld	N	396	396	398	398	388	389	390	386
	22-in. Fwd of aft girth weld	O	392	396	389	400	388	388	390	382
	10-in. Fwd of aft girth weld	P	394	394	396	396	390	390	392	389
	1-in. Fwd of aft girth weld	Q	388	394	392	392	386	383	390	390
	18-in. Above long weld	S	394	392	394	390	426	390	390	392
	24-in. Below long weld	T	398	396	396	394	398	-	396	396

Center of Weld

+ Plus values are above, minus values are below the long-weld bead.

+ Plus values are forward, minus values are aft of girth welds. Toward head end is plus, toward aft end of motor is minus.

LOCKHEED PROPULSION COMPANY

Results of ultrasonic inspection of the segments are given in Section VII.

2. NOZZLE ADAPTER BOLT HISTORY

Following is a summary of the pertinent information on the bolts used in attaching the nozzle adapter to the aft motor case segment.

There were 256 EWB 926-12-20 (3/4 - inch diameter by 2.56-inches long) bolts required for this use. These bolts were purchased by LPC under Air Force Contract No. 04(695)-364. Also used were WC 22-12 washers. A total of 800 bolts and 320 washers were purchased with 266 bolts and 256 washers shipped directly to Excelco for use in the hydrostatic test. The balance of the bolts and washers were shipped to LPC. Tests of the bolts showed them to meet all specification requirements.

During assembly of the motor case for hydrotest at Excelco, several of the bolts bottomed out during installation. These were removed, ground to shorten the length, and reinstalled. Following the hydrotest, the bolts were preserved and shipped with the case. At the insulation contractor, Rohr Corp., the nozzle adapter was installed with 64 bolts (every 4th bolt) to permit processing the silica-phenolic internal insulation. Hydrotest bolts and washers were used.

The aft motor segment was processed through insulation, lining and propellant casting with these 64 bolts. Prior to the L-71 firing, new bolts were installed throughout with two washers to prevent bottoming of the bolts. After the firing, the motor was hydrostatic tested to 810 psig without disassembly. Prior to the L-72 motor firing another new set of bolts was installed again with two washers under each bolt head.

The L-72 motor was disassembled and the forward and aft segments assembled for hydrostatic test. Prior to hydrotest, one bolt was found broken off in the adapter flange. All of the bolts were removed with 22 new bolts installed. The bolts removed were magnetic particle and visually inspected and then baked at 380° F for 12 hours. The bolts were replaced for the hydrostatic test which was completed on 25 November to a pressure of 750 psig.

Prior to the hot gas valve firing, 128 of the EWB bolts were removed and returned to Redlands for inspection and baking. At the time, an additional 188 used bolts from inventory were also magnetic particle inspected. The combined 316 bolts were baked at 375 ± 10°F for 12 hours. The bolts were visually inspected and re-installed with two washers. The bolts were lubricated with Moly Spray Koat and in-sequence torqued to 100 ft-lb to 250 ft-lb and finally to 375 ft-lb. The motor was fired on 7 April 1966.

The motor was then turned horizontally in the test bay and prepared for the hydrostatic burst. No additional torque of the bolts was made.

SECTION III

TEST OPERATIONS

The test program was conducted at LPC's Potrero Production and Test Facility, utilizing available analog and Beckman 210 digital data acquisition systems. Test Work Order and Test Procedure, Publication 751-TP-1, defines the detailed procedures for conducting the test program.

Following successful completion of the hot gas secondary injection TVC static test-firing, preparations commenced for the hydrocycling and the hydroburst of the 156-inch diameter chamber. The nozzle assembly was removed, the igniter was removed from the motor, and the chamber was cleaned of all loose insulation. The assembled motor case was removed from the thrust stand and placed in the LSM test bay in a horizontal position supported at each end skirt by 156-inch diameter pillow blocks. After paint was removed from the longitudinal weld exterior surfaces, visual and ultrasonic inspections were conducted to support stress analyses and verify existing data records defining known defects and suspected areas of potential failure. No inspection or replacement of the nozzle adapter bolts was conducted.

Fabrication and installation of the hydrostatic pressurization system was completed and hydrostatically tested with satisfactory results (Figure 2). Preparation of the internal chamber cabling system was completed under laboratory conditions to ensure the integrity of the cabling and pressure connectors.

The strain gages were installed and waterproofed in accordance with standard LPC procedure (see Figure 3). Only one gage was lost during the hydrotest operations and was due to a breakdown in the external resistive network, not the strain gage. Dentronics, Inc., Type 204C biaxial strain gages were installed at each of the nine locations on the motor chamber inside and out. A special high elongation strain gage, Dentronics Type 204Y, was installed parallel to and in line with the hoop gage portion of the internally mounted biaxial gages. This gage is capable of measuring an elongation of up to 12 percent (versus three percent limitation of the biaxial gage). The primary strain gage instrumentation system then consisted of 18 biaxial gages located on the outside of the chamber, 9 longitudinal portions of the biaxial gages mounted on the inside of the chamber, and 9 high elongation hoop gages mounted on the inside chamber wall.

The measurements were recorded on both digital and oscillographic acquisition systems.

On 17 May 1966, final instrumentation calibrations were conducted and the first hydrotest cycle initiated. The pressurization rate and the hold time increments are shown in Figure 4. During the hold time at 200 psi, a visual inspection of the assembled chamber and the pressurization system was conducted. All systems functioned normally and in accordance with the test plan.

After a constant pressure hold of 11 minutes at 800 psi for data checking, the chamber failed. Post-test inspection of the ruptured chamber revealed the damage and case displacement.

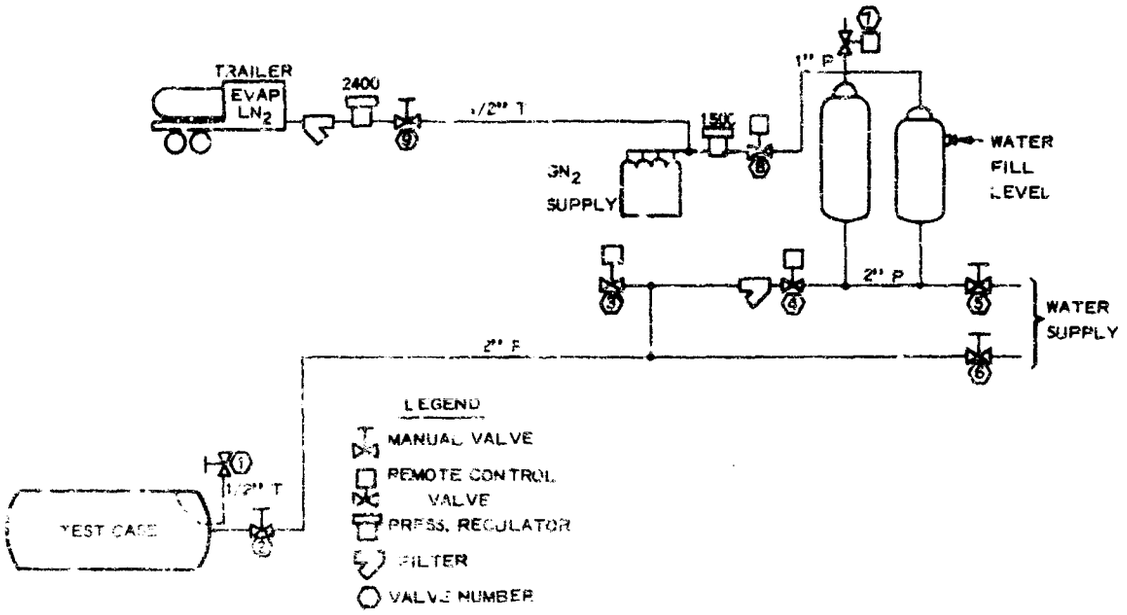

Figure 2 Schematic Diagram of Hydroburst Pressurization System

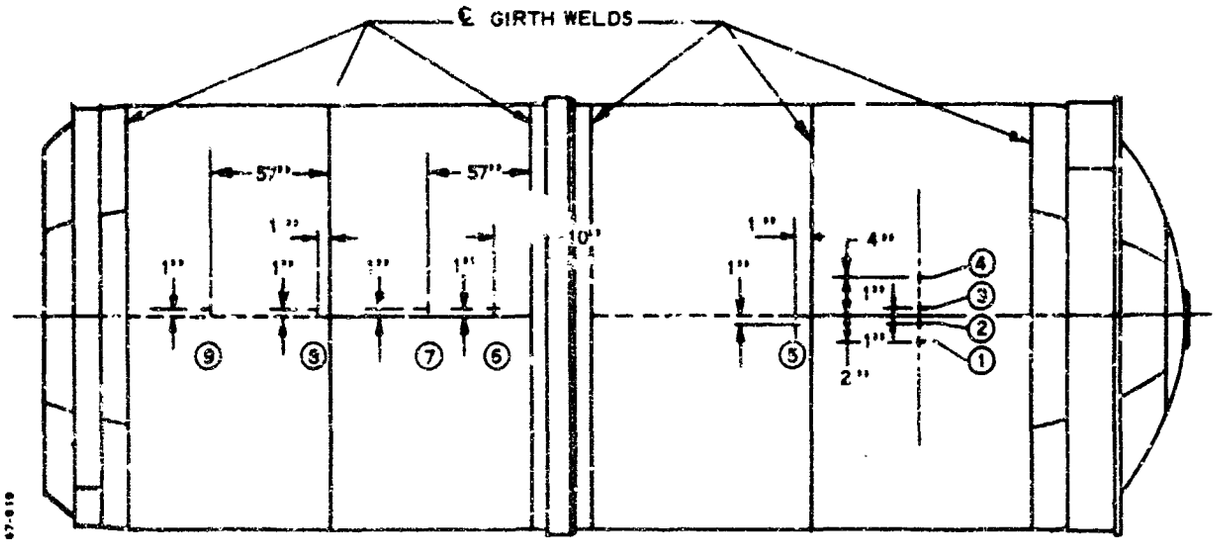

Figure 3 Strain Gage Locations, 156-Inch Case Hydroburst

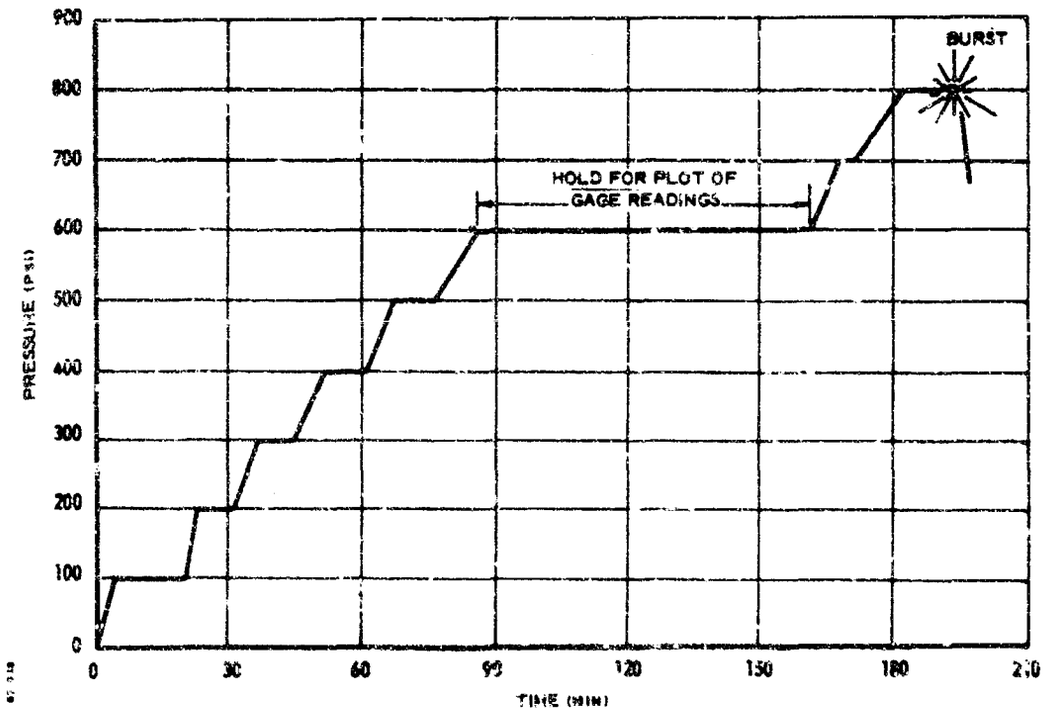

Figure 4 First Hydrotest Cycle, 156-Inch Motor Chamber

SECTION IV

ANALYSIS OF STRAIN GAGE DATA

Thirty-six strain gages were mounted at nine locations near the longitudinal welds, as shown in Figure 3. Gages on the inside were numbered 101 to 109 and gages on the outside 1 to 9 with the suffix L for longitudinal gages and H for hoop gages.

The data were recorded at 100-psi increments. Results are listed in Table 6 and plotted versus pressure in Figures 5 through 13. For reference purposes the theoretical strain versus pressure curves for a perfectly round cylinder with the nominal radius and local thickness is shown. In the elastic range below the assumed proportional limit, these curves are approximated by

$$\epsilon_\theta = \frac{pR}{Et}\left(1 - \frac{\nu}{2}\right)$$

$$\epsilon_\phi = \frac{pR}{Et}\left(1/2 - \nu\right)$$

where

ϵ_θ = strain in the circumferential direction

ϵ_ϕ = strain in the meridional direction

p = pressure (measured)

R = nominal radius = 77.255 in.

t = thickness (measured)

E = modulus of elasticity = 27×10^6 psi

ν = Poisson's ratio = 0.285

The yield point for the reference curve, marked (Y. P.), was established using the average measured uniaxial 0.2% offset yield values for welded specimens aged with each cylinder, the local thickness at each gage location and assuming no biaxial gain. The proportional limit, marked (P. L.), was assumed to occur at 80% of the yield pressure and the curve between the proportional limit and yield point was faired between these points.

In general, the strain gages behaved as expected. The gages in the meridional direction followed the reference membrane behavior. Because of the known weld peaking the measured hoop strains on the inside surface were greater than the reference strains and less than the reference strain on the outside surface. The difference between measured hoop strain and

TABLE VI

156-INCH DIAMETER CHAMBER CALCULATED ACTUAL STRESS AT 800 PSI

Pair of Gages	ϵ_H, Microinches per Inch	ϵ_L, Microinches per Inch	Meriodional Stress (psi)	Circumferential Stress (psi)
1H, 1L	4355	1026	69,205	138,345
101H, 101L	5740	1103	83,818	180,124
2H, 2L	2728	929	51,845	89,209
102H, 102L	7291	1267	102,489	227,602
3H, 3L	2121	--	--	--
103H, 103L	6740	1175	94,855	210,434
4H, 4L	5132	1027	76,151	161,408
104H, 104L	4399	1091	71,525	140,229
5H, 5L	5288	110	50,332	157,874
105H, 105L	5476	2018	108,616	180,435
6H, 6L	717	1014	36,467	30,299
106H, 106L	7195	966	42,704	222,074
7H, 7L	1611	1120	47,570	57,767
107H, 107L	7448	1157	100,623	231,281
8H, 8L	4190	885	63,553	132,195
108H, 108L	46[illegible]	1282	79,338	149,080
9H, 9L	1870	1188	51,893	66,057
109H, 109L	6580	892	85,034	203,168

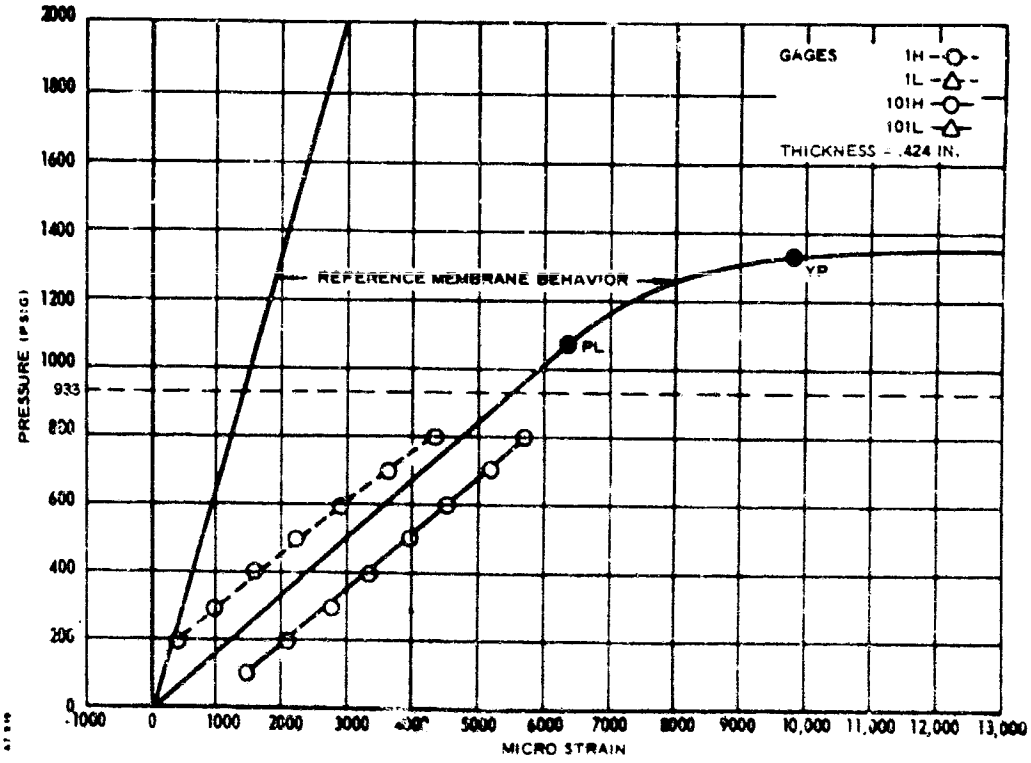

Figure 5 Microstrain versus Pressure, Gages 1H, 1L, 101H and 101L. Thickness = 0.424 Inch

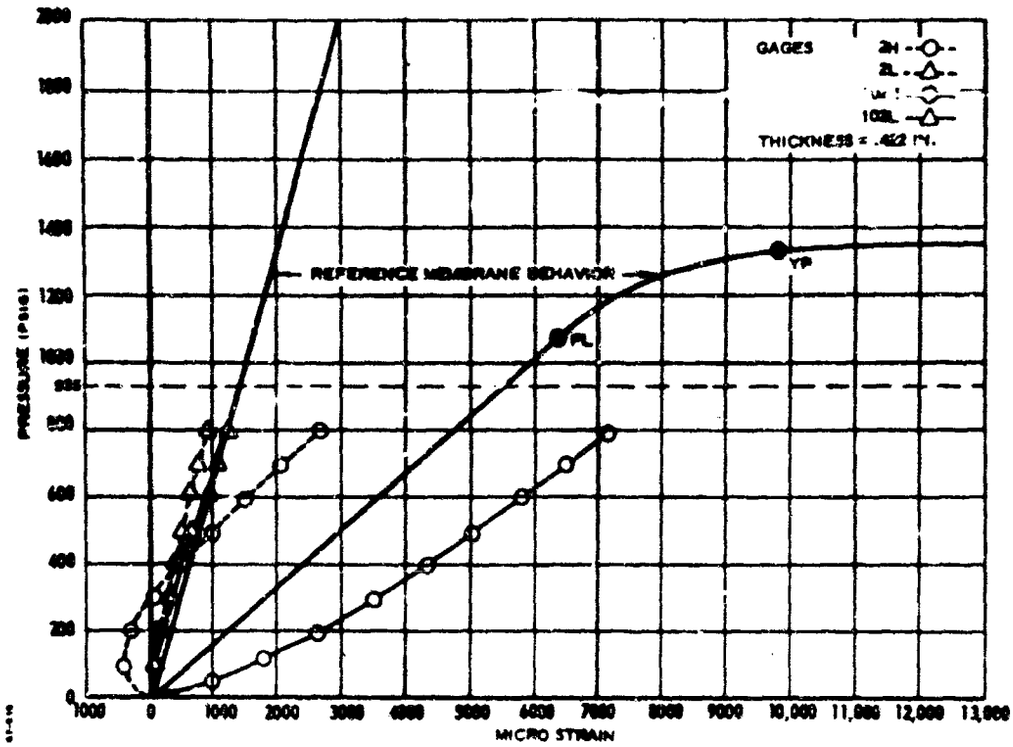

Figure 6 Microstrain versus Pressure, Gages 2H, 2L, 102H and 102L. Thickness = 0.422 Inch

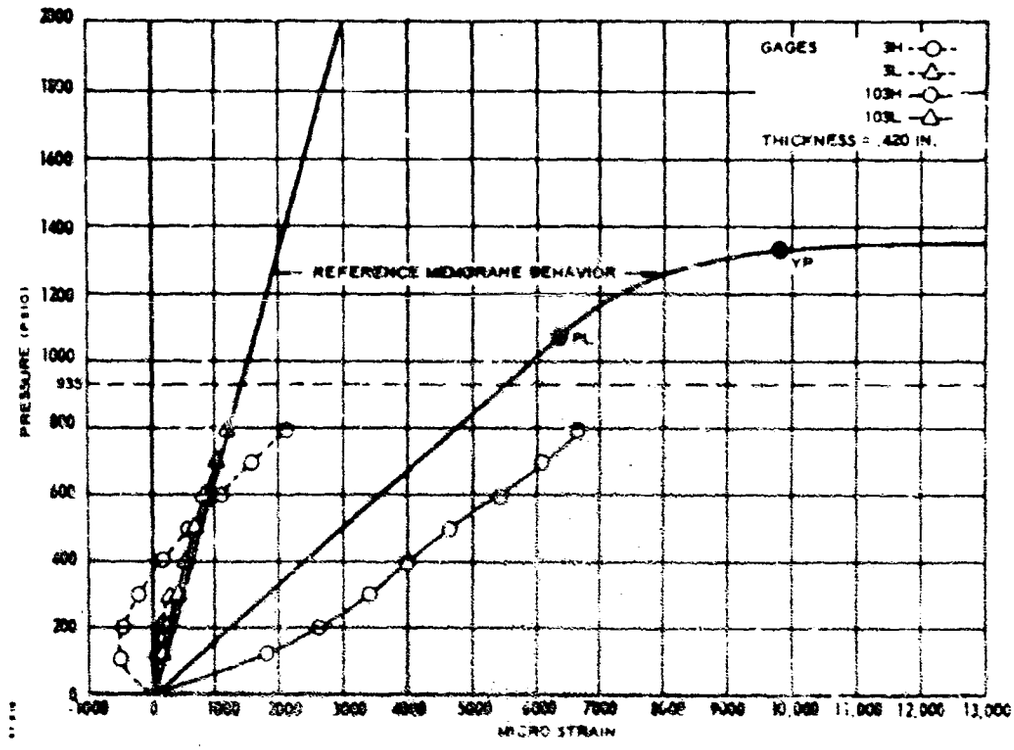

Figure 7 Microstrain versus Pressure, Gages 3H, 3L, 103H and 103L. Thickness = 0.420 Inch

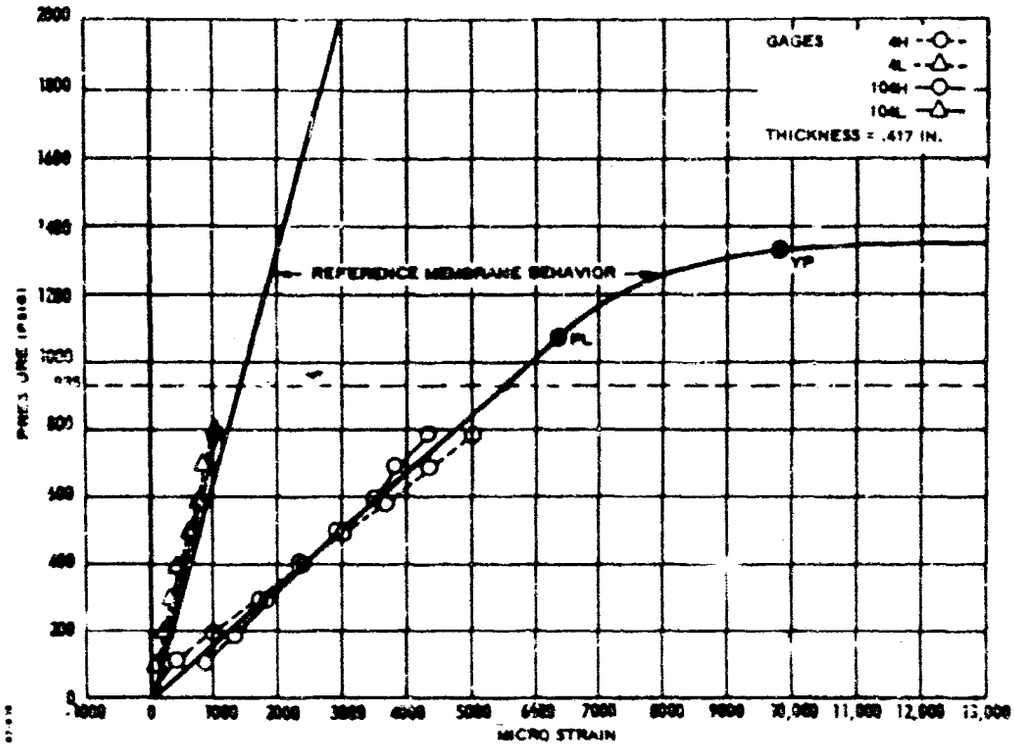

Figure 8 Microstrain versus Pressure, Gages 4H, 4L, 102H, and 104L. Thickness = 0.417 Inch

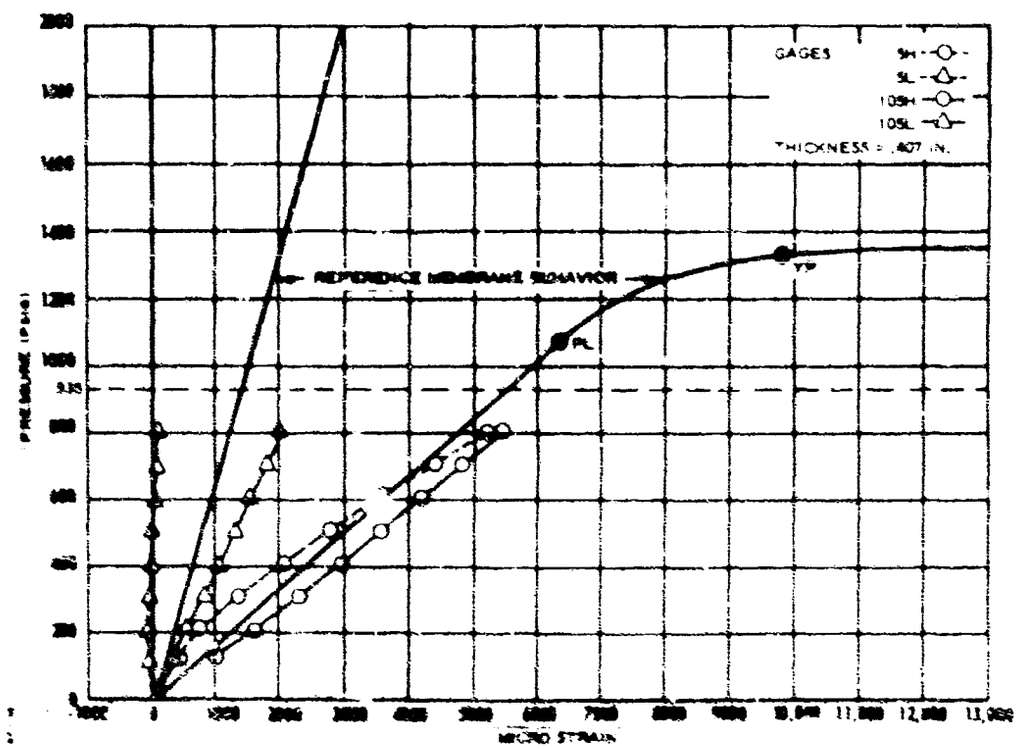

Figure 9 Microstrain versus Pressure, Gages 5H, 5L, 105H and 105L. Thickness = 0.407 Inch

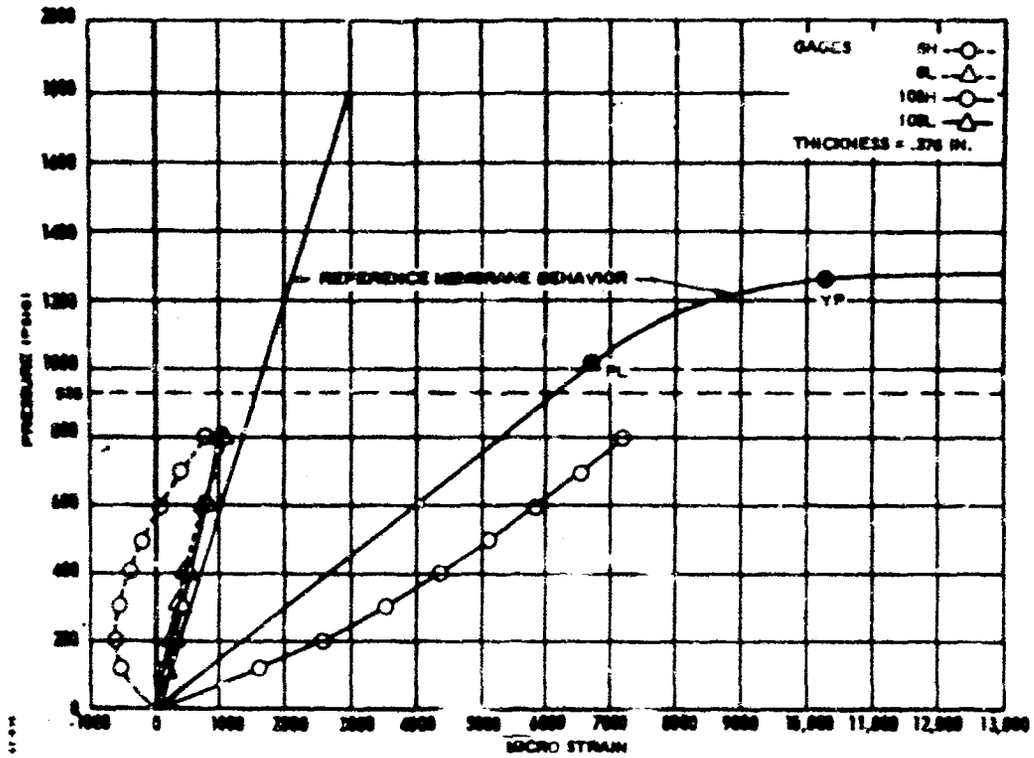

Figure 10 Microstrain versus Pressure, Gages 6H, 6L, 106H and 106L. Thickness = 0.376 Inch

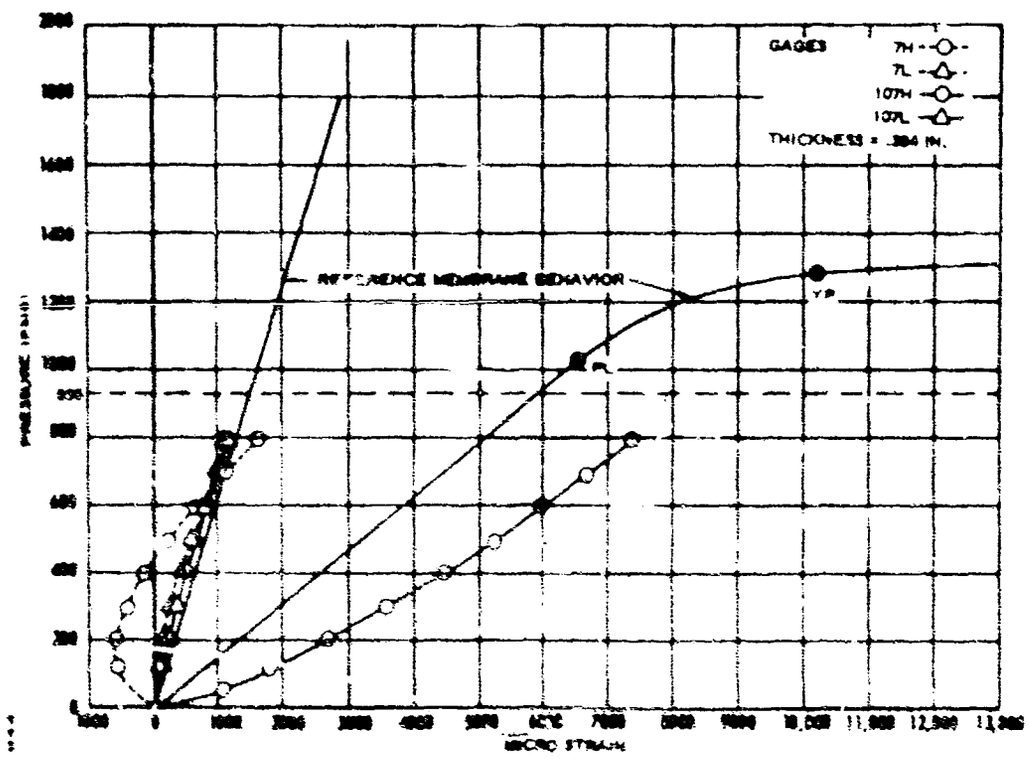

Figure 11 Microstrain versus Pressure, Gages 7H, 7L, 107H and 107L. Thickness = 0.384 Inch

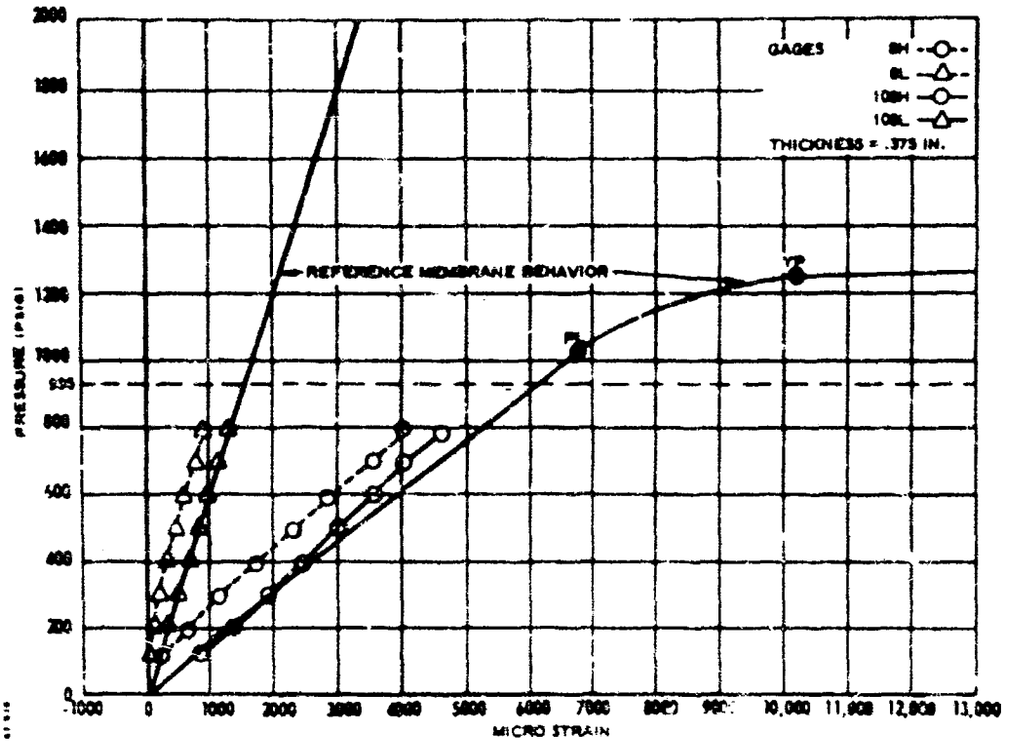

Figure 12 Microstrain versus Pressure, Gages 8H, 8L, 108H and 108L. Thickness = 0.375 Inch

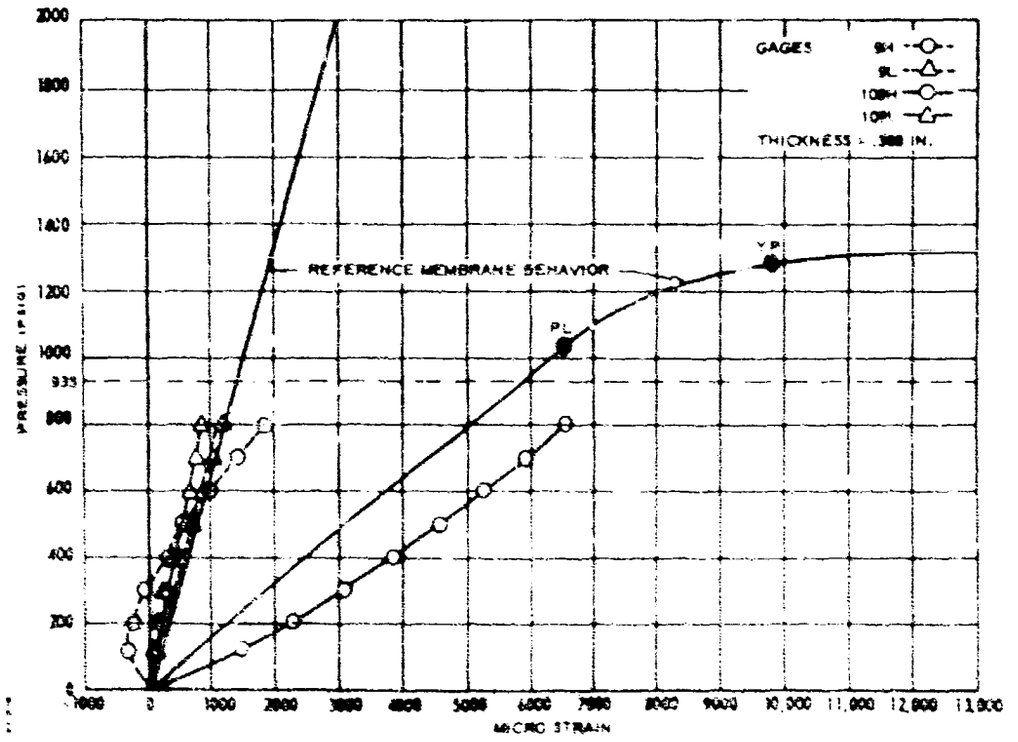

Figure 13 Microstrain versus Pressure, Gages 9H, 9L, 109H and 109L. Thickness = 0.388 Inch

the reference strain also decreased with distance from the longitudinal weld. This can be seen clearly by observing the behavior of the gages at location 1 to 4 (Figures 5 through 8). Gages 2 and 3 were located one inch from the longitudinal weld and gages 1 and 4 were two and four inches from the longitudinal weld, respectively. The least discrepancy from the reference membrane behavior occurred at gage location 4 which was the furthest from the longitudinal weld.

The maximum strain occurred in gage 107H and was 0.745% at 800 psi. All strain was below the reference yield point strain but the inside loop gages at locations 2, 3, 6 and 7 exceeded the reference proportional limit strain. This indicated that a small amount of permanent, unrecoverable, deformation had occurred at these locations. As these gages were at a distance of one inch from the longitudinal weld, a somewhat greater amount of permanent deformation is expected to have occurred at the weld centerline.

Table VI presents stress values calculated from the measured strains.

SECTION V

FAILURE ANALYSIS

1. INTRODUCTION

Concurrent analyses conducted by LPC, SPS Laboratories, and Mellon Institute have not only pinpointed the precise failure mechanism, but have focused attention on preventative steps which could have even more far-reaching value than the original objectives. To this end, detailed data and preventative recommendations are given.

2. POST-TEST CONDITION AND FAILURE SEQUENCE

The precise mechanism and sequence of component failure in the hydroburst chamber is deduced on the basis of visual observation of the fractured remnants, location with respect to original position, and optical and electron microscopic examination of the fracture surfaces.

The chamber was supported by the end skirts upon cradles, with restraining cables placed over the unit to limit risk of damage to bay structures. Failure originated in the bolts on the bottom of the 120-inch diameter adapter-to-case bolt circle, inducing movement of the adapter forging with respect to the aft chamber section, with resultant shear of the bolts. It was noted that the origin of failure for bolts showing a sunburst-pattern fractured face was not oriented uniformly with regard to the bolt circle perimeter, indicating localized corrosion and multiple incipient failure origins. Figure 14 indicates the type and location of bolt failures, and depicts a typical shear to tensile mode transition.

The release of the pressure caused by the bolt fracture created reverse bending of the membrane, and movement of the assembly upward into the restraint cables. Pronounced markings from the cable were evident on top of the case. The severe ovality produced cracking of the clevis joint forging and barrel section in the region of maximum curvature. Figure 15 indicates the relative position of the clevis joint forging fracture with a close-up view shown in Figure 16. The force exerted on the pin retainers caused shearing of the pin retainer bolt heads and ejection of the tapered pins when the chamber reverse bent and impacted on the supporting structure. The chamber halves separated with considerable force.

The movement of the aft segment caused a sharp impact of the adapter forging against a steel restraining cable, resulting in a fracture of the adapter forging adjacent to the small diameter flange. The origin of this failure in shown in Figure 17. Chevron patterns indicated direction of fracture path to the outer bolt circle, where secondary fracture origins resulted in a further fragmentation of the adapter forging and membrane. Secondary failure origins were found at the threaded bolt holes and at sharp cornered machine cuts, with five such secondary fracture origins located. The fractured adapter forging remnants attached to the aft segment, with the aft closure lying nearby, are shown in Figures 18 and 19. The assembled

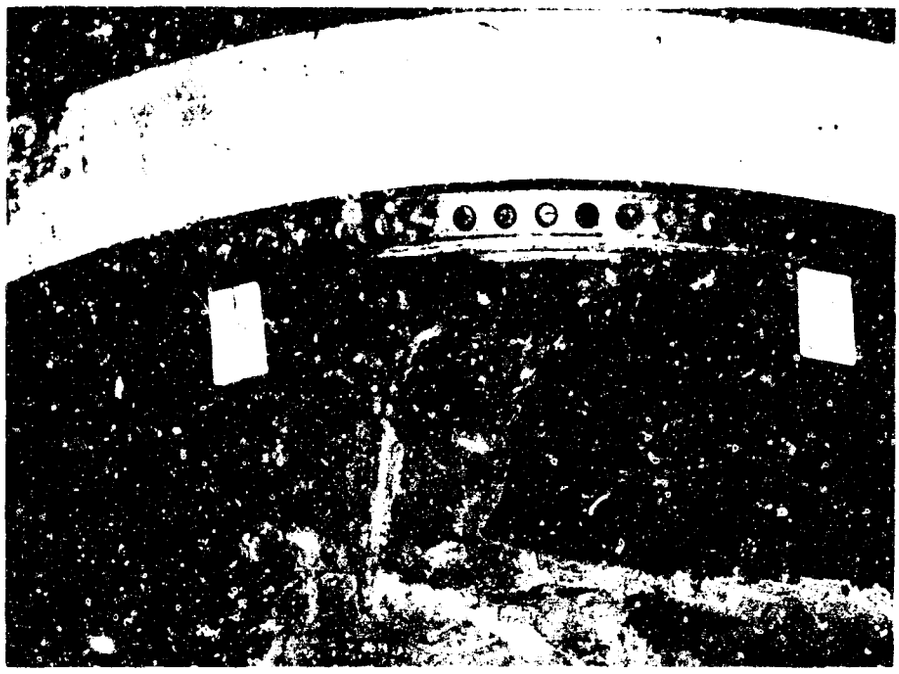

Figure 14 Type and Location of Bolt Failures, Depicting a Typical Shear to Tensile Mode Transition

Figure 15 Aft Section of 156-Inch Diameter Chamber showing Oval Condition after Hydroburst and Cracked Clevis Joint Forging on Left-Hand Side

Figure 16 Close-up Of Clevis Joint Fracture

Figure 17 Primary Origin of Failure of Adapter Forging

Figure 18 One View of Adapter Forging Remnant on Aft Segment--Closure Lying on Ground

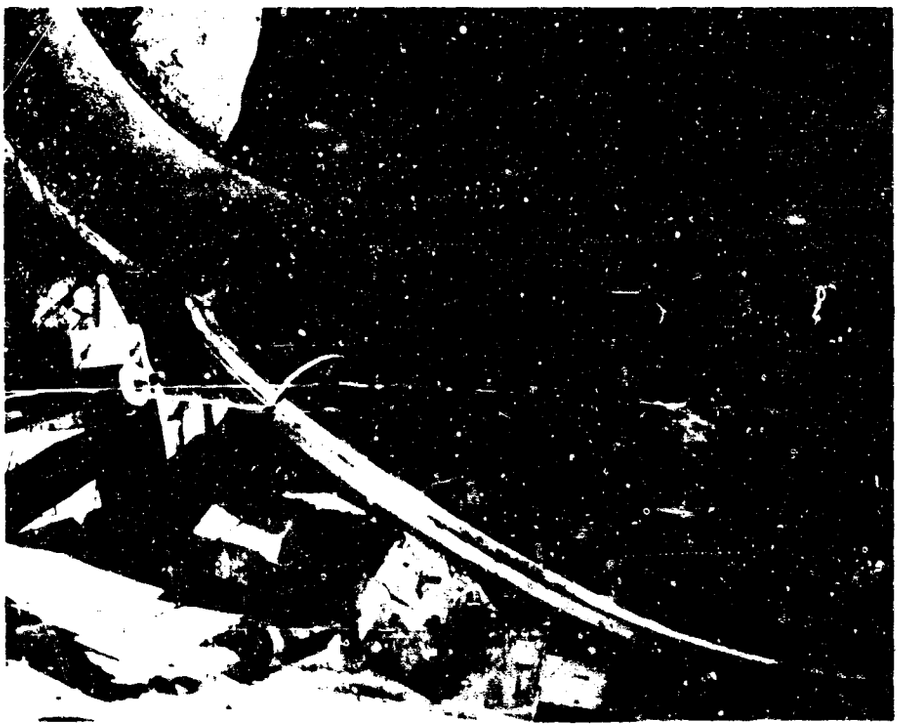

Figure 19 Close-up View of Adapter Forging Remnant on Chamber and Attached to Closure

sections of broken adapter forging are shown in Figure 20. The location of bolts is correlated with the numbering system adjacent to the large diameter flange. The primary origin of failure in the adapter forging was associated with a ductile dimple rupture pattern as determined by electron fractographs performed on the area. The mechanism for the crack propagation triggered by impact of the forging against the restraining cable was predominantly microvoid coalescence.

The movement of the forward segment caused a shearing of the skirt fillet weld joint where chamber and concrete pad were in contact. The crack at the fillet weld progressed during subsequent removal of the chamber to the stage where complete separation of the skirt and forward segment occurred. Several secondary failure origins were found along the fillet weld where plate delaminations were present.

3. FAILURE DISCUSSION

A macroexamination of the bolts disclosed that thread damage had occurred on many of the bolts; i. e., the crests of the threads were flattened (see Figure 21). In addition, many of the fractured bolts provided for this investigation exhibited pitting on both the shank and the threads (see Figure 22). Bolt number 12 exhibited a seam along the crest of the threads, and bolt number 28 contained six radial checks on the crest of the thread. The bolt numbers reflect positions on the bolt circle. Examination of the fractured faces revealed that the failure mode of the bolts varied from 100% tensile to 100% shear. Figures 23 through 26 are typical photographs of these two conditions. The tensile fracture faces exhibited a fine grained structure typical of 5% chromium tool steel. The bolts fractured generally in the root of the threads $\frac{1}{8}$ to $\frac{1}{2}$ inch from the shank. As illustrated in Figure 27, the majority of the tensile failures nucleated at a point and propagated across the bolt. The fractured face of these bolts is similar to the fractured face of high strength bolts in which stress corrosion cracking was induced under laboratory conditions.[1]

4. MICROSTRUCTURE

Eight bolts that exhibited the tensile fracture and eight bolts that did not fail were selected for longitudinal microscopic studies. The appearance of the typical tensile fracture exhibited by the eight selected bolts is illustrated in Figure 27. Typical examples of bolts exhibiting the tensile fracture were investigated because the primary failure mode for this application would be in tension. Therefore, all the bolts exhibiting shear type fractures (Figure 24) were secondary failures, and thus not investigated. All of these bolts exhibited the normal hardened and tempered martensitic structure of 5% chromium tool steel. Figure 27 illustrated this structure at different

[1] Standard Pressed Steel Company, Stress Corrosion Cracking of High Strength Bolting, By C. S. Lin, J. J. Laurilliard, A. C. Wood, SPS Laboratories, Jenkintown, Penn., June 1966.

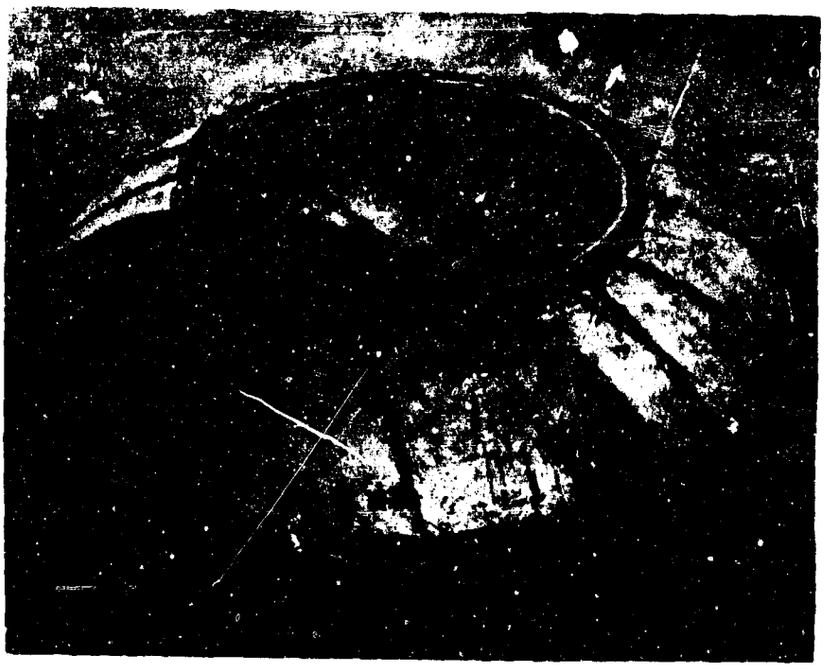

Figure 20 Assembled Fragments of Adapter Forging

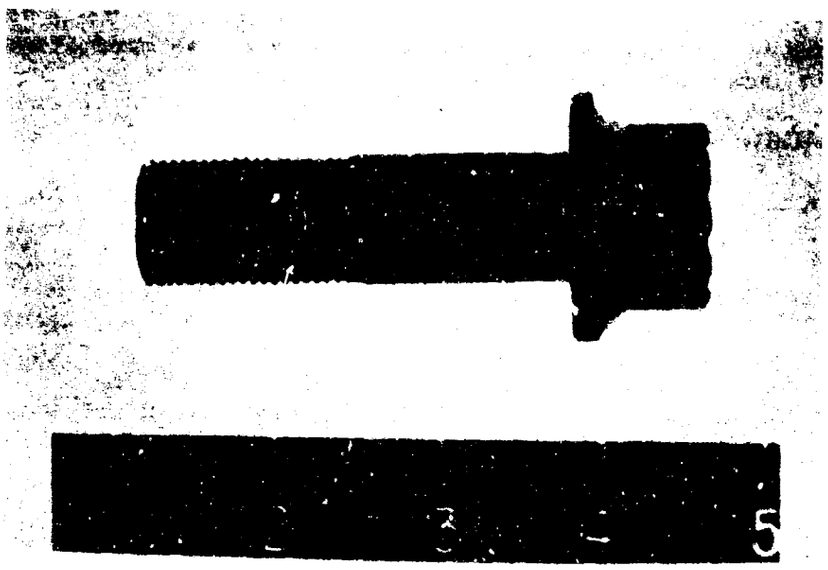

Figure 21 Thread Damage Found on Many of the Bolts

Figure 22 Pitting Experienced by Many of the Bolts

Figure 23 Tensile-Type Failure which Nucleated at a Point and Propagated through the Bolt

Magnification: 150X

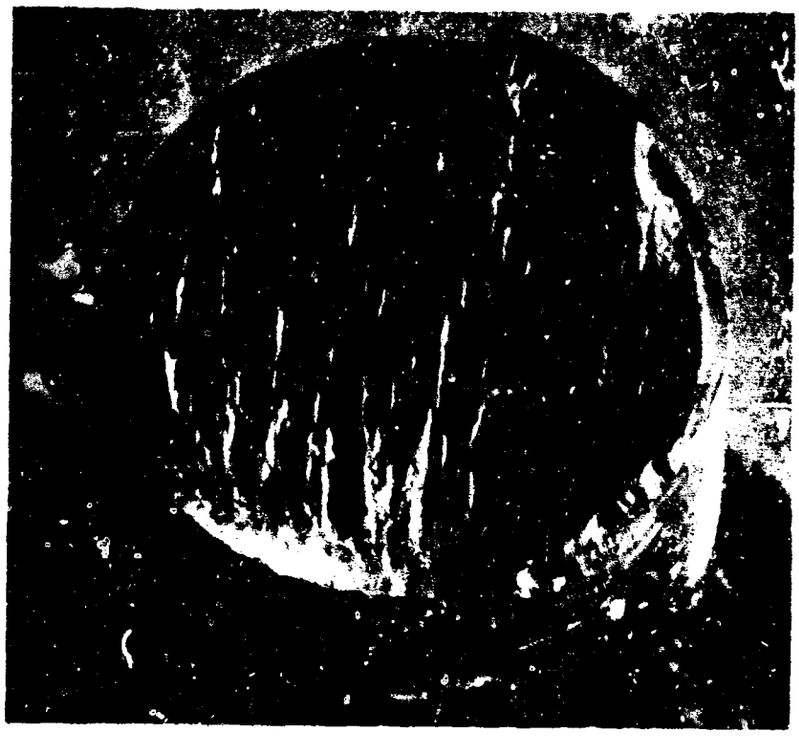

Figure 24 Shear Type Fracture Exhibited by Many of the Bolts

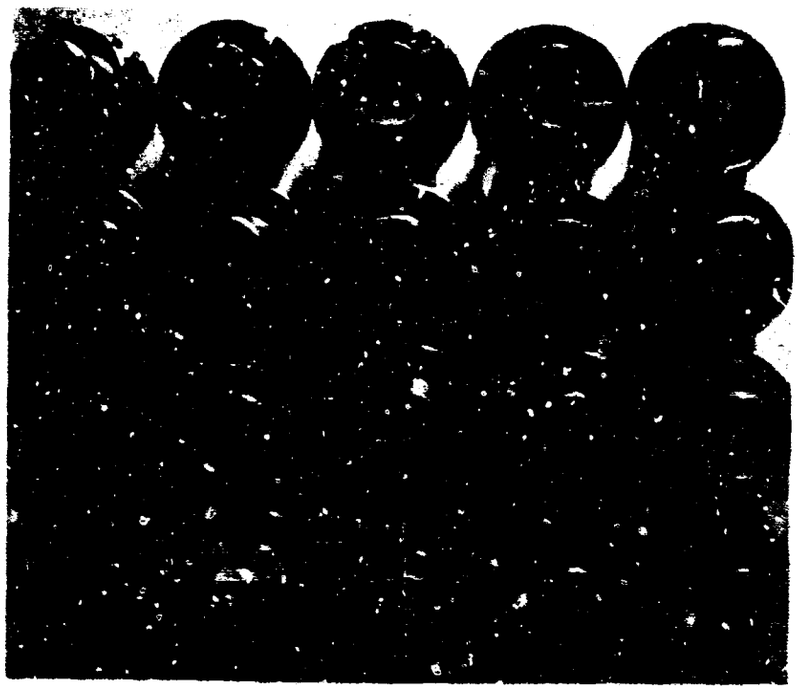

Figure 25 Typical Photograph of Cupped Tensile Failure Mode, 20 Bolts, Batch 5

Figure 26 Typical Photograph of Shear Failure Mode, 16 Bolts, Batch 5

magnifications. No evidence of carburization or decarburization was found. The normal cold work initiated by the thread rolling operation was visible. Manufacturing defects were noted on the crest of the threads in both the fractured and the whole bolts. Figure 28 is a photomicrograph of a defect on the crest of the thread which was caused by the thread rolling operation (note the plating on the surface of the thread). Figure 29 is a photomicrograph of a similar defect at a higher magnification. The plating, as revealed in Figure 28, was not visible on all surfaces of the bolts. It appeared to have been abraded from the thread area and part of the shank area. Bolt 28, which exhibited the checks on the crest of the threads was sectioned in the transverse direction and revealed that small cracks were propagating from the checks into a parent material (Figure 30). (This finding is also noted in the Mellon Institute report in a later section.) This polished area also revealed that cracks were propagating into the parent material from the crest of the thread (Figure 31). As Figure 32 reveals, secondary cracking occurred perpendicular to the fractured surface and on the primary fractured face. Another secondary crack was located in the root of the first thread below the fracture (Figure 33).

"A"

Magnification: 150X Etchant: 2% Nital

"B"

Magnification: 320X Etchant: 2% Nital

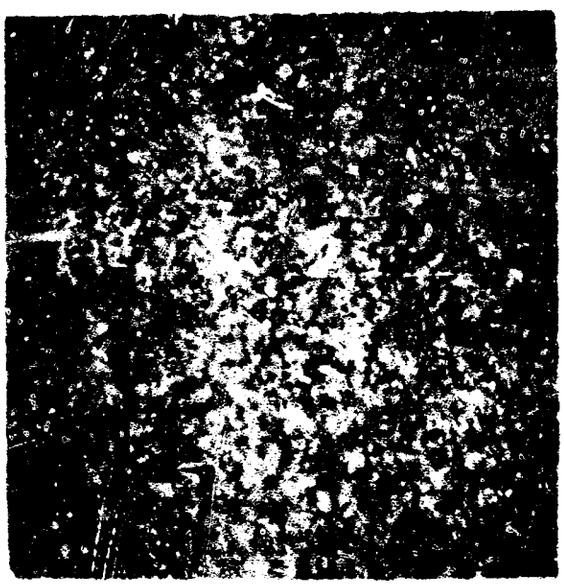

Figure 27 Photomicrographs of the Normal Hardened and Tempered Martensite Exhibited by the Bolts

Magnification: 150X

Etchant: 2% Nital

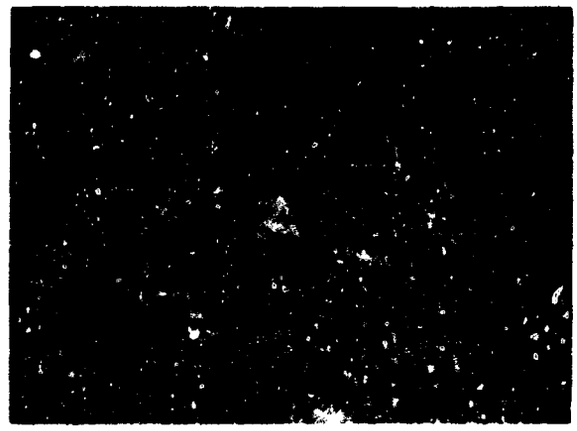

Figure 28

Thread Rolling Defec in Crest of a Thread (Note plating on thread surface)

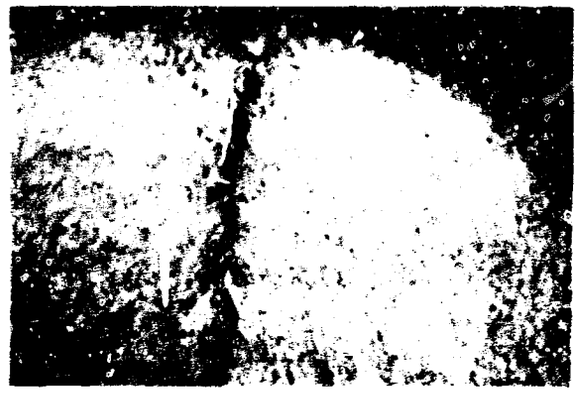

Figure 29

Another Thread Rolling Defect in Crest of Thread

Magnification: 320X

Etchant: 2% Nital

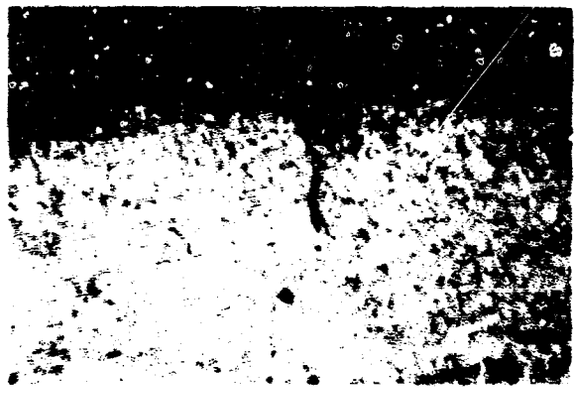

Figure 30

Transverse Microstructure Crack Propagating from a Check in the Crest of a Thread

Magnification: 150X

Etchant: 2% Nital

Figure 31

Transverse Microstructure--
Crack Propagating from
Crest of a Thread

Magnification: 150X

Etchant: 2% Nital

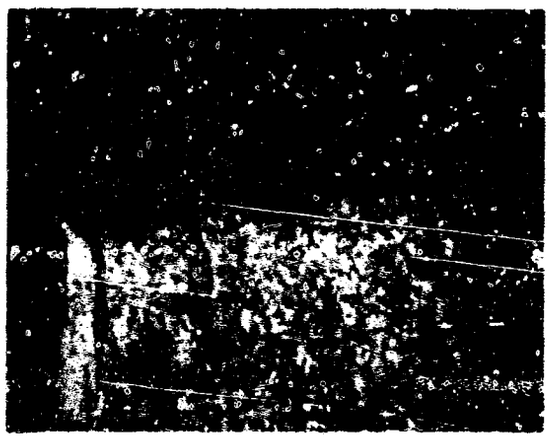

Figure 32

Secondary Cracking Noted at
the Origin of the Fracture

Magnification: 150X

Etchant: 2% Nital

Figure 33

Secondary Crack in the Root
of the First Thread under
the Fracture

Magnification: 320X

Etchant: 2% Nital

5. TENSILE TEST

Seven of the sound bolts which were removed from the fractured motor case were tensile tested. The results, tabulated below, indicate a high range of values:

Bolt No.	Tensile Load (lb)	Ultimate Tensile Strength (psi)	Psi Required	Hardness (Rc)
2	112,700	291,200	260,000	53
6	112,200	289,900	260,000	52
9	112,700	291,200	260,000	51
16	105,200	271,800	260,000	52
17	111,100	287,100	260,000	53
22	111,700	288,600	260,000	52
46	112,700	291,200	260,000	53

The hardness of both the sound bolts and fractured bolts was taken, and without exception, the hardness ranged between Rockwell "C" 51 to 56.

With the exception of the stress corrosion cracks previously noted in the microscopic examination, the defects described in this report were either initiated by the bolt manufacturing process or are secondary cracks i.e., caused by the failure. The location and nature of these defects disclosed that they did not initiate the hydrotest failure. The thread damage, as illustrated in Figure 21, is believed to have been caused by the failure. Other than the above defects, the bolts complied with specification requirements. The fact that the nickel-cadmium plating was worn off the threads and part of the shank is believed to have contributed to the premature failure of the bolts. The absence of plating permitted pits to form as illustrated in Figure 22, creating stress risers and susceptibility to stress corrosion cracking.

SPS Laboratories (Standard Pressed Steel Company, Jenkintown, Pennsylvania) performed examination of several of the failed bolts. Unused bolts of the same lot (EWB 926-12-20, Lot No. 1) were also obtained from stock, checked for metallurgical properties, and tested for bending properties in tensile and fatigue using a 3° angle washer under the nut. A 120,000-pound capacity Tinius Olsen Testing Machine was used for tensile tests and a 50,000-pound capacity Ivy Fatigue Testing Machine was used for fatigue tests.

The examination showed severe thread damage on the failed bolts. (Figure 34, 35, and 36). Microscopic examination revealed that failures occurred at the corroded root of the bolt threads. No rust appeared on the shank areas.

Figure 38 illustrates the cracking fracture initiated at a corrosion pit in the thread root area of a used bolt. Secondary cracking was found to have propagated nearly perpendicular to the fastener surface as shown in Figures 40 and 41. It is probable that these failures occurred by stress corrosion cracking with high localized loading.

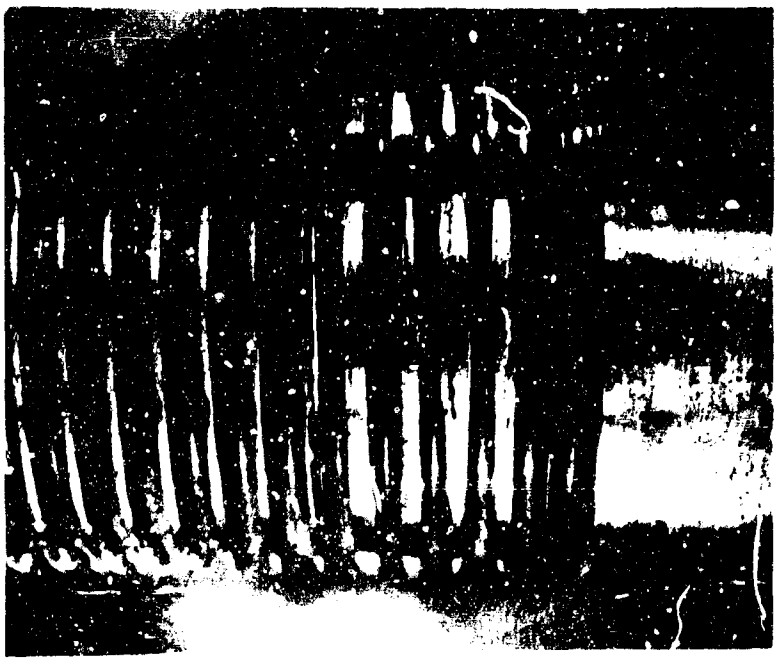

Mag. X3.6 7142R

Figure 34 Example of Severe Thread Damage of Unfailed Bent Part

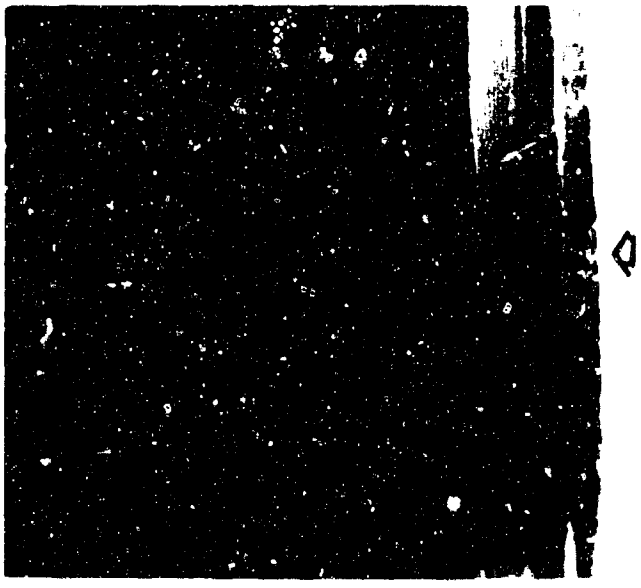

Mag. X9 7141R

Figure 35 Thread Damage at Original Point of Cracking (Failure) Indicated by Arrow

Mag. X8 7131R

Figure -36- Thread Failure As-Received. Note Pitted Shank and Damaged Thread Area

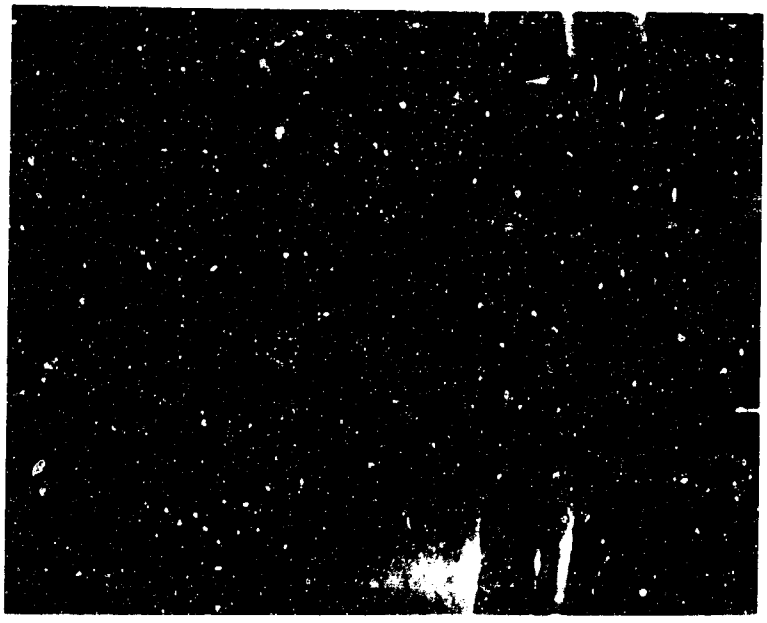

Mag. X8 7132R

Figure 37 After Strip of Plating - Note Pitted Shank and Thread Area

Mag. X3.5 7130R

Figure 38 Fracture Face of Failed EWB26-12 As-Received

Mag. X3.5 7150R

Figure 39 Fracture Face of Unused EWB26-12 Following a Tensile Test With a 3° Angle Under the Nut

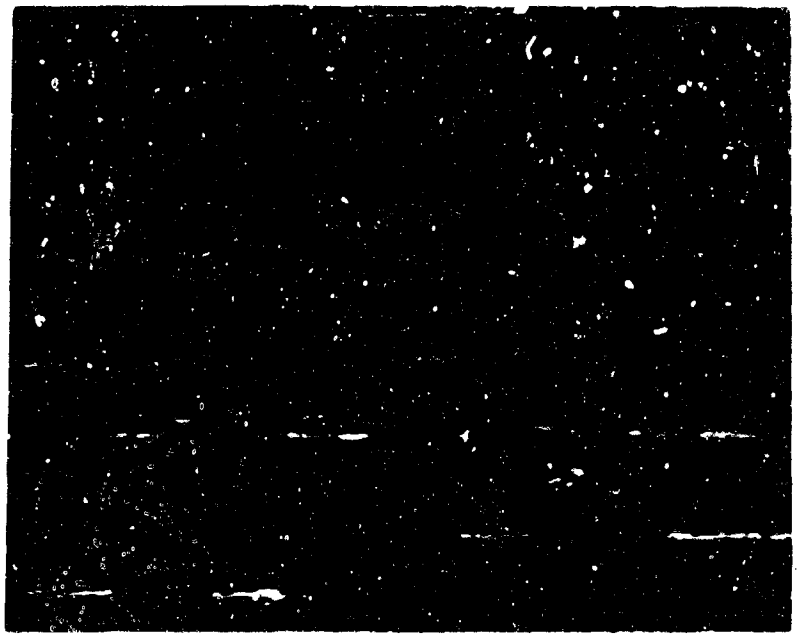

Mag. X250
Nital Etchant

7139R

Figure 40 Secondary Cracking From Fracture Surface

Mag. X250
Nital Etchant

7140R

Figure 41 Final Section (Opposite Origin) of Fracture - Secondary Cracking. Note Shear Lip at End of Fracture.

Pitting was found on the shank and thread of the failed bolts. (Figures 36, 37, and 42). This could possibly act as a stress raiser and contribute to bolt failure.

A Tukon microhardness survey of failed bolts gave no evidence of carburization or decarburization. Tukon measurements (200 gram D.P.H.) averaged 583.3 (Rc 54.3) and 578.9 for the core (Rc 54.0).

Tensile tests on unused bolts from stock indicate no significant difference in bolt strength tested with or without a 3^0 angle washer to compare bending effects. Thread failures occurred at 109,000 pounds using a 3^0 angle washer under the nut and at 107,000 pounds without a washer.

Fatigue tests were conducted on unused bolts from stock at a load of 48,100 pounds (R = 0.1) with and without a 3^0 angle washer under the nut to compare bending effects. Head failures resulted at 71,000 cycles for the bolt tested without an angle washer and at 6000 cycles for the bolt tested with the angle washer.

Magnification: 250X

Nital Etchant

Figure 42 Origin of Failure Area -- (As-Received). Note Pitting of Thread Area

As shown in Figure 39, the resultant tensile fracture surface had no clear cracking nucleus and radial paths as had been observed on the service failed bolts.

Microscopic studies of bolts obtained from stock which were corroded by exposure to water for 24 hours did not duplicate the secondary cracking findings when fractured in tensile or fatigue tests. (Figures 43 and 44).

6. MELLON INSTITUTE ANALYSIS

Under subcontract to LPC, Mellon Institute performed electron fractographic examination of selected bolts and microscopic evaluation of the secondary forging fracture surface. Due to the exceptional quality of the electron microscopy, the Mellon report is included as subsection 8, below.

7. BOLT MATERIAL CONSIDERATIONS

The bolt failure cannot be ascribed specifically to stress corrosion or hydrogen embrittlement as these mechanisms of failure are quite similar, except where evidence of corrosion is present. Stress corrosion cracking can be intergranular to transgranular, and may occur concurrently with hydrogen embrittlement where the alloy is susceptible thereto and atomic hydrogen is evolved during the corrosive action. Stress corrosion cracking is quite frequently marked by secondary cracking and thus distinguished from hydrogen embrittlement failure. However, where secondary cracking or corrosion products are not in evidence, the two are indistinguishable.

C. S. Lin and others recently published findings on stress corrosion cracking of high-strength bolting. The study involved H-11, 4340, and 300 grade 18% Ni maraging steels, various manufacturing processes, platings, and test conditions. This information, while not directly related to the failure analysis, is presented for understanding and possible control of the factors relating to stress corrosion failure. Significant findings were as follows:

(1) There is a lower level of applied stress, approximately 50% of the proportional limit stress, below which no stress corrosion failure will occur.

(2) Of the materials tested, 18% nickel maraging steel bolting material was the least susceptible to stress corrosion failure.

(3) Bolts of any material below 200,000 psi ultimate strength did not fail in testing.

(4) Bolt coating was influential in reducing the incidence of bolt failure; electroplated nickel and electroplated cadmium-diffused afforded the most effective protection.

(5) The influence of thread rolling after heat treating was significant in increasing the bolt life.

(6) The effect of decarburization on bolt life was not significant.

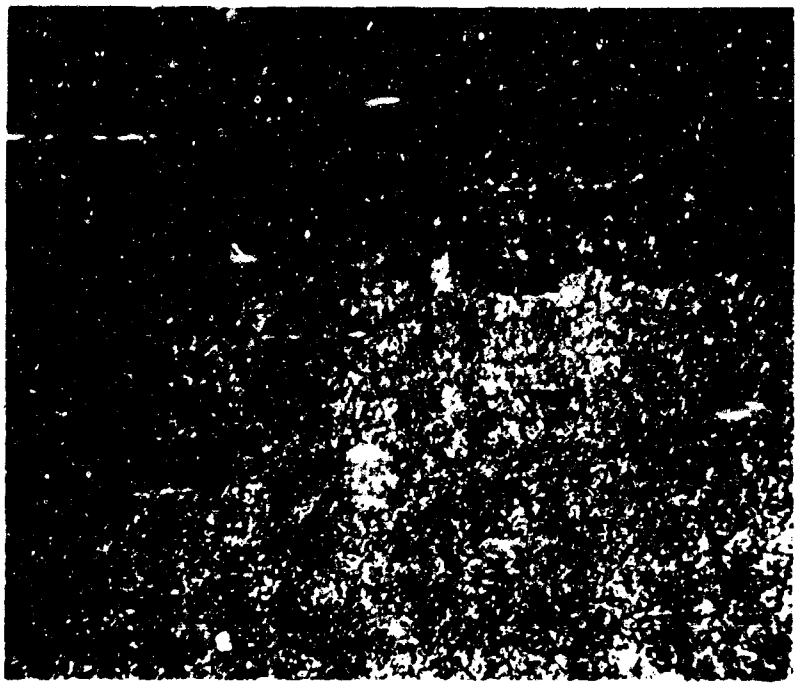

Mag. X250 7148R
Nital Etchant

Figure 43 Tensile Test Specimen - Unused EWB26 Bolt

Mag. X250 7149R
Nital Etchant

Figure 44 Tensile Test Specimen after 24-Hour Exposure to H_2O (Unused EWB26)

8. MELLON INSTITUTE REPORT

a. Introduction

This report presents the results of the investigations conducted at Mellon Institute to determine the cause of suspected premature failure of the Type H-11 steel bolts used to secure the adapter forging on the 156-inch-diameter maraging steel booster case. Due to their qualitative nature, proper interpretation of the results obtained in studies of this type is of primary importance. Thus, in preparing the comments given in this report the investigators at Mellon Institute have relied strongly on the standards presented in the Electron Fractography Handbook.[2]

b. Experimental

(1) Material

Approximately thirty-five fractured bolts of H-11 steel and one section of the failed maraging steel adapter forging were received at Mellon Institute. The fracture surfaces of the majority of the bolts showed signs of oxidation. In the severe cases the surfaces were completely covered with rust, while, in general, attack was not appreciable.

Visual examination of these samples resulted in the choice of eleven (11) bolts as representative of the lot. The criterion of selection was a peculiar flat fracture on the bolt surface at the point of fracture origin. In addition, a few samples without apparent unique features at the origin were chosen. Bolts which obviously fractured in total shear were not examined.

Study was, therefore, limited to the eleven (11) bolts and one section from the forging.

(2) Procedure

(a) Electron Fractographic Analysis

Due to the surface condition of the fractured samples elaborate cleansing measures were necessary to render them suitable for replication. The preparation technique included immersing the bolts in an acetone bath, kept turbulent by use of a mechanical vibrator. Minimum time of immersion was one hour. The object of this treatment was to remove any free residues and also, if possible, to loosen the oxide film on the fracture surfaces.

Then, cellulose acetate replicating tape moistened with acetone was pressed onto the surface, allowed to dry, and then stripped

---

[2] A. Phillips, et al, "Electron Fractography Handbook", Air Force Materials Laboratory, Wright-Patterson Air Force Base, Ohio, AD 612-912, 31 January 1965.

off. By repeating this procedure all of the visible oxides were removed from the sample. Generally, six repetitions were sufficient to accomplish this end. Serious examination of the samples by electron fractographic techniques started only after the fracture surfaces had been thus repaired.

All replicas examined were of the plastic-carbon two step type. Cellulose acetate tape approximately five mils thick was used as the replicating plastic. A generally accepted replicating technique was employed. This technique has been outlined in subsection 9, following.

Because of the distinct chevron patterns on the fracture surfaces of all the bolts, it was concluded that after the initial fracturing, through fracture proceeded rapidly. Therefore, replication was confined to the area of initial fracture, or approximately an area bounded by the edge of the bolt at the point of fracture origin and a chord drawn ¼ inch from that point towards the center of the fracture surface.

The point of fracture origin becomes apparent by examining the chevron patterns, the textures of the fracture surface, and the variation in size of the edge shear lips. At least six replicas from the initial fracture area of each bolt sample were processed and examined.

The fracture surface of the forging sample was repaired in the same manner outlined for the bolts and several replicas taken from the area of suspected fracture origin were examined.

(b) Fracture Profile Examination

Certain of the bolt samples, following electron fractographic study, were sectioned in a manner such that fracture edges could be microscopically examined. Particular attention was given to the fracture origin.

c. Results

(1) Electron Fractographic Analysis

The results of this portion of the study are presented in Figures 45 through 107. To limit the lengthy discussion and repetition in presentation, the "lead-off" page to each group of electron fractographs, representing the work on one bolt, gives the following information:

A. Bolt identify if known.
B. Photograph of the fracture surface.
C. Description of the fracture appearance.
D. Classification of the electron fractographs.

The job of determining the exact cause of a failure by electron fractography is an extremely complex one. The reason is that the mechanism of fracture propagation can be very similar in failures caused by a variety of conditions. To help the reader understand this problem and also as an aid in following the classification of the electron fractographs, portions

of the section dealing with environmental effects on fracture modes given in the Electron Fractography Handbook are recommended.

Thus, classifications of the fractographs presented in this report will be limited to an identification of the most probable mechanism of fracture propagation, plus, pointing out features peculiar to a particular condition of failure.

(2) Fracture Profile Examination

Metallographic samples were prepared from bolts identified as LPC Codes 2, 86, and 95. The photomicrographic results obtained from the microscopic examination of these samples are given in Figures 108, 109, 110, and 111.

The results obtained from bolt sample 86 are shown in Figure 108. The profile of the fracture origin, 108(a) and 108(b), show the brittle nature of the fracture at the point of initiation, apparent from the flatness of the fracture and the presence of a brittle crack extending in a direction approximately perpendicular to the fracture path. The photomicrograph given in Figure 108(c) is an example of the condition present around all of the threads in the sample, namely, a deformation band conforming to the thread geometry. A hair-line crack found in the deformation band associated with the thread immediately below the fracture is shown in Figure 108(d).

The point of origin of the fracture in bolt sample LPC 2 is shown in photomicrographs (a) and (b) in Figure 109. These represent the two halves of the sectioned bolt. As can be seen, the fracture initiated very close to the root of a thread. Visual examination of most of the bolts studied also showed the thread root region to be the most frequent point of fracture initiation. Higher magnification photomicrographs (c) and (d) in Figure 109, show the fracture profile at the origin in more detail. Apparent is the brittle nature of the fracture at its point of initiation, particularly so in Figure 109(c). Again, brittle cracking in a direction perpendicular to the fracture path can be seen.

The appearance of the fracture origin, shown in Figure 109 in the etched condition, is given at 100X magnification in Figure 110(a). The deformation zone is readily apparent. Cracks parallel to the direction of elongation in the deformation band associated with the first thread below the fracture in sample LPC 2, is shown in Figure 110(b).

Figure 111 is a photomicrograph of the root of the thread immediately below the fracture in bolt sample LPC Code 95. A fine network of cracks can be seen penetrating into the cadmium plate still adhering to the bolt. Thorough examination of the bolt samples showed that in many cases the cadmium plate was either partially or totally removed from the area around the thread roots.

d. Discussion

A study of the history of the H-11 steel bolts reveal[illegible] they were (a) threaded by a rolling technique and subsequently heat tre[illegible]

LOCKHEED PROPULSION LIBRARY

cadmium plated and (c) used repeatedly to secure the adapter section on the LPC 156-inch-diameter maraging steel booster case during developmental testing.

The investigations conducted at Mellon Institute have shown that (1) all bolts except those which failed in total shear had a point of fracture origin located at one edge, (2) the point of fracture origin was generally located at the root of one of the threads, (3) the fracture was more brittle at the point of origin than elsewhere on the sample, as detected from visual observations of the fracture textures and microscopic observations of fracture profiles, (4) the mechanisms of fracture propagation in the area of fracture origin in the majority of the bolts examined were predominantly two; intergranular rupture and quasi-cleavage, mechanisms which can be associated with a number of brittle fracture conditions, and (5) occasional features were found on the electron fractographs which are associated with stress corrosion or hydrogen embrittlement failure conditions.

Having considered all available information, a mechanism of failure can be suggested. It is felt that prior to through (or complete) fracture, many of the bolts had formed an area of initial brittle fracture. Once this area had grown to critical dimensions fracture propagated rapidly by a mechanism of sharp-notched tension.

The exact mechanism of the initiation and propagation of brittle fracture cannot be stated. However, the possibilities which evolve from the known facts and experimental indications can be proposed. The fact that fracture always initiated at an edge of the bolt suggests that some condition existed at this point prior to failure which acted as a stress raiser. The most obvious answer is a crack or some other type of defect.

Conditions which might allow for a crack to initiate and grow at some preferred point on the bolt are numerous. Those conditions which must be considered in this case are hydrogen embrittlement as a result of the cadmium plating technique, stress corrosion (exposure of H-11 steel surface) because of the introduction of some undesirable environment between or during testing, the effect of the stresses and metallurgical phenomena created by the technique of thread rolling and subsequent heat treatment, and the possibility that all three conditions act in harmony to induce brittle fracture.

Another factor which must certainly be considered is the effect of handling the bolts between testing on inducing susceptibility to cracking by the conditions given above. For example, damage to the cadmium plating in the root area of a thread could set up ideal conditions for corrosive attack, especially if the bolts are not carefully stored between testing.

The predominant mechanism of fracture propagation in the area of fracture origin of the forging section was found to be microvoid coalescence, as shown by the dimpled rupture patterns on the electron fractographs. Although some areas showed signs of brittle fracture these were associated with networks of brittle secondary phase particles, commonly found in maraging steel. The brittle particles tend to cleave with the result that surrounding areas show less ductile fracture facets.

e. Conclusions

Conclusions reached from the investigations described above are listed below:

A. All of the bolts examined had an area of fracture origin located at one edge and characterized by flat surface textures and occasional discolorations.

B. The fracture origin was generally located at the root of one of the bolt threads.

C. Examination of fracture profiles and electron fractographs show generally brittle fracture propagation in the area of initial fracture.

D. Features generally recognized as, and presently suggested as being associated with stress corrosion and/or hydrogen embrittlement failure conditions were found in the electron fractographic analysis of the bolt samples.

f. Recommendations

Since this failure is considered to be associated with service life of a structural member, it is important to realize that steps have to be taken to avoid such mishaps. In this connection, bolt specifications relative to the type of material, its heat treatment and microstructure, plus handling techniques must be changed so as to preclude as much as possible, the undesirable effects such as notch-embrittlement, stress corrosion, hydrogen embrittlement. Furthermore, experiments have to be conducted on bolts to simulate service failure conditions in the laboratory and evaluate the different failure modes. Directions to modify bolt specifications can be more realistically developed through such an approach.

Approved,

Respectfully submitted,

G.K. Bhat
Head, General Metallurgy and
Materials Research Group

J.B. Tobias
Project Engineer

9. APPENDIXES TO MELLON INSTITUTE REPORT

a. Appendix I

The cellulose acetate replicating tape is moistened on one side with acetone. The moistened side of the tape is pressed onto the fracture surface using a finger or something else suitable such as a pencil eraser. Once it is apparent that all of the air bubbles have been forced out and good

contact has been made, the plastic is allowed to dry. Generally, the drying time is one hour.

The plastic replicas were reinforced with 200 mesh stainless steel grids. Two techniques of attaching the replicas to the grids were used.

If the fracture area of interest is relatively flat and unobstructed by a shear lip then a stainless steel grid is placed on top of the cellulose acetate and located over this area. By moistening the grid with a small amount of acetone and allowing it to dry, the grid becomes slightly embedded in the plastic. The replica with the attached grid is then stripped in the usual manner and subsequently sectioned around the grid. The sample is now ready for further processing.

Occasionally the area of interest on a fracture sample is located close to a shear lip or is characterized by severe changes in surface texture. In cases of this type the plastic replica is first stripped. The areas of interest are then carefully sectioned to sizes appropriate to the ⅛-inch diameter stainless steel grids. A grid is placed on a clean glass slide and moistened with a drop of acetone. Then, the plastic replica is placed, sample side up, onto the grid just as the acetone seems to have completely evaporated. The replica is held down by the corners using tweezers for a few seconds. The result is the plastic replica is firmly adhered to the grid without damage to the sample side.

All plastic replicas were platinum shadowed at a 45° angle prior to deposition of the carbon film. A technique which has proved successful was then used to dissolve the cellulose acetate replica.

b. Appendix II

A fractured bolt sent from Rocket Propulsion Laboratory at Edwards Air Force Base by Mr. William Payne was also received at Mellon Institute for the purpose of fractographic analysis. A photograph of the fracture surface is given in Figure 112. Replication was concentrated in the area pointed out by the arrow. This area is characterized by a surface texture much flatter than the rest of the sample.

The results of the study are shown by the electron fractographs in Figures 113 through 118. A very predominant fracture pattern is apparent. It is characterized by a very high density of surface markings, giving the impression on an etching effect, on transgranular fracture facets. Hair-line networks of markings of the type seen in these fractographs are often found on hydrogen embrittlement induced fractures. They are believed to be associated with the fracture process or the alloy microstructure.

LPC Code: None Mellon Code: A

2X

Appearance of Fracture

The area of initial fracture is shown by the arrow in the photograph. This area is characterized by a flat surface texture and the presence of two discolored regions extending to the bolt edge.

Electron Fractographic Analysis

Fractographs showing the typical appearance of the fracture in the area pointed out above are given in Figures 46, 47, 48, and 49. The discolored regions at the fracture origin show an intergranular mechanism of fracture propagation somewhat obscured by large amounts of corrosion products (see arrows in Figures 46 and 47). Away from the discolored regions but still in the area of initial fracture a mixed fracture mechanism of intergranular rupture and quasi-cleavage was predominant, as shown in Figures 48 and 49. The very dark material on the fractograph in Figure 48 is a remnant of surface oxide initially contaminating the surface.

Figure 45 Photograph of the Fractured Surface of H-11 Steel Bolt Sample, Mellon Code A, and Pertinent Information

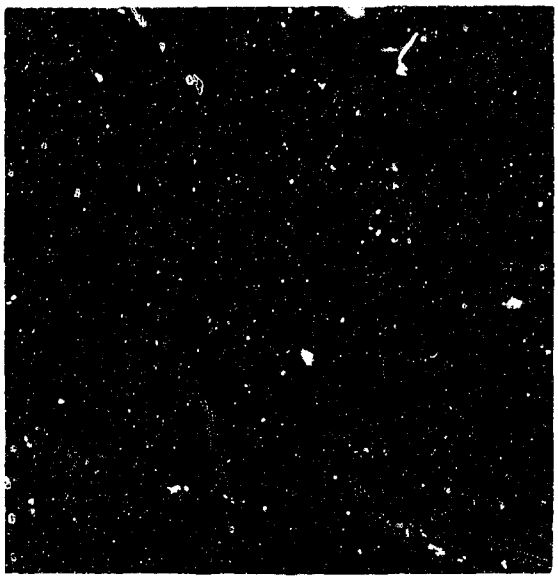

Figure 46 Fractograph Showing an Intergranular Mechanism of Fracture Propagation. Arrows Point Out Corrosion Products.

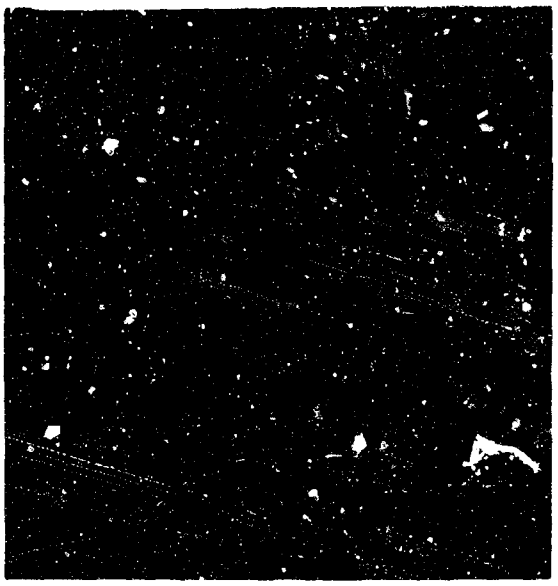

Figure 47 Fractograph Showing an Intergranular Mechanism of Fracture Propagation. Arrows Point Out Corrosion Products.

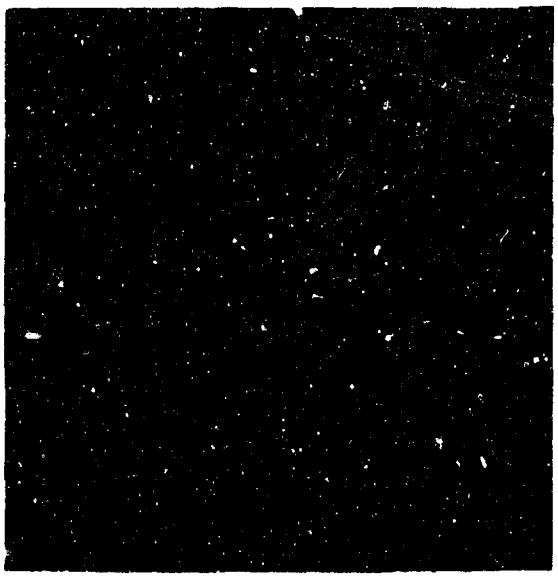

Figure 48 Fractograph Showing a Mixed Intergranular and Quasi-Cleavage Fracture Mechanism. The Dark Material on the Fractograph is a Remnant of Surface Oxide Initially Contaminating the Surface.

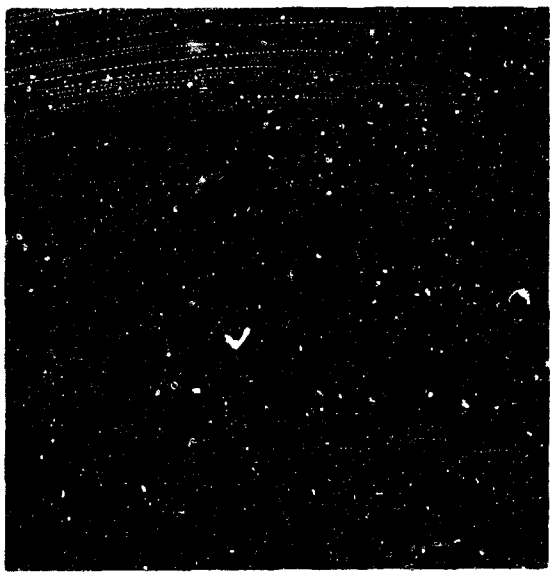

Figure 49 Fractograph Showing a Mixed Intergranular and Quasi-Cleavage Fracture Mechanism.

LIC Code: None Mellon Code: B

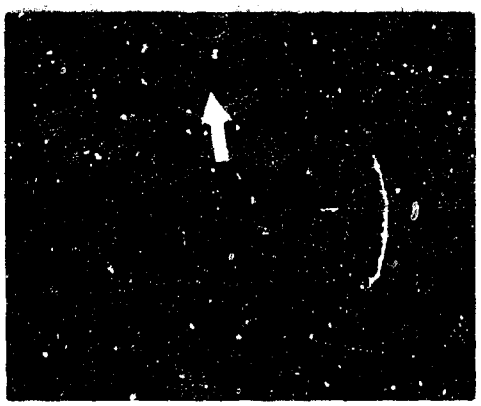

2X

Appearance of Fracture

The area of initial fracture is shown by the arrow in the photograph. This area is characterized by a flat surface texture and lack of other unusual markings. The discolored regions seen on the fracture surface are of a post-failure origin.

Electron Fractographic Analysis

The four fractographs given in Figure 51, 52, 53, and 54 are typical of the fracture appearance in the area pointed out above. The predominant mechanism of fracture propagation is quasi-cleavage with occasional intergranular and dimpled rupture facets.

Figure 50 Photograph of the Fractured Surface of H-11 Steel Bolt Sample, Mellon Code B, and Pertinent Information

4000X

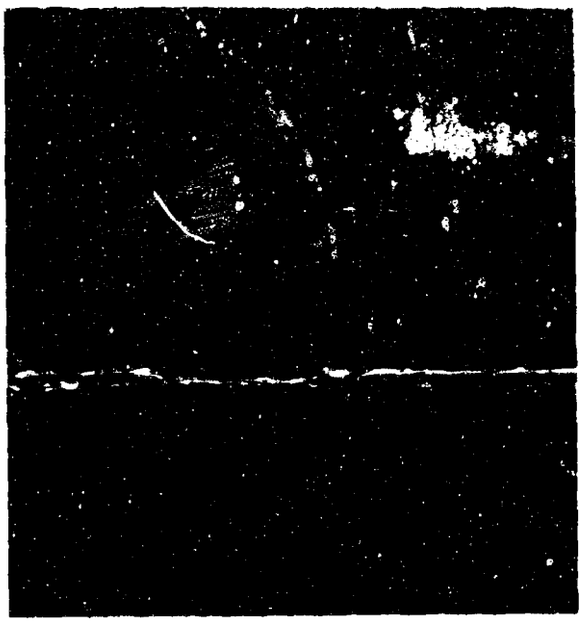

Figure 51 Fractograph Showing a Mixed Intergranular and Quasi-Cleavage Fracture Mechanism

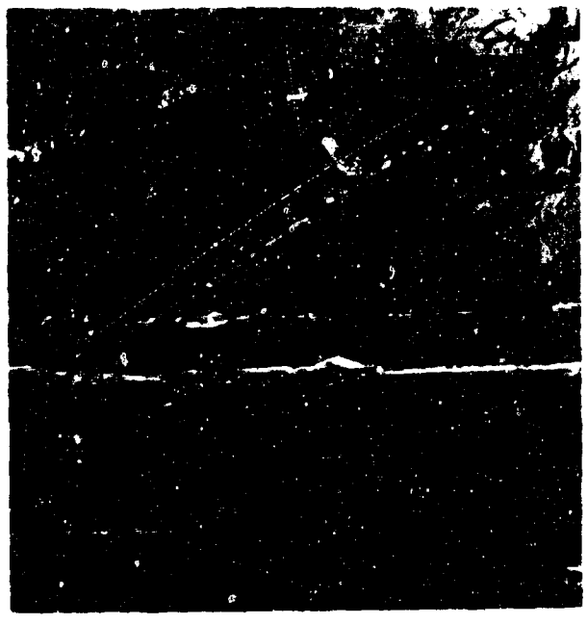

Figure 52 Fractograph Showing a Mixed Quasi-Cleavage and Dimpled Rupture Fracture Mechanism

Figure 53 Fractograph Showing Quasi-Cleavage Fracture Mechanism

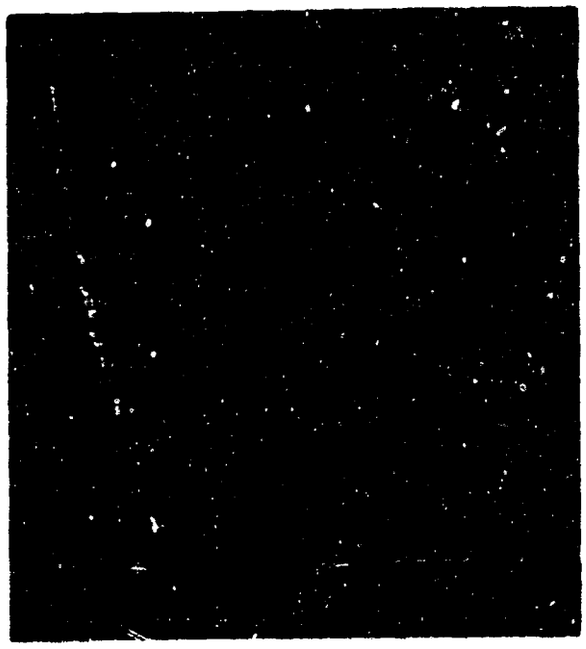

Figure 54 Fractograph Showing a Mixed Quasi-Cleavage and Dimpled Rupture Fracture Mechanism

LPC Code: None Mellon Code: C

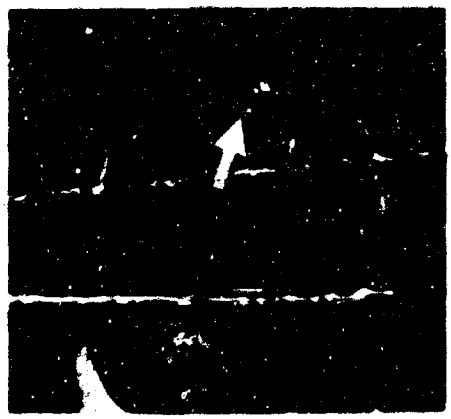

2X

Appearance of Fracture

The area of initial fracture is shown by the arrow. This area is characterized by a flat surface texture and the presence of a shiny fan-shaped region a short distance from the bolt edge.

Electron Fractographic Analysis

Two distinctly different patterns of fracture propagation were found in and around the fan-shaped area pointed out above. Figures 56, 57, 58, and 59 are illustrative of a mechanism of propagation associated with an environmental effect. Features are present on the fractographs which generally accompany stress corrosion fracturing. These will be noted in each figure. Little resistance to fracture was experienced when crossing the area represented by the fractographs in Figures 60 and 61. This condition is generally classed as material defect which, in this case, seems to be large amounts of banded and clustered, regularly shaped, secondary phase particles. It is not known whether the two mechanisms were related to this fracture.

Figure 55 Photograph of the Fractured Surface of H-11 Steel Bolt Sample, Mellon Code C, and Pertinent Information

4000X

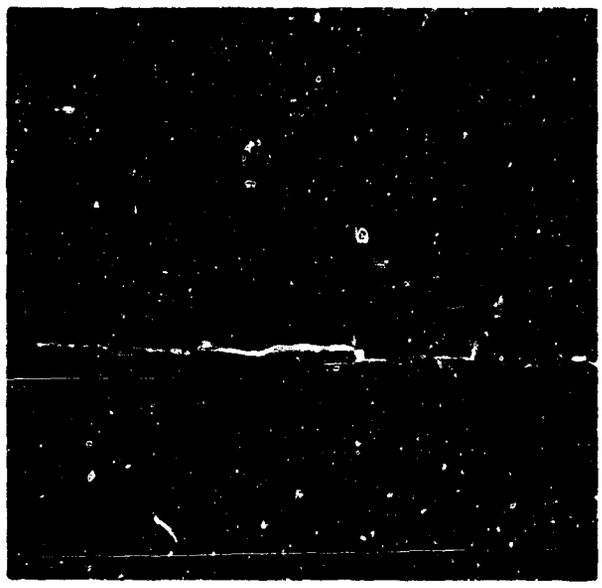

Figure 56 Fractograph Showing a "Mud-Crack" Pattern, a Phenomenon of Corrosive Attack, Commonly Found Accompanying Stress Corrosion Failures

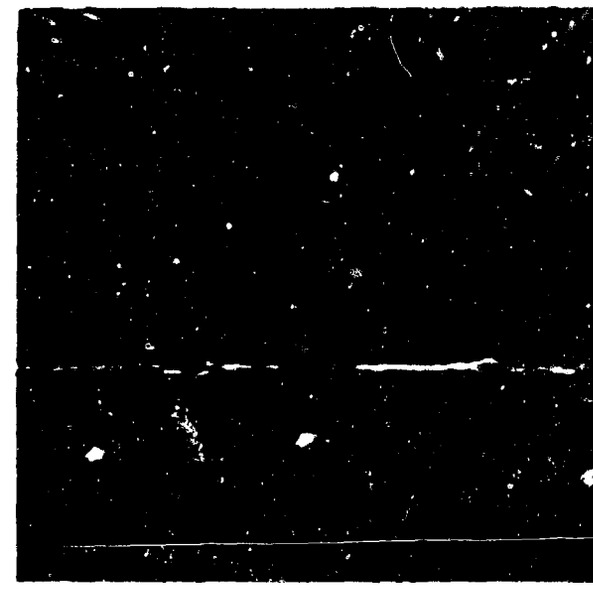

Figure 57 Fractograph Showing Large Amounts of Corrosion Products (see arrows) on What Appeared to be Intergranular Fracture Facets

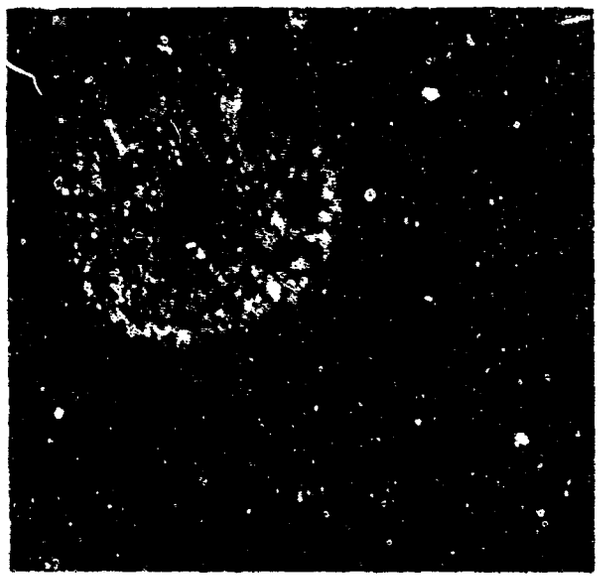

Figure 58 Fractograph Showing a Mixed Intergranular and Quasi-Cleavage Fracture M[illegible]m. Arrows Point Out C[illegible] Products on the Frac[illegible]cets

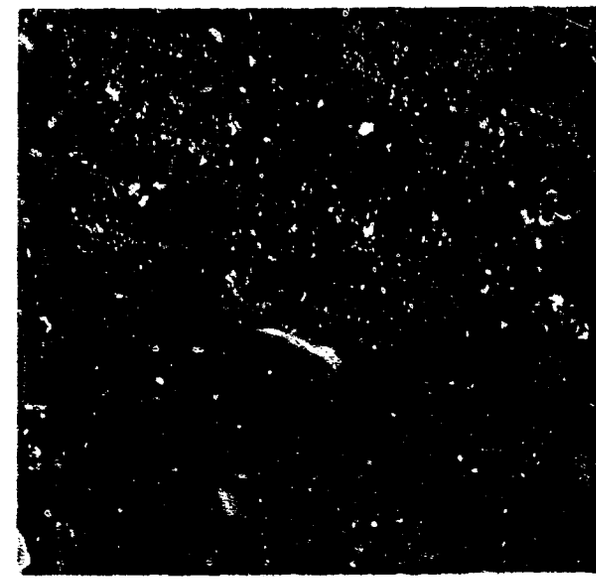

Figure 59 Fractograph Showing a Quasi-Cleavage Fracture Mechanism in the Presence of a Smooth Corrosion Product (see arrows)

4000X

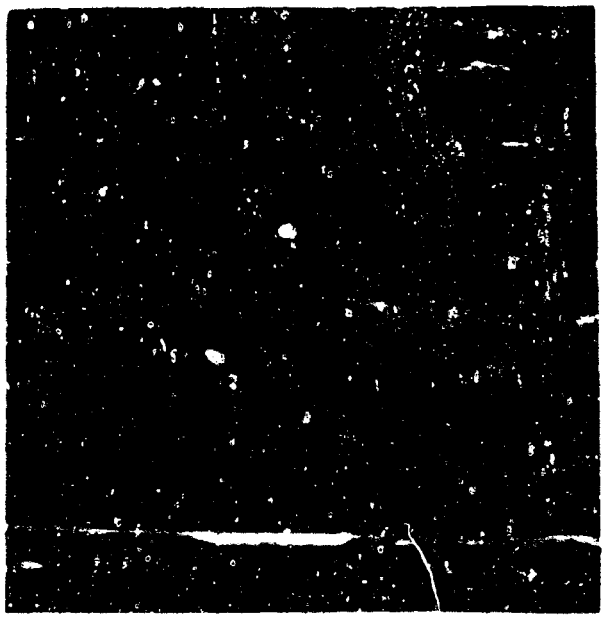

Figure 60 Fractograph Showing a Material Defect Type of Fracture Mechanism. In This Case, the Material Defect is Large Amounts of Banded and Clustered Secondary Phase Particles

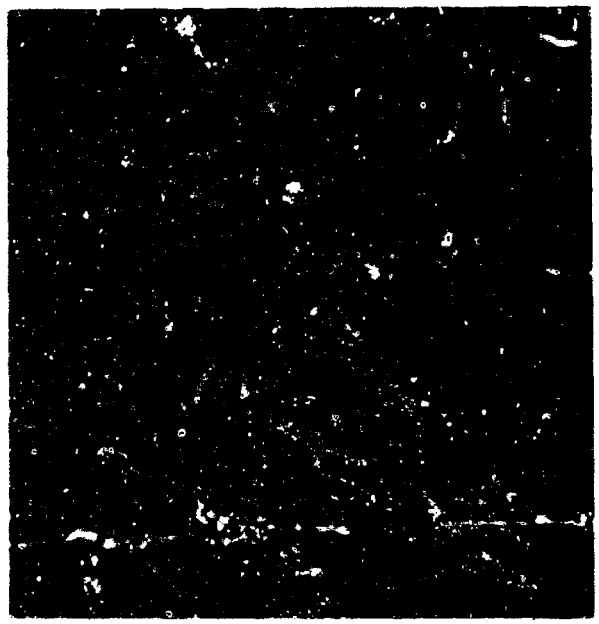

Figure 61 Fractograph Showing a Material Defect Type of Fracture Mechanism. In This Case, the Material Defect is Large Amounts of Banded and Clustered Secondary Phase Particles

LPC Code: None Mellon Code: D

2X

Appearance of Fracture

The area of initial fracture is shown by the arrow in the photograph. This area is characterized by a flat surface texture and the lack of other unusual markings.

Electron Fractographic Analysis

The fractographs given in Figures 63 through 69 are typical of the type of fracturing found in the area pointed out above. The mechanism of propagation seen in practically all of the figures can be classed as predominantly quasi-cleavage. However, there are facets on most of the fractographs which suggest some intergranular or transgranular fracturing. In addition, the numerous fine-lined markings on the fracture facets, especially as seen in Figures 63, 64, 65, and 66, suggest the possibility of an environmental effect adding to the failure condition.

Figure 62 Photograph of the Fractured Surface of H-11 Steel Bolt Sample, Mellon Code D, and Pertinent Information

4000X

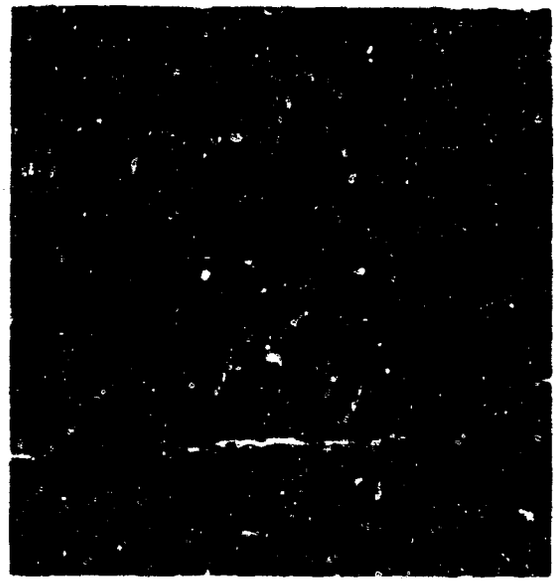

Figure 63 Fractograph Showing a Quasi-Cleavage Fracture Mechanism with Numerous Fine-Line Markings on the Fracture Facets

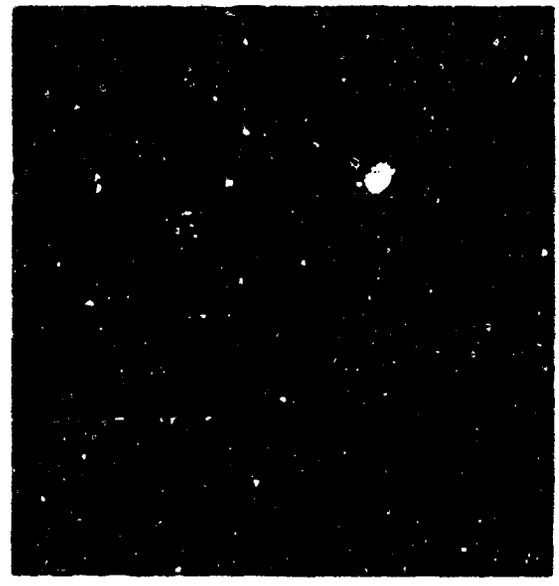

Figure 64 Fractograph Showing a Quasi-Cleavage Fracture Mechanism with Numerous Fine-Line Markings on the Fracture Facets

Figure 65 Fractograph Showing a Mixed Quasi-Cleavage and Intergranular Fracture Mechanism with Numerous Fine-Line Markings on the Fracture Facets

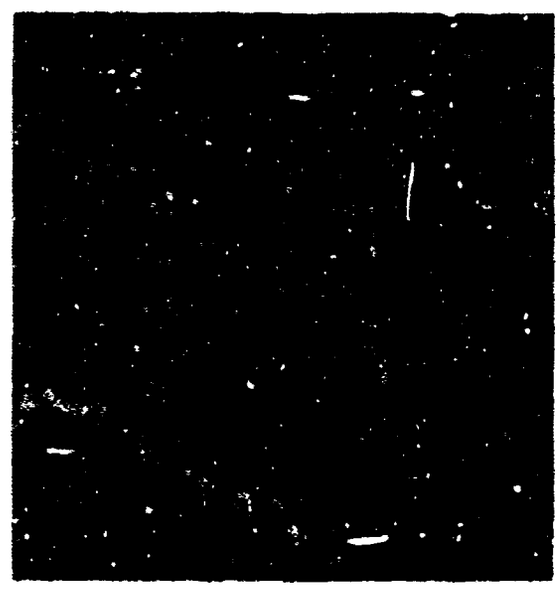

Figure 66 Fractograph Showing a Quasi-Cleavage Fracture Mechanism with Numerous Fine-Line Markings on the Fracture Facets

4000X

Figure 67 Fractograph Showing a Mixed Quasi-Cleavage and Intergranular Fracture Mechanism

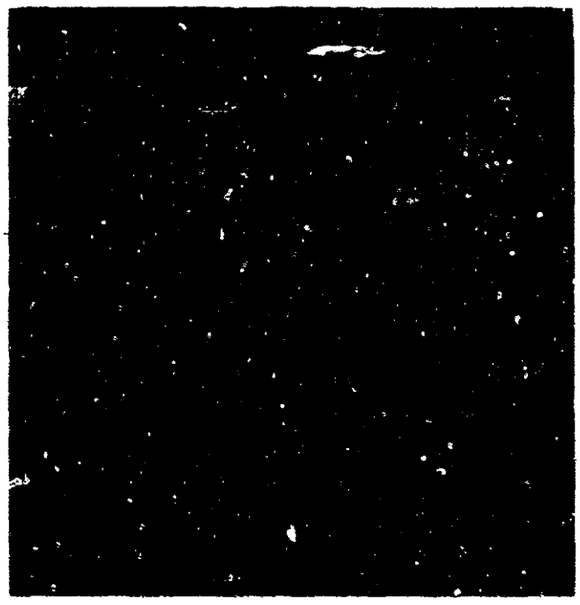

Figure 68 Fractograph Showing a Mixed Quasi-Cleavage and Dimpled Rupture Fracture Mechanism

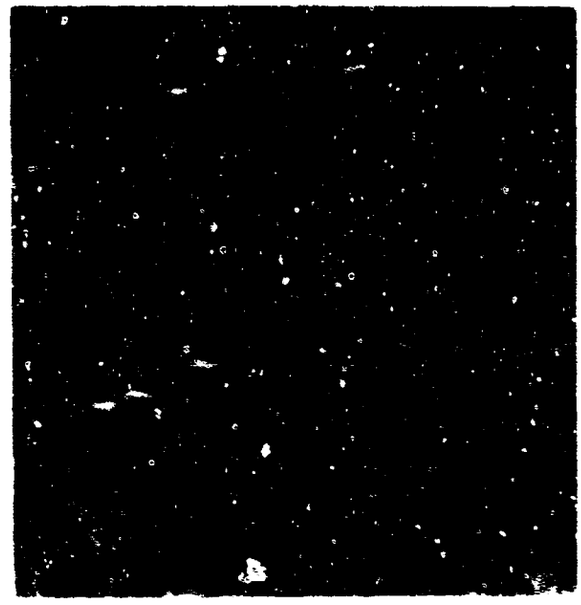

Figure 69 Fractograph Showing a Mixed Quasi-Cleavage and Dimpled Rupture Fracture Mechanism

LPC Code: 2 Mellon Code: None

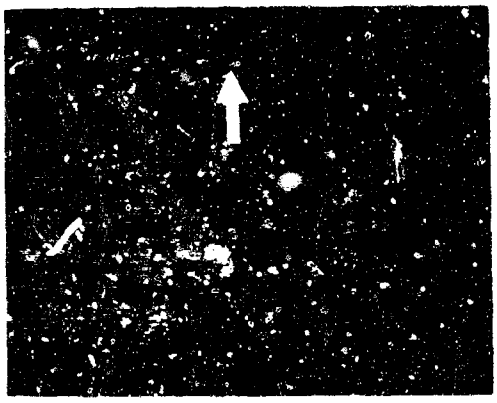

2X

Appearance of Fracture

The area of initial fracture is shown by the arrow in the photograph. This area is characterized by a flat surface texture and the presence of a shiny fan-shaped marking extending to the edge of the bolt.

Electron Fractographic Analysis

The fractographs given in Figures 71 through 74 are typical of the type of fracturing found in the area pointed out above. The patterns do not show generally recognizable features which would allow for a classification of the mechanism of fracture propagation. However, the fracture seems to have been particularly brittle in this area as is evidenced by the lack of ductile features in most of the fractographs. The dark patches in Figures 72 and 73 are remnants of surface oxide contaminants.

Figure 70 Photograph of the Fractured Surface of H-11 Steel Bolt Sample, LPC Code 2, and Pertinent Information

4000X

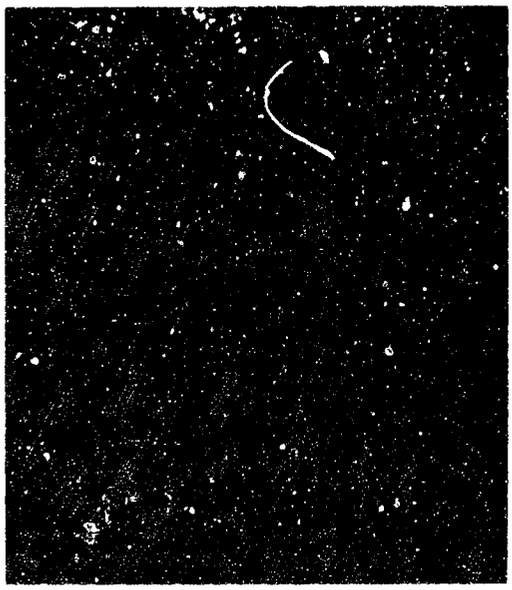

Figure 71 Fractograph Showing Complete Lack of Ductile Fracture Features

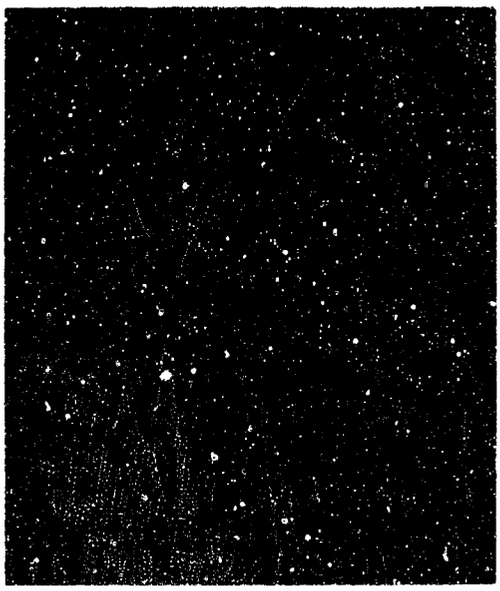

Figure 72 Fractograph Showing Complete Lack of Ductile Fracture Features

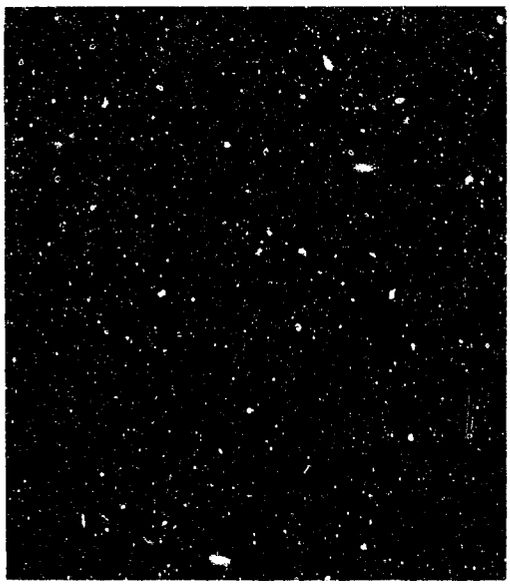

Figure 73 Fractograph Showing Signs of an Intergranular Fracture Mechanism

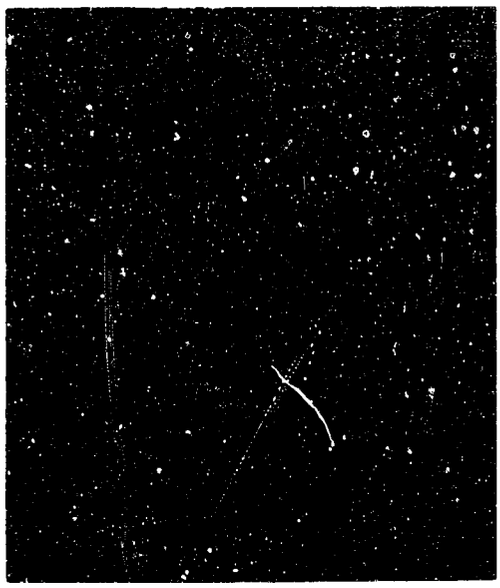

Figure 74 Fractograph Showing Mixed Quasi-Cleavage and Dimpled Rupture Fracture Mechanism

LPC Code: 28 Mellon Code: None

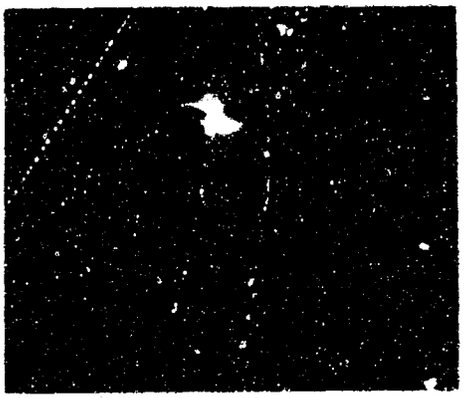

2X

Appearance of Fracture

The area of initial fracture is shown by the arrow in the photograph. This area is characterized by a flat surface texture and the lack of other unusual markings.

Electron Fractographic Analysis

Typical fracture patterns found in the area pointed out above are shown by the fractographs in Figures 76 through 79. The mechanism of propagation can be classed as predominantly quasi-cleavage with occasional indications of intergranular separation. In addition, many fine-lined markings are apparent on the fracture facets.

Figure 75 Photograph of the Fractured Surface of H-11 Steel Bolt Sample, LPC Code 28, and Pertinent Information

4000X

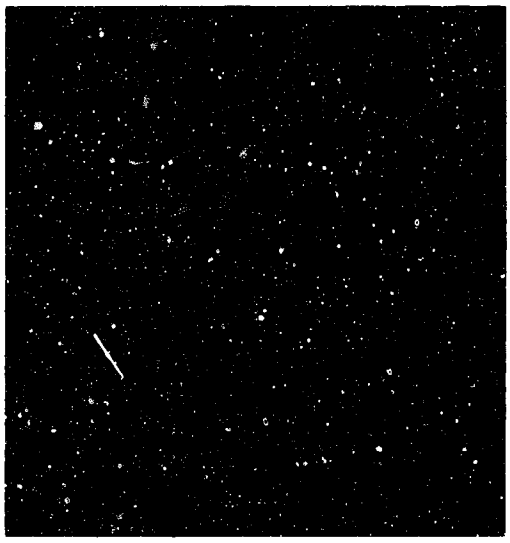

Figure 76 Fractograph Showing a Mixed Quasi-Cleavage and Intergranular Fracture Mechanism with Fine-Line Markings on the Fracture Facets

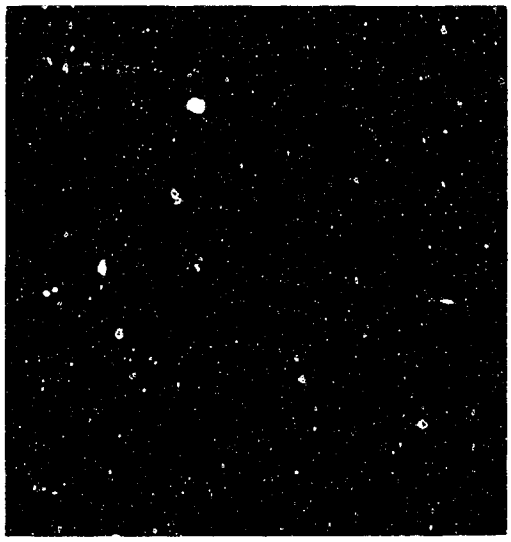

Figure 77 Fractograph Showing Quasi-Cleavage Fracture Mechanism with Fine-Line Markings on the Fracture Facets

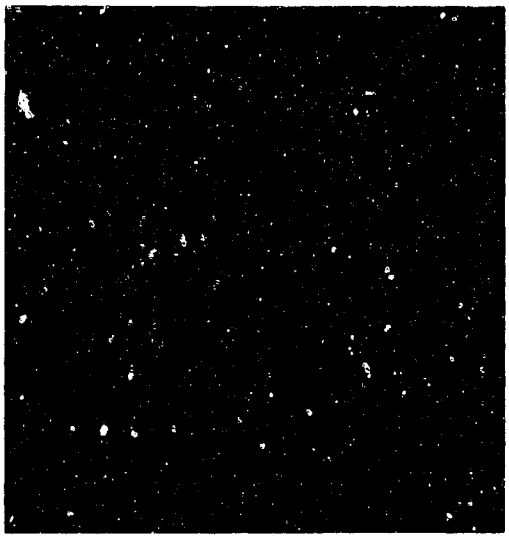

Figure 78 Fractograph Showing a Quasi-Cleavage and Intergranular Fracture Mechanism

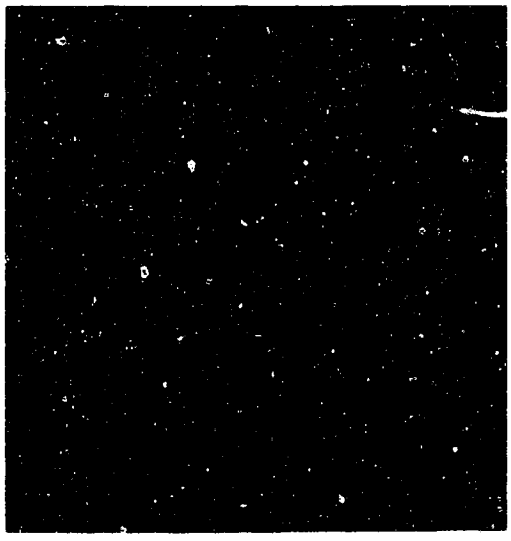

Figure 79 Fractograph Showing Quasi-Cleavage Fracture Mechanism

LPC Code: 86 Mellon Code: None

Appearance of Fracture

The area of initial fracture is shown by the arrow in the photograph. This area is characterized by a flat surface texture and the presence of a discolored region extending to the edge of the bolt.

Electron Fractographic Analysis

Typical fracture patterns found in the area pointed out above are shown in Figures 81 through 84. A transition of fracture mechanisms from very close to the edge of the bolt to just beyond the discolored region was noted. Figure 81 is a fractograph of the area very close to the edge. The features, although not recognizable, do not indicate ductile fracture. Figure 82 shows a combination quasi-cleavage, dimpled rupture in an area further away from the edge. Directional dimples, typified by the fractographs given in Figures 83 and 84, were found around the inside edge of the discolored region. The pitting or etching effect on the fracture facets of these last two figures suggest an environmental effect adding to the failure condition.

Figure 80 Photograph of the Fractured Surface of H-11 Steel Bolt Sample, LPC Code 86, and Pertinent Information

4000X

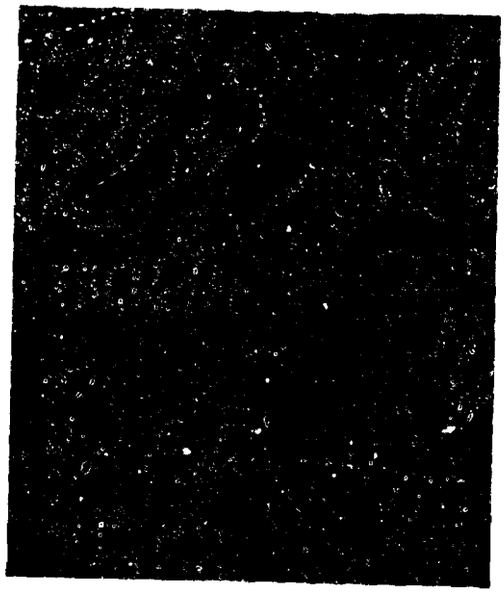

Figure 81 Fractograph Showing Complete Lack of Ductile Fracture Features.

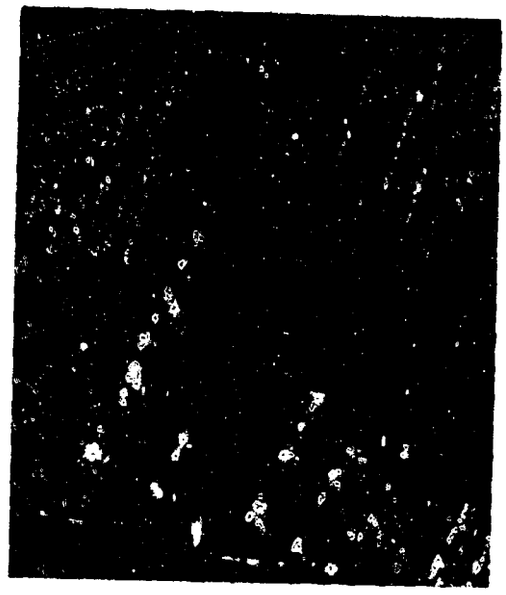

Figure 82 Fractograph Showing a Mixed Quasi-Cleavage and Dimpled Rupture Fracture Mechanism

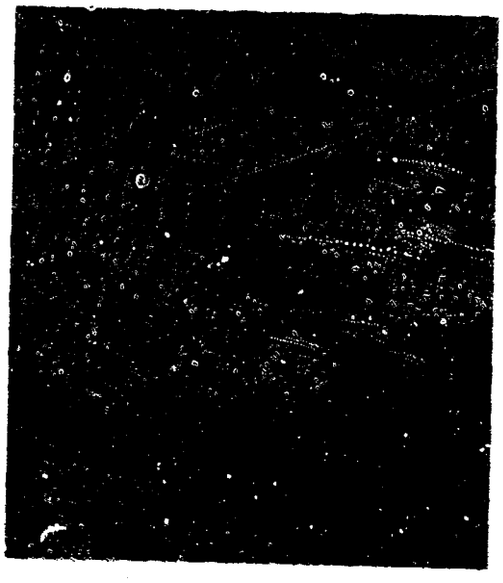

Figure 83 Fractograph Showing a Directional Dimpled Rupture Mechanism of Fracture Propagation With an Etching Effect on the Fracture Facets.

Figure 84 Fractograph Showing a Directional Dimpled Rupture Mechanism of Fracture Propagation With an Etching Effect on the Fracture Facets.

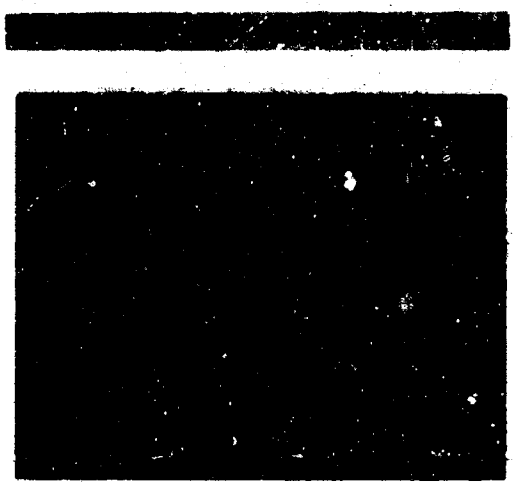

2X

Appearance of Fracture

The area of initial fracture is shown by the arrow in the photograph. This area is characterized by a flat surface texture which is discolored. The discoloration extends to the edge of the bolt.

Electron Fractographic Analysis

Typical fracture patterns found in the area pointed out above are given by the fractographs in Figures 86 through 91. Common to all of these fractographs are features which indicate the presence of a corrosion product. Figures 86 and 87 show corrosion products, indicated by arrows, on intergranular fracture facets. The mechanism of fracture propagation shown in Figure 88 can be classed as predominantly quasi-cleavage. The corrosion products and other features, due to environmental effects, completely obscure the fracture patterns in the fractographs of Figures 89, 90, and 91.

Figure 85 Photograph of the Fractured Surface of H-11 Steel Bolt Sample, LPC Code 95, and Pertinent Information

4000X

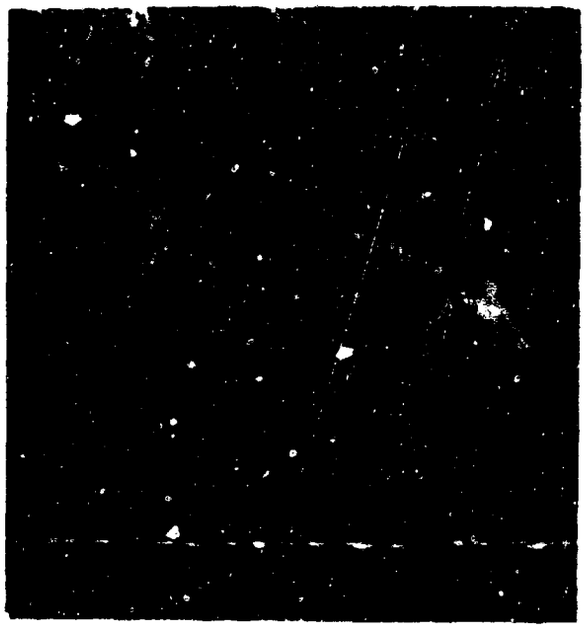

Figure 86 Fractograph Showing An Intergranular Fracture Mechanism With Corrosion Products (see arrows) Present in Fracture Facets.

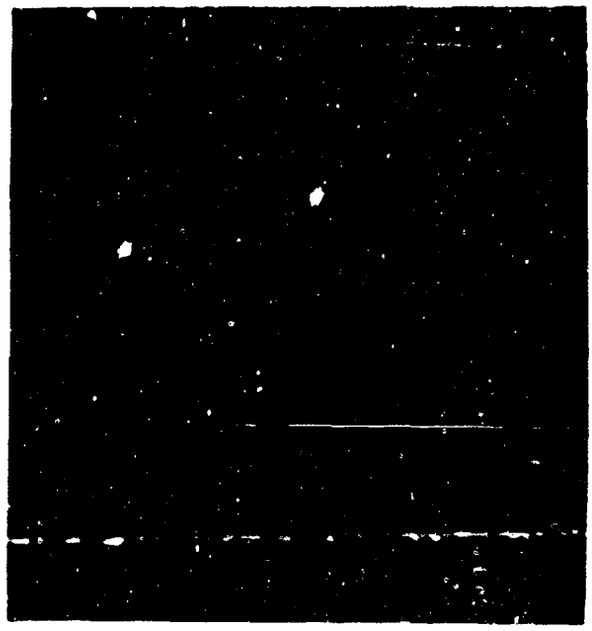

Figure 87 Fractograph Showing An Intergranular Fracture Mechanism With Corrosion Products (see arrows) Present in Fracture Facets.

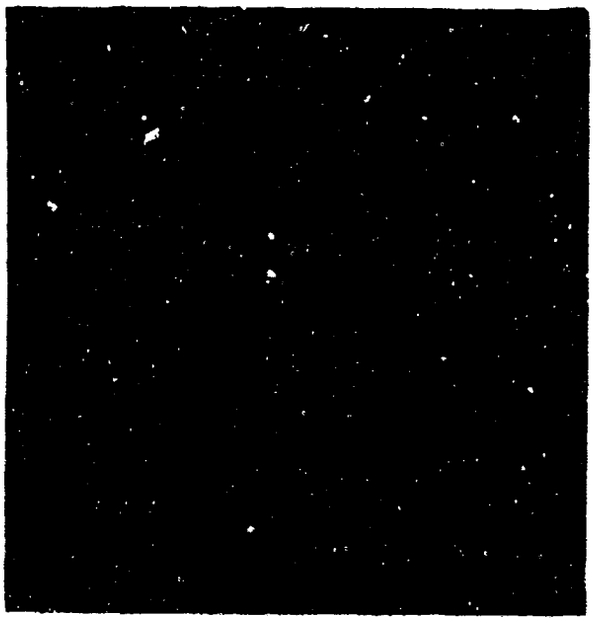

Figure 88 Fractograph Showing Quasi-Cleavage Fracture Mechanism With Corrosion Products Present on all Fracture Facets.

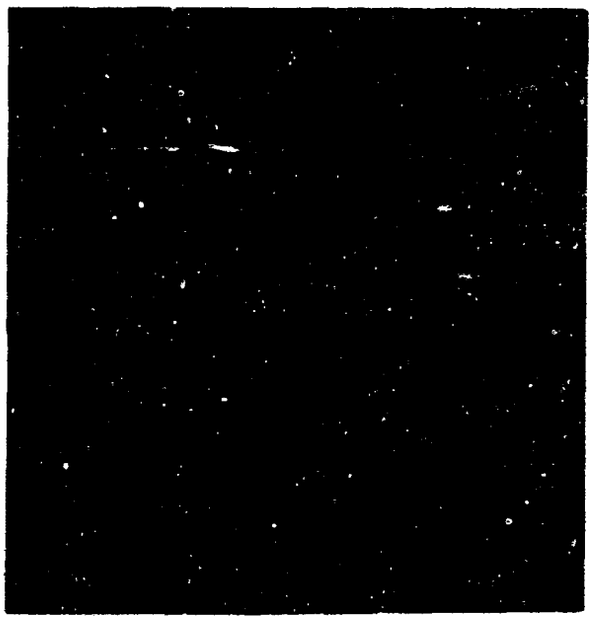

Figure 89 Fractograph Showing "Mud-Crack" Patterns and Corrosion Products Obscuring the Fracture Pattern.

4000X

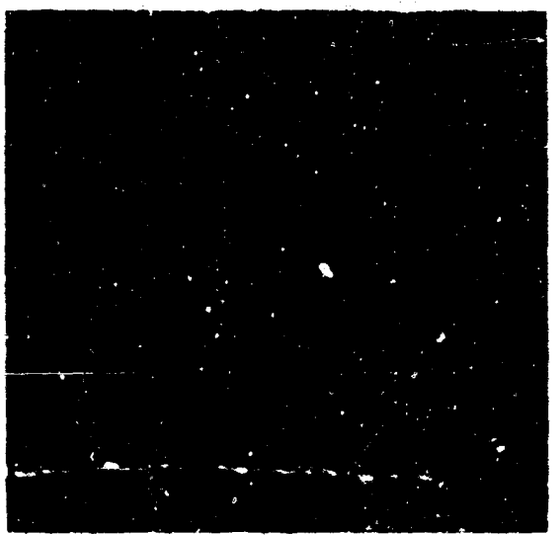

Figure 90 Fractograph Showing a "Mud-Crack" Corrosion Pattern Completely Obscuring the Fracture Pattern.

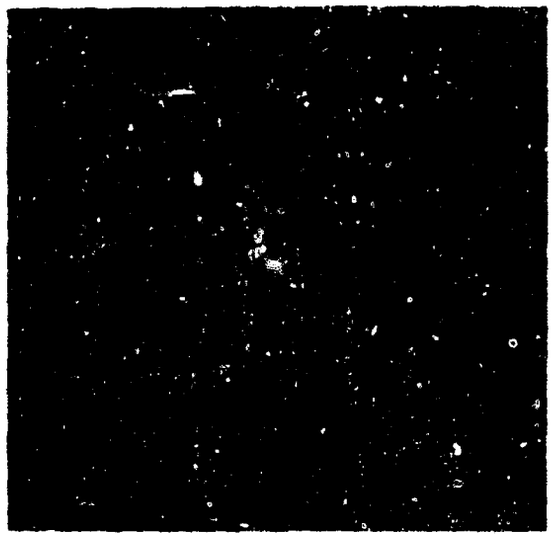

Figure 91 Fractograph Showing a Needle-Like Corrosion Product Completely Obscuring the Fracture Pattern.

LPC Code: 99 Mellon Code: None

2X

Appearance of Fracture

The area of initial fracture is shown by the arrow in the photograph. The area is characterized by a small region close to the edge having a flat surface texture and the lack of other unusual markings.

Electron Fractographic Analysis

The fractograph given in Figure 93 is typical of the fracture pattern in the area close to the edge pointed out above. The mechanism of fracture propagation is classed as quasi-cleavage. Also apparent is the high density of fine-line markings on the fracture facets.

Figure 92 Photograph of the Fractured Surface of H-11 Steel Bolt Sample, LPC Code 99, and Pertinent Information.

4000X

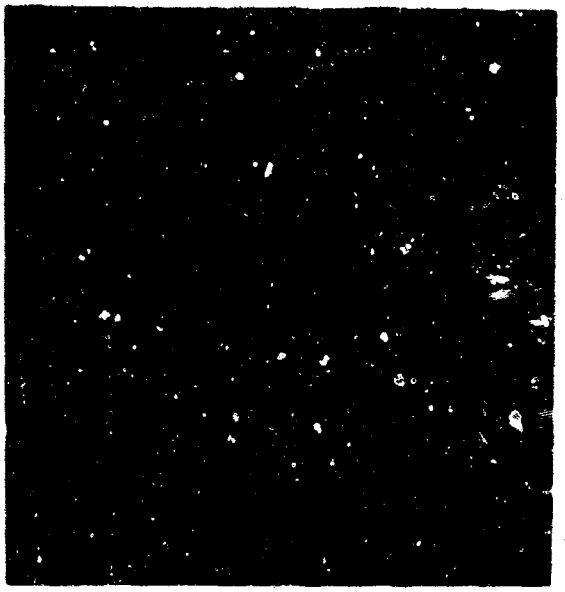

Figure 93 Fractograph Showing a Quasi-Cleavage Fracture Mechanism With Many Fine-Line Markings on the Fracture Facets

LPC Code: 106 Mellon Code: None

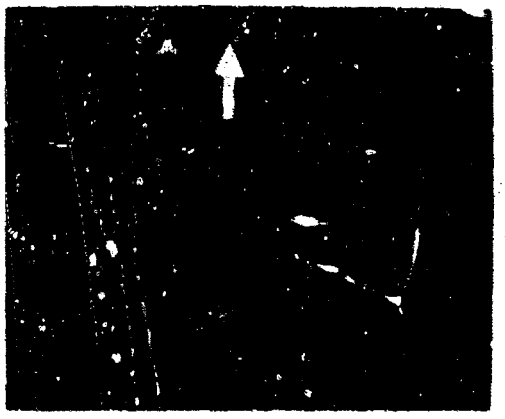

2X

Appearance of Fracture

The area of initial fracture is shown by the arrow in the photograph. This area is characterized by a flat surface texture and a discolored region which extends to the bolt edge.

Electron Fractographic Analysis

The fracture pattern typical of the area in and around the discolored region pointed out above are shown by the fractographs in Figures 95, 96, and 97. The mechanism of fracture propagation is predominantly quasi-cleavage with occasional evidence of dimpled rupture, the latter indicated in Figure 97. The presence of a smooth corrosion product is also noted by arrows in the figures.

Figure 94 Photograph of the Fractured Surface of H-11 Steel Bolt Sample, LPC Code 106, and Pertinent Information.

4000X

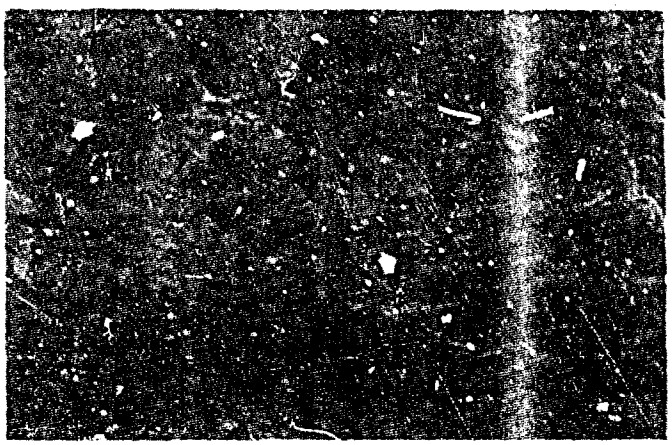

Figure 95 Fractograph Showing Quasi-Cleavage Fracture Mechanism With the Presence of a Smooth Corrosion Product (see arrows).

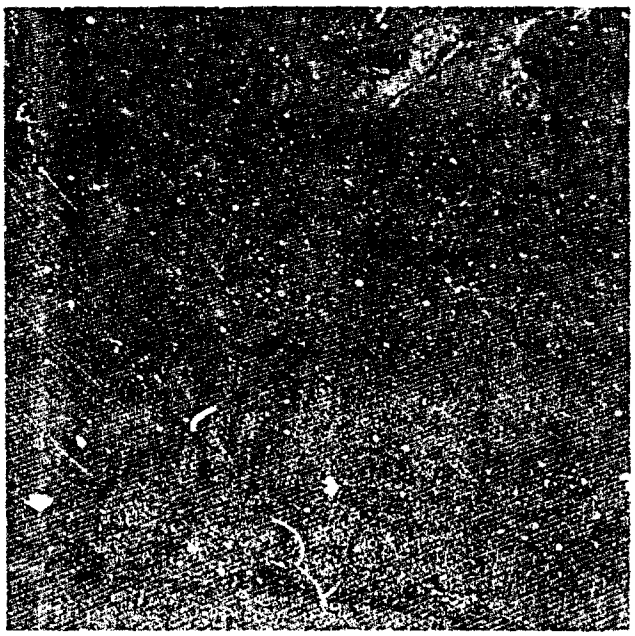

Figure 96 Fractograph Showing Quasi-Cleavage Fracture Mechanism with the Presence of a Smooth Corrosion Product (see arrows).

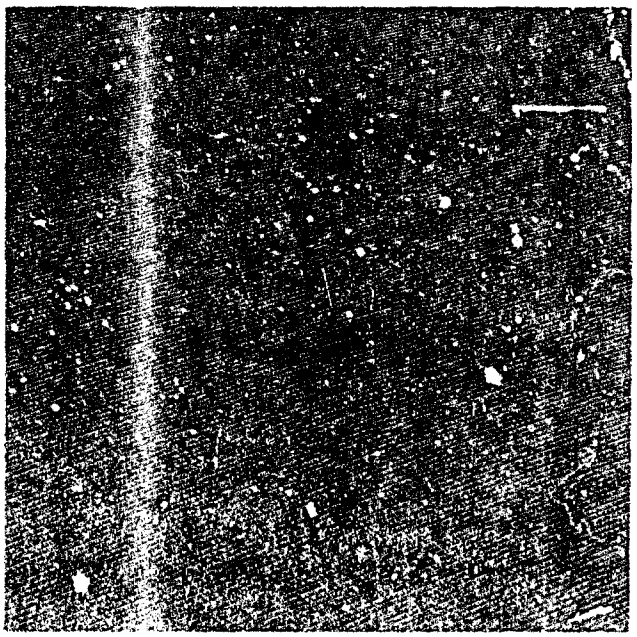

Figure 97 Fractograph Showing a Mixed Quasi-Cleavage and Dimpled Rupture Fracture Mechanism with the Presence of a Smooth Corrosion Product (see arrows).

LPC Code: 146 Mellon Code: None

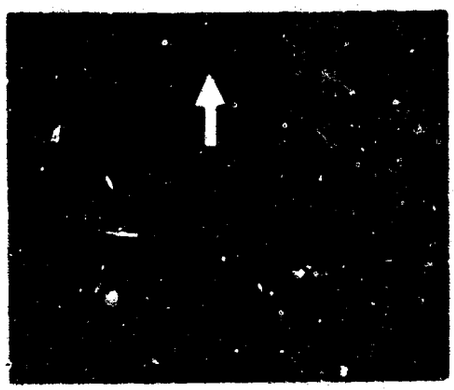

2X

Appearance of Fracture

The area of initial fracture is shown by the arrow in the photograph. This area is characterized by a flat surface texture and the lack of other unusual markings.

Electron Fractographic Analysis

Typical fracture patterns found in the area pointed out above are shown by the fractographs in Figures 99, 100, and 101. The fracture mechanism is predominantly quasi-cleavage.

Figure 98 Photograph of the Fractured Surface of H-11 Steel Bolt Sample, LPC Code 146, and Pertinent Information

4000X

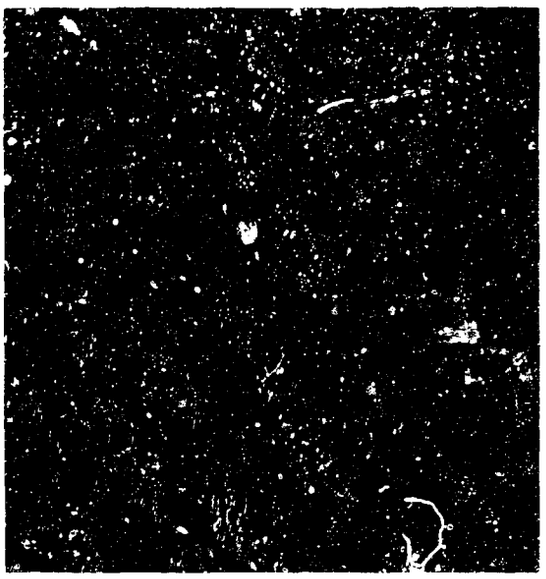

Figure 99 Fractograph Showing Quasi-Cleavage Fracture Mechanism.

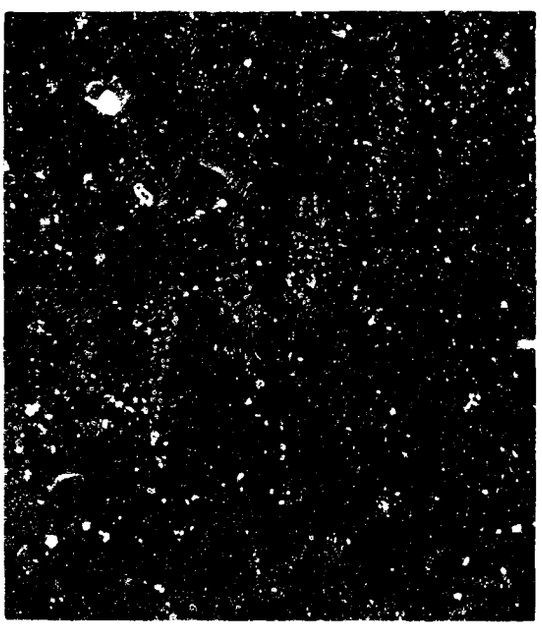

Figure 100 Fractograph Showing Quasi-Cleavage Fracture Mechanism

Figure 101 Fractograph Showing Quasi-Cleavage Fracture Mechanism

Adapter Forging Section

.5X

Appearance of Fracture

The suspected area of initial fracture is shown by the arrow in the photograph. The fracture texture is not much smoother in this region, however, the chevron pattern seems to converge here. The center band seen on the fracture is the area where the surface rust was removed.

Electron Fractograph Analysis

The fracture patterns found in and around the area of fracture origin pointed out above are shown by the fractographs in Figures 103 through 107. The predominant mechanism of fracture propagation seems to be micro-void coalescence characterized by the directional dimpled rupture seen in Figures 103, 104, and 105. The fractographs in Figures 106 and 107 show brittle fracture facets in areas where secondary phase material is present. These clusters of material, shown by arrows in the figures, are apparently brittle and fail probably by a cleavage mechanism. The result is that the fracture in the area immediately surrounding the secondary phase material propagates in a brittle manner. There is evidence of corrosion products on the fracture facets in Figures 106 and 107. It is felt that this condition is of a post-failure origin since the fracture was heavily rusted as received.

Figure 102 Photograph of the Fracture Surface of the Section From the Adapter Forging and Pertinent Information.

4000X

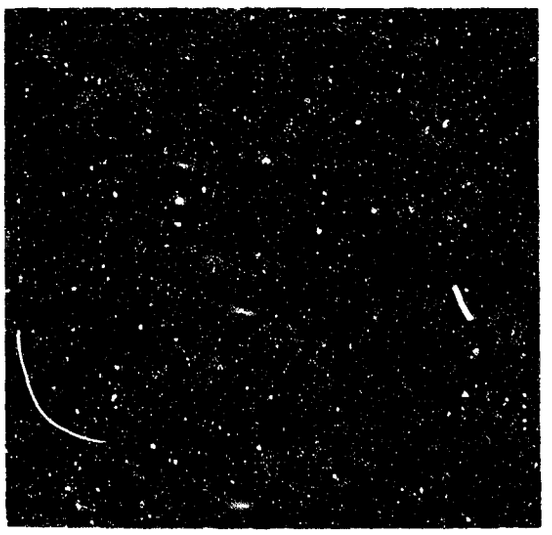

Figure 103 Fractograph Showing a Micro-Void Coalescence Mechanism of Fracture Propagation Characterized by Directional Dimples.

4000X

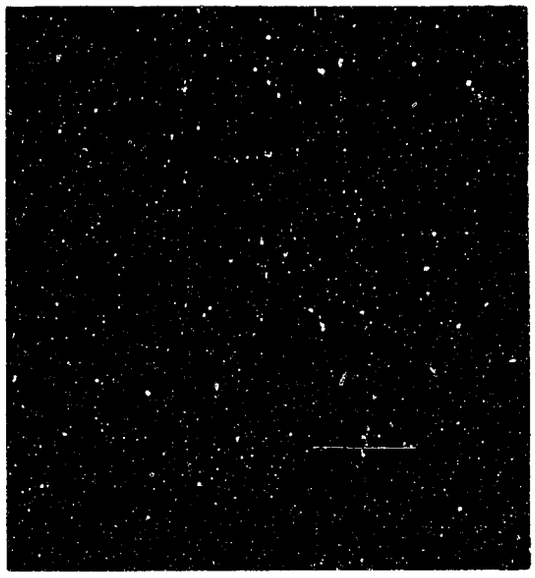

Figure 104 Fractograph Showing a Micro-Void Coalescence Mechanism of Fracture Propagation Characterized by Directional Dimples.

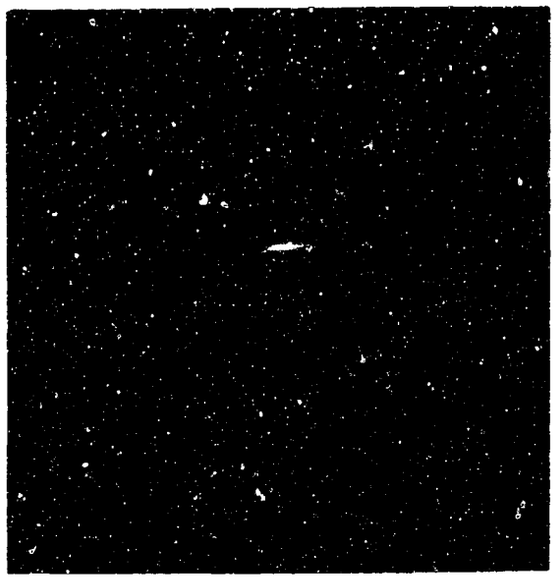

Figure 105 Fractograph Showing a Micro-Void Coalescence Mechanism of Fracture Propagation Characterized by Directional Dimples.

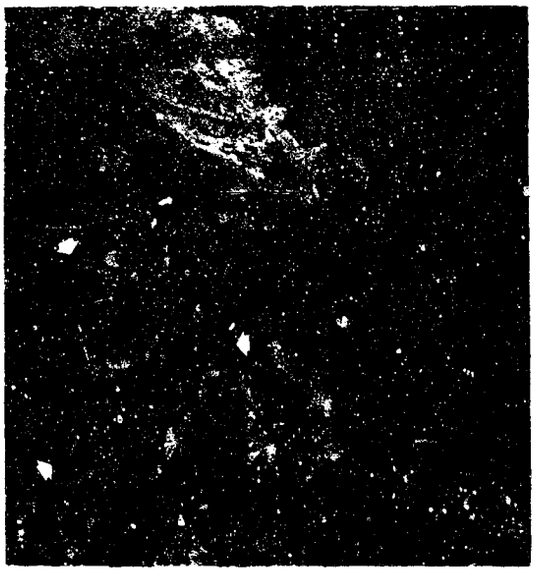

Figure 106 Fractograph Showing a Brittle Fracture Mechanism in an Area Where Secondary Phase Material is Present (see arrows). A Needle-Like Corrosion Product is Shown by the Open Arrows.

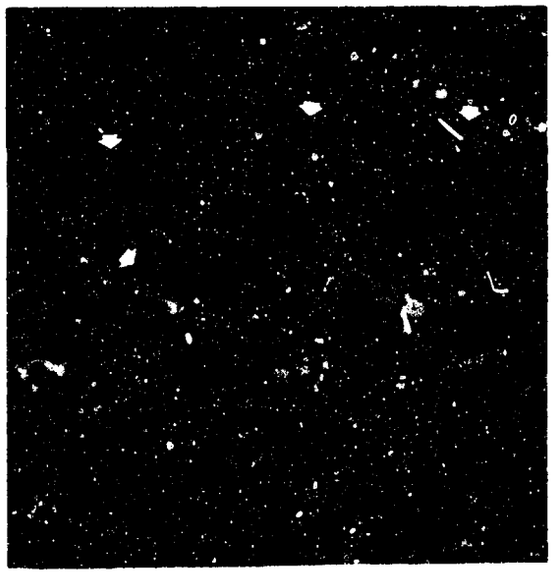

Figure 107 Fractograph Showing a Brittle Fracture Mechanism in an Area Where Secondary Phase Material is Present (see arrows).

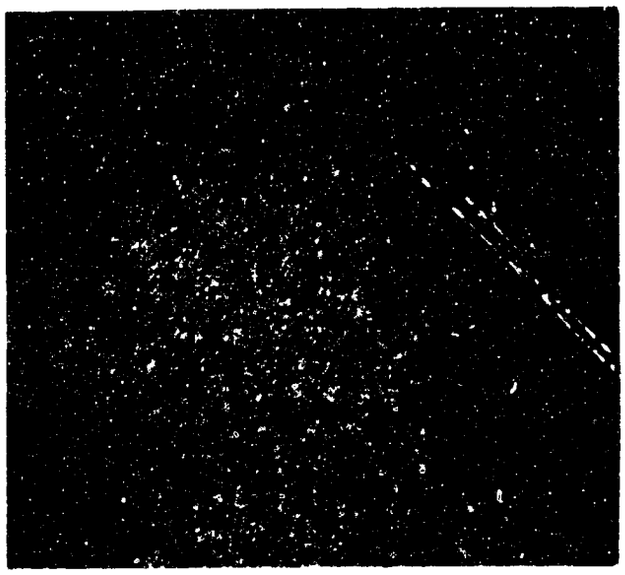

100X Etch: Mixed Acid

(a)

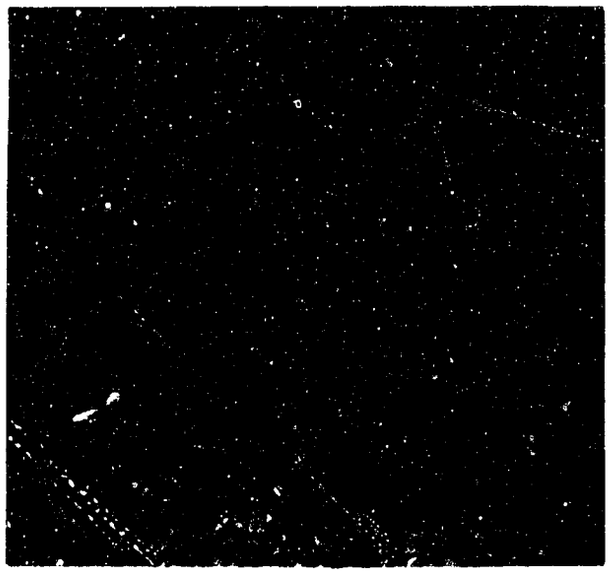

250X Etch: Mixed Acid

(b)

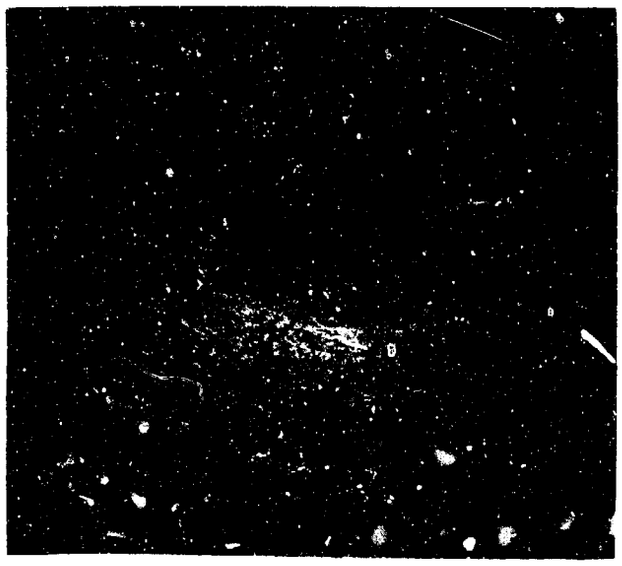

100X Etch: Mixed Acid

(c)

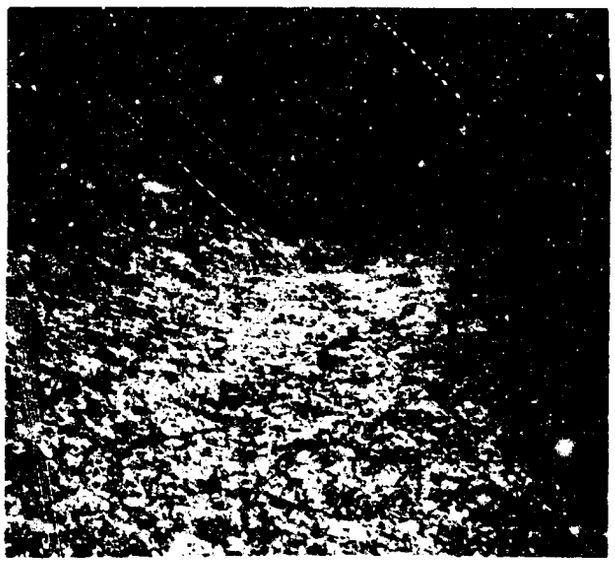

250X Etch: Mixed Acid

(d)

Figure 108- Photomicrographs Showing the Profile of the Fracture Origin, (a) and (b), of Bolt Sample 86. A Deformation Band Present at the Root of a Thread and the Occasional Cracking Found in the Bands are Shown in (c) and (d) Respectively.

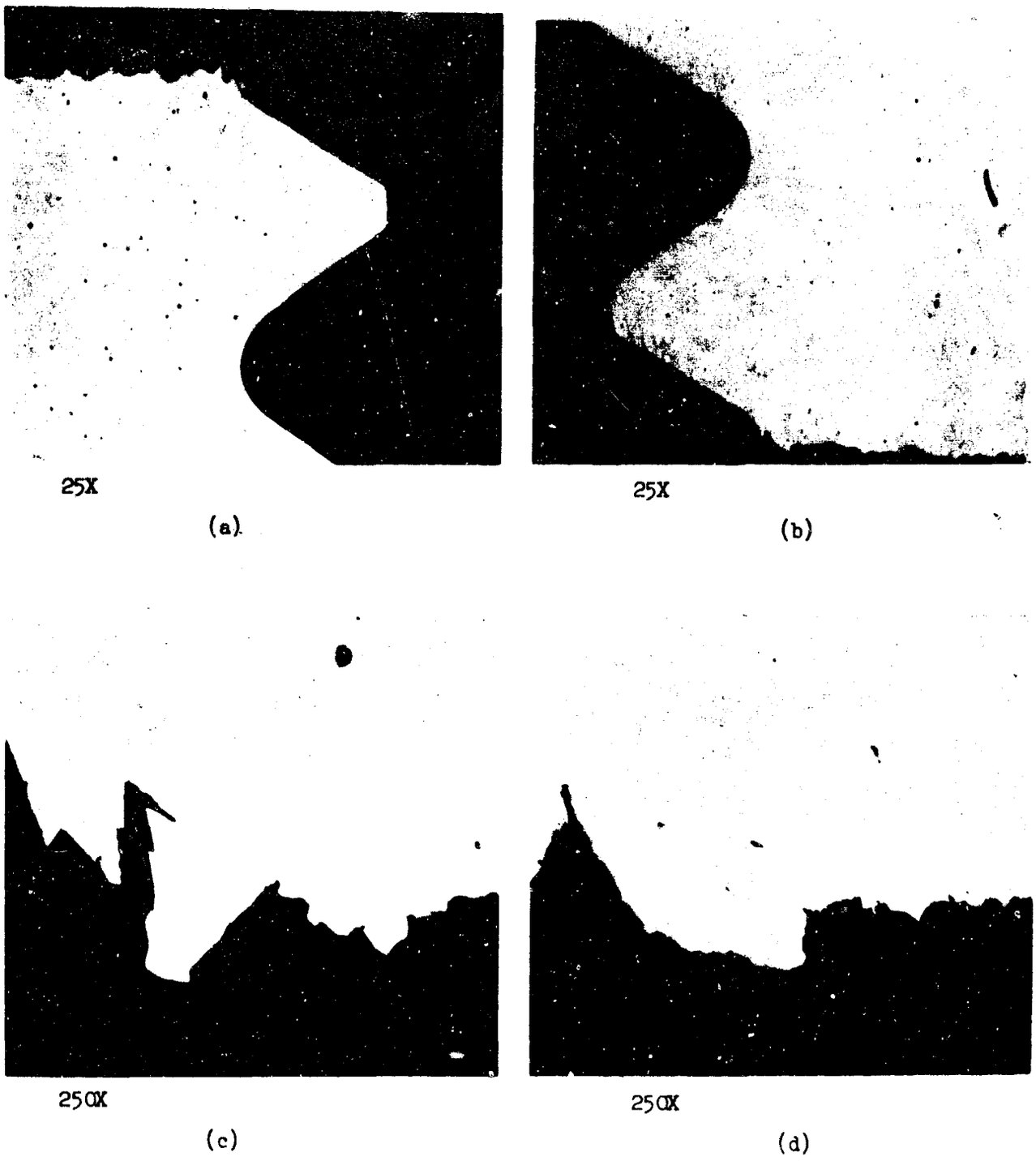

Figure 109. Photomicrographs Showing the Location, (a) and (b), and the Profile, (c) and (d), of the Fracture Origin in Bolt Sample 2.

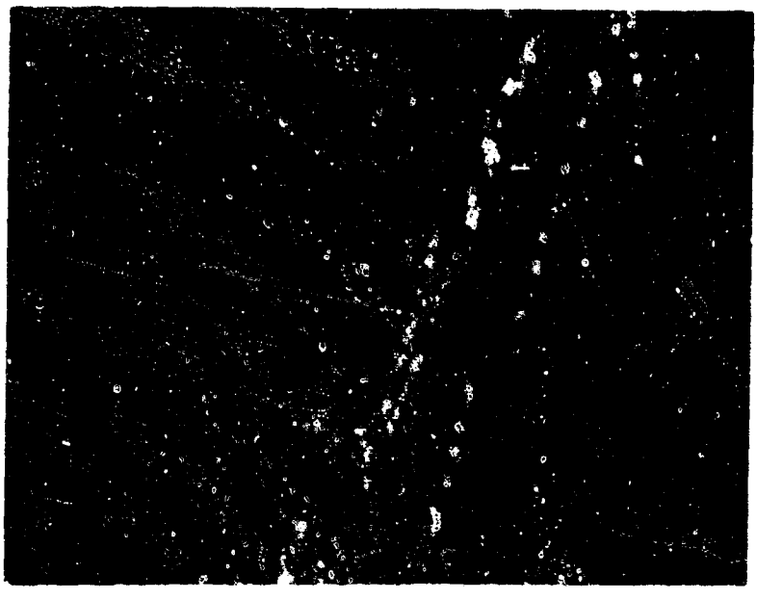

100X Etch: Mixed Acid

(a)

500X Etch: Mixed Acid

(b)

Figure 110 Photomicrographs, (a), Showing the Location of the Fracture Origin with Respect to the Thread Deformation Band in Bolt Sample 2 and (b) Cracking in the Deformation Band Associated with the First Thread Below the Fracture.

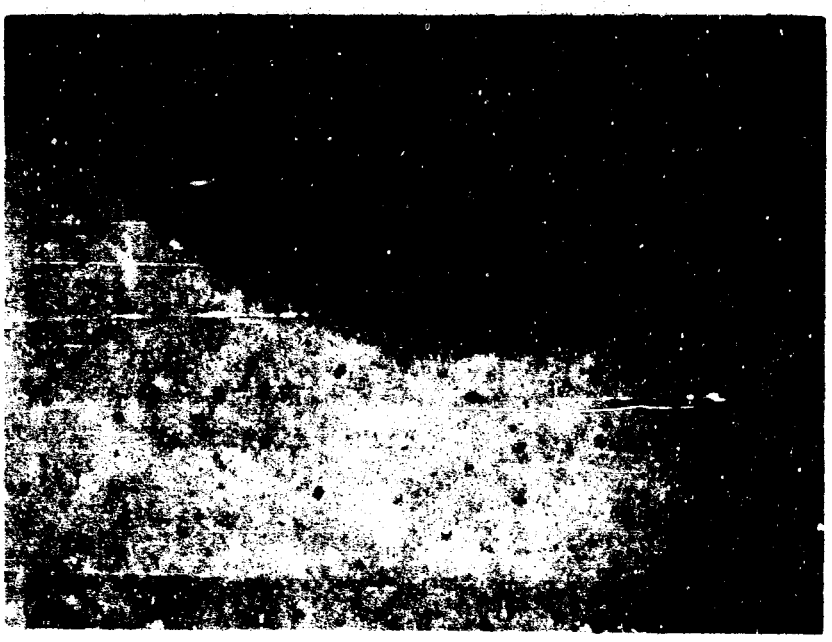

500X

Figure 111 - Fractograph Showing a Fine Network of Cracks Penetrating into the Cadmium Plate at the Root of the Thread Immediately Below the Fracture in Bolt Sample 95.

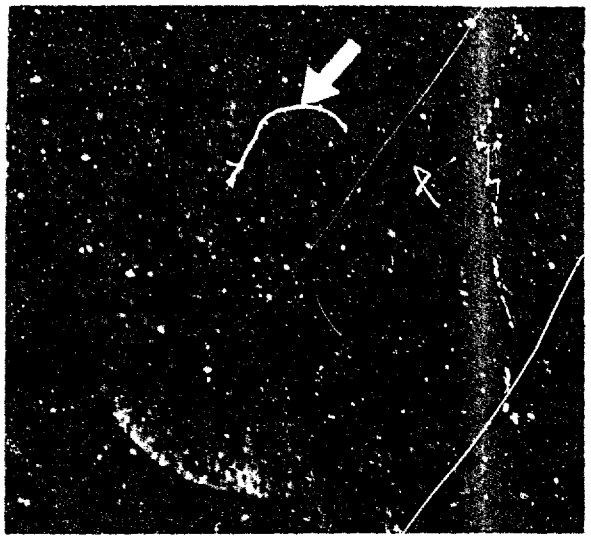

Figure 112 Photograph of the Fractured Surface of the Bolt Sample Sent From Rocket Propulsion Laboratory. The Arrow Shows the Area of Initial Fracture Where Replication was Conducted.

4000X

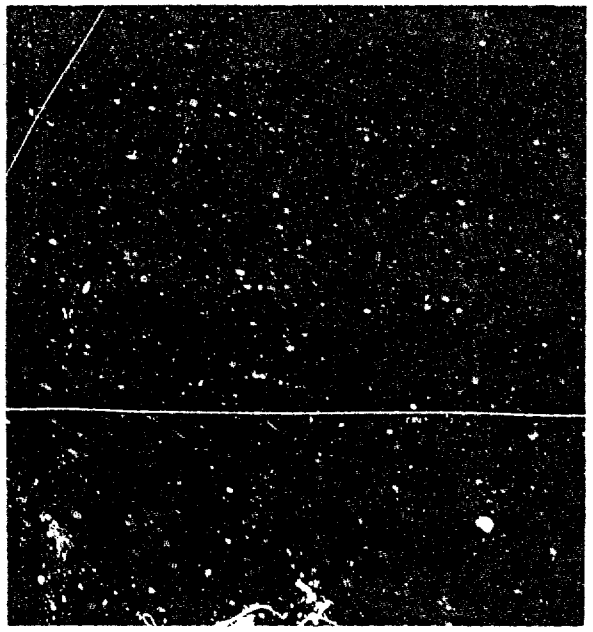

Figure 113 Fractograph Showing a Transgranular Fracture Mechanism with Many Fine-Line Marking on the Fracture Facets.

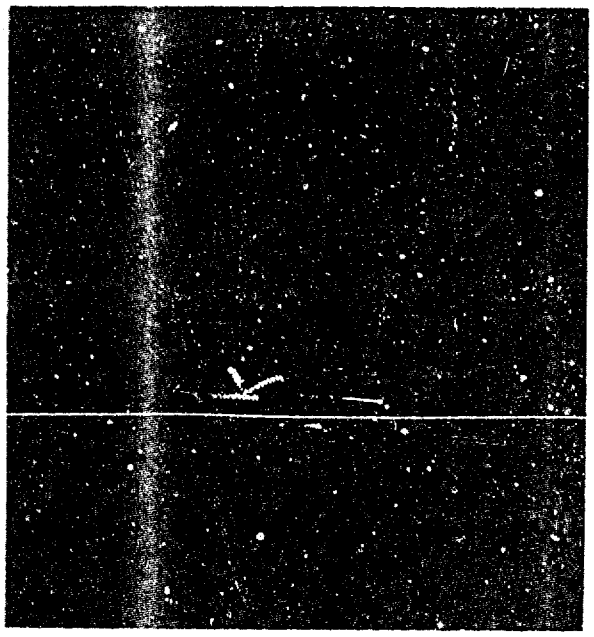

Figure 114 Fractograph Showing a Transgranular Fracture Mechanism with Many Fine-Line Markings on the Fracture Facets.

4000X

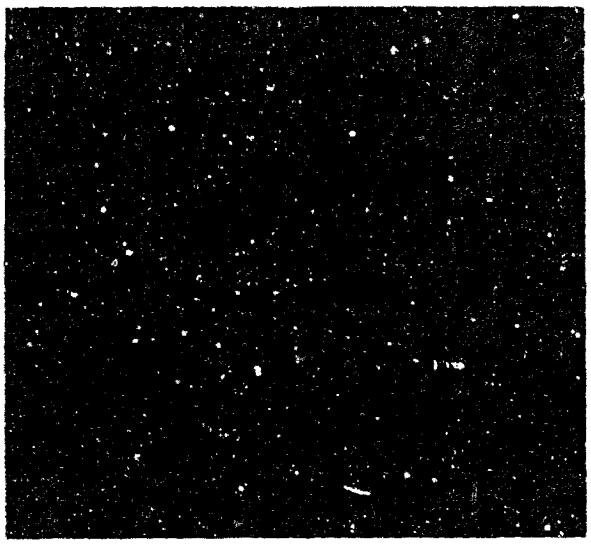

Figure 115 Fractograph Showing a Transgranular Fracture Mechanism with Many Fine-Line Markings on the Fracture Facets.

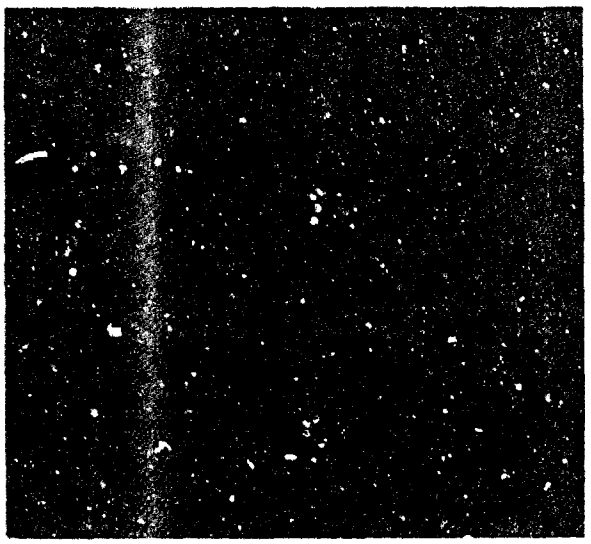

Figure 116 Fractograph Showing a Transgranular Fracture Mechanism with Many Fine-Line Markings on the Fracture Facets.

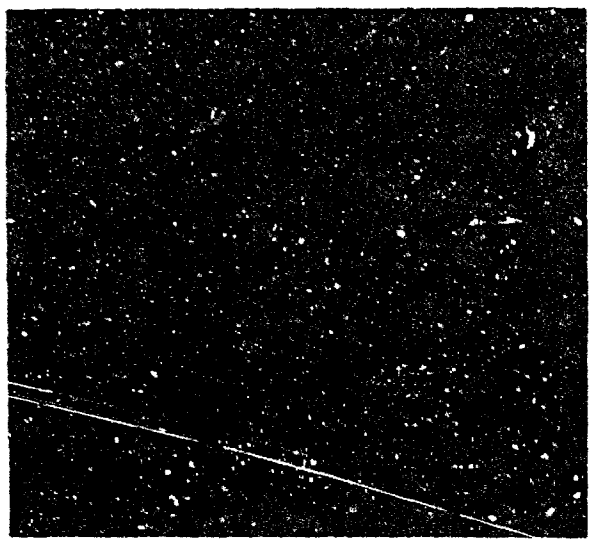

Figure 117 Fractograph Showing a Transgranular Fracture Mechanism with Many Fine-Line Markings on the Fracture Facets.

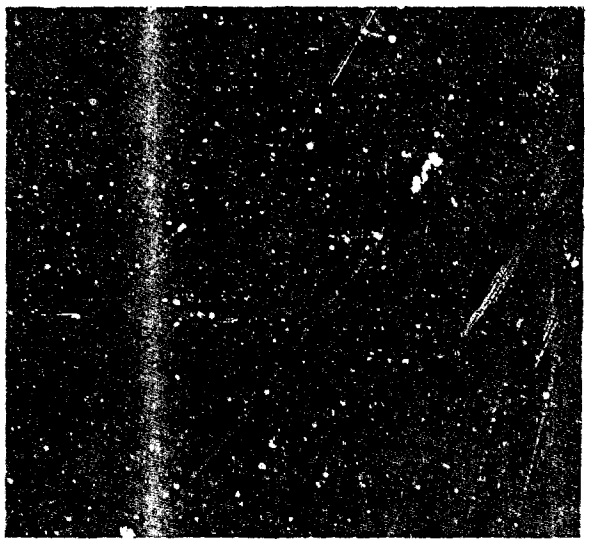

Figure 118 Fractograph Showing a Transgranular Fracture Mechanism with Many Fine-Line Markings on the Fracture Facets.

SECTION VI

DISCONTINUITY STRESS ANALYSIS

1. INTRODUCTION

The fabrication of large pressure vessels very often introduces contour deviations in the vessel. Among the deviations most frequently encountered are:

(1) Longitudinal radial mismatch

(2) Circumferential radial mismatch

(3) Longitudinal angular mismatch

(4) Circumferential angular mismatch

These deviations cause a change in the stress pattern from that which would occur in a pressurized geometrically perfect vessel. A knowledge of the stresses is needed in order to establish tolerance limits on the amount of deviation that can be permitted in the structure, as well as in defining the allowable defect size in a mismatched weld joint, since critical flaw size is proportional to stress squared.

Discontinuities as such do not actually occur in pressure vessels and the term is used to describe local irregularities or discrepancies. This terminology is used because the geometric configuration undergoes abrupt changes at these locations. The most critical such anomalies in cylindrical pressure vessels are those that result in deviations from "roundness" in the cylindrical section. Such irregularities introduce stress patterns which increase the local hoop stresses and thereby produce the highest stresses in the system.

A perfect circular section is the lowest energy configuration for such a vessel and any deviations from this will result in a system of stresses which, upon pressurization, will tend toward this low energy state. While it is relatively simple to apply such general principles to determine behavior of an out-of-round structure, it is much more difficult to obtain a quantitative measure of the significance of such "discontinuities".

Discontinuities are traditionally evaluated by applying minor and often empirical approximate influence factors to the simpler solution for a regular geometry; these techniques are seldom valid in the immediate vicinity of the discontinuity. A second method of analysis has become available which permits the evaluation of detailed geometric configurations with the aid of computers. These procedures do not require a mathematical equation of the geometry but rather consider the structure as an assembly of finite elements. The computers are efficient at calculating the behavior of all these interconnecting parts, permitting precise solution of the matrix formulation.

The 156-inch hydroburst program was designed to demonstrate and develop improved methods of performance prediction, including verification of analytical strength analysis methods. The assumptions for the analytical investigation included all visible and experimentally determined defects. Measurements were taken on the case in the region of the longitudinal welds prior to the hydroburst program and compared to similar measurements taken immediately after the case had been fabricated. The differences in the measurements indicated that permanent set had occurred in the interim. The most severe discontinuity in the 156-inch case was a circumferential angular mismatch as shown in Figure 119.

A comprehensive plane strain discontinuity stress analysis of this mismatch was conducted, utilizing a modified nonlinear stress analysis computer program written by Dr. L. R. Herrmann. A comparison of Dr. Herrman's analysis and the available Swedlow's (as programmed by J. Ary of Edwards Air Force Base) is presented in Table VII.

TABLE VII

COMPARISON OF HERRMANN AND SWEDLOW PROGRAMS

	L. R. Herrmann	J. Swedlow (Programmed by J. Ary)
Strain-displacement	Nonlinear, e.g., $\epsilon_{11} = \frac{\partial u}{\partial x} - \frac{1}{2}\left[\left(\frac{\partial u}{\partial x}\right)^2 + \left(\frac{\partial v}{\partial x}\right)^2\right]$	Linear, e.g., $\epsilon_{11} = \frac{\partial u}{\partial x}$
Formulation (in terms of deformed or undeformed body)	Deformed Body a. Uses true stress b. Loads applied on deformed boundary	Undeformed Body a. Uses engineering stress b. Loads applied on original boundary
Stress-strain law	Modified Hookes' Law for large strains where elastic constants can be specified as secant modulus as function of maximum principal strain	Uses incremental plasticity theory due to Reuss although it is not know whether or not the unloading feature has been programmed
Basic formulation	Equilibrium by variational method (displacements unknown)	Stress function
Plane stress or strain	Plane strain or stress	Plane strain or stress
Finite element or difference	Finite element	Finite difference
Grid spacing	Arbitrary (triangular elements)	(Constant mesh spacing)
Principal limitation	Poor stress-strain law	Based on a linear strain-displacement law which does not consider effects of changes in geometry under load
Program modifications required	Adapt Hencky's deformation theory which requires determination of E_{sec} and μ_{pl} versus effective strain. Change E_{sec} program to modify μ_{pl} and based on effective strain rather than principal strain	Change program to modify geometry after each load increment. This may be rather difficult since a stress formulation is used and the unknowns are the values of the stress function at each node rather than displacement

Primary requirements for the analysis were:

(1) The theory must account for effects of changes in geometry under load.

(2) The stress-strain law should be capable of predicting pressure-strain (or deformation) behavior of a perfectly round chamber.

Dr. Herrmann's program was selected for the analysis. A detailed description of the program is presented in subsection 4.

Additional analyses performed in areas of possible failure include those below:

- The aft closure-adapter bolts failed prematurely
- The tapered pins were ejected

2. STRUCTURAL DESCRIPTION

The hydroburst chamber consisted of two segments attached together by a tapered pin clevis joint, the male and female portions in the forward and aft segments, respectively. The outside diameter of the chamber was 154.90 inches, and the wall thickness was $0.390 \begin{smallmatrix}+0.036\\-0.026\end{smallmatrix}$ inches. The chamber dimensions are shown in Figure 3. Each segment was composed of two plates of steel rolled and welded and attached together by a girth weld.

The forward dome was fabricated from six partial gore plates and a dollar plate welded together. A cylindrical skirt was welded to the closure through a double ring just prior to the elliptical tangency plane. Similarly, the aft dome was fabricated from gore plates welded together. A nozzle adapter was bolted to the dome, and a hydrotest closure was bolted to the adapter.

A visual examination of the 156-inch motor case prior to the hydrotest resulted in the following observations and conclusions:

(1) A "dutch patch" was visible on the aft closure. This is a relatively low stress location and was not considered significant.

(2) An apparent indentation was on the circumferential weld on the forward cylinder, forward segment, and on the forward cylinder, aft segment. The indentations appeared negligible.

(3) There was apparent "sea gulling" of the longitudinal welds.

(4) Several retainers for the joint pins were bent and loose. It was recommended that all retainers be checked, and the damaged one repaired.

Available vidigage dimensions were reviewed. The minimum thickness was 0.375 inches at approximately one inch from the aft course longitudinal weld. Ultrasonic thickness measurements taken of the segments are shown in Section II.

Accurate case contour definition was obtained by measuring the rise of the case over six-inch chord lengths spaced one-inch apart for thirty inches on either side of the longitudinal weld at six different locations. These data were then matched with the vidigage measurements of thickness to establish the shell contour.

The most severe discontinuity in the longitudinal weld based on measured data is shown in Figure 119.

Based on results of Pittsburgh Testing Laboratory data for tensile specimens aged with various cylinders of forward and aft segments (see Table VIII), following are the measured case steel properties:

Minimum yield strength (0.2% offset)	240,000 psi
Minimum ultimate tensile strength	255,000 psi
Elongation (1.4-inch gage)	8%
Reduction in area	30%

The chamber design analysis was based on an MEOP chamber pressure of 875 psig determined for maximum operating temperature plus three-sigma variation of pressure.

Design yield = MEOP x safety factor = 875 x 1.15 = 1004 psi

The estimate of hydrostatic burst pressure was based upon the assumption that the minimum thickness values measured one inch from the weld extended into the heat affected zone, and that the uniaxial strengths of the welds were applicable because of the expected plastic flow on the inside surface near the weld. The calculated burst pressures to achieve membrane hoop stresses corresponding to the strengths listed in Table VIII are shown in Table IX. The anticipated burst pressure based on measured minimum ultimate strength of the welded samples was 1280 psi, to occur in the forward cylinder of the aft segment.

HYDROSTATIC TEST METHODS

The 156-inch diameter motor was cleaned around the longitudinal weld and inspected by use of visual, ultrasonic and dye penetrant methods to determine flaws and growth of defects. The assembled motor case was supported at each end of the skirt by 156-inch diameter pillow blocks. A cable was secured over the aft closure and the motor was tied by two cables located on each segment. When the assembly and the inspections were completed, test instrumentation consisting of redundant pressure transducers and 36 strain gages were located internally and externally on the

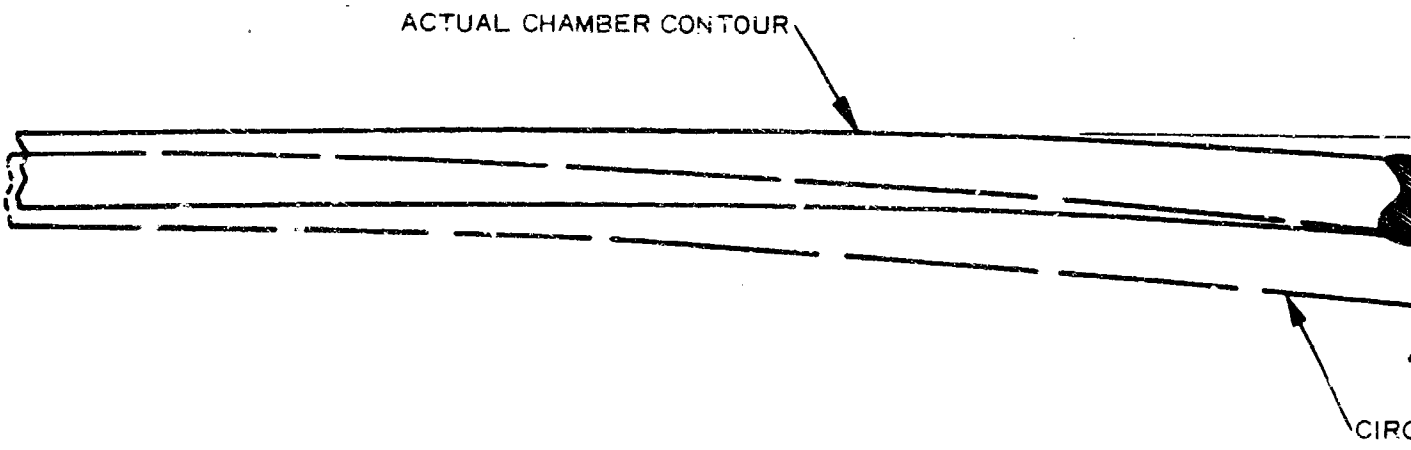

SCALE: FULL

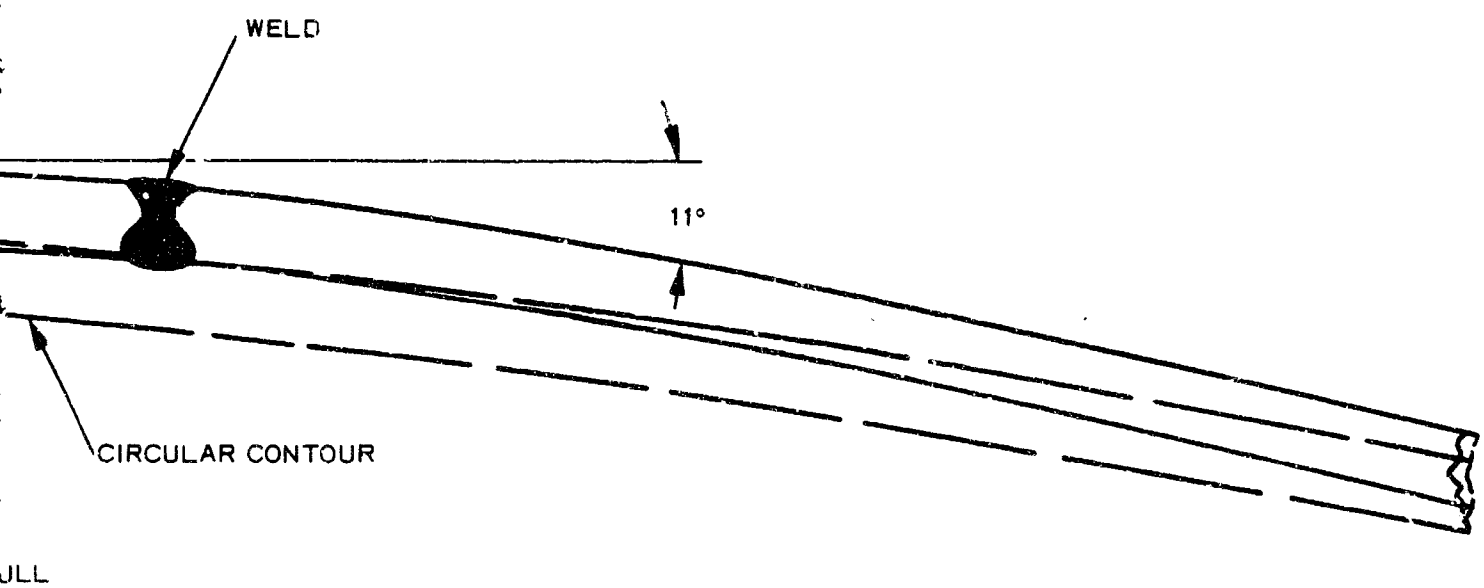

Figure 119 Typical Contour Measurement Depicting Peaking

2

TABLE VIII
TENSILE STRENGTHS AND CALCULATED PRESSURES FOR 156-INCH DIAMETER MOTOR CASE

	Forward Segment		Aft Segment	
	Weld 1284	Weld 1282	Weld 1283	Weld 1285
Parent metal strengths				
Minimum yield (psi)	244,000*	267,000	266,000	285,000
Average yield (psi)	248,000*	270,000	266,000	286,000
Minimum ultimate (psi)	257,000*	277,000	273,000	291,000
Average ultimate (psi)	258,000	279,000	274,000	291,000
Weld metal strengths				
Minimum yield (psi)	240,000*	247,000	257,000	257,000
Average yield (psi)	246,000*	254,000	261,000	260,000
Minimum ultimate (psi)	257,000	255,000*	263,000	266,000
Average ultimate (psi)	259,000*	262,000	267,000	268,000

* The minimum value in a row.

TABLE IX
CALCULATED PRESSURES TO ACHIEVE MEMBRANE HOOP STRESS†, ASSUMING NOMINAL RADIUS CYLINDER WITH MINIMUM MEASURED THICKNESS

	Forward Segment		Aft Segment	
	Weld 1284	Weld 1282	Weld 1283	Weld 1285
Minimum yield in parent metal (psi)	1270*	1400	1295	1383
Average yield in parent metal (psi)	1290*	1415	1295	1388
Minimum yield in weld (psi)	1249	1295	1251	1247*
Average yield in weld (psi)	1280	1332	1271	1262*
Minimum ultimate in parent metal (psi)	1337	1452	1229*	1413
Average ultimate in parent metal (psi)	1343	1463	1334*	1413
Minimum ultimate in weld (psi)	1337	1337	1280*	1291
Average ultimate in weld (psi)	1348	1373	1300*	1301

† Corresponding to those listed in Table VI-2.

* The minimum value in a row.

chamber. Standard bonded strain gage pressure transducers of 0 to 2000-psig capacity were used.

Strain gages were located (based on past data and analyses) at the most critical locations along the longitudinal weld where the maximum stresses were anticipated.

The 36 postyield uniaxial gages were applied at nine locations, in pairs placed at right angles in order to determine principal strains, at the inside and outside of the motor case. These data were to be used for correlating uniaxial tensile stress-strain data with biaxial stress-strain results.

4. METHOD OF DISCONTINUITY STRESS ANALYSIS

The structural analysis of complex solids subjected to arbitrary loads is often required in the aerospace industry. The solution of the arbitrary three-dimensional stress problem, however, is beyond the present state of the art. Yet, with the aid of electronic computers, a large number of practical two-dimensional problems may be readily solved.

The discontinuity stress analysis utilizes a finite element method to determine the stresses, strains, and displacements within the complex two-dimensional structure. Nonlinear material properties and large deformations are considered by a successive iterative technique. The governing equations are given in the following sections. This program may be used for plane stress, plane strain, and generalized plane strain types of solutions.

In the finite element approximation of solids, the continuous structure is replaced by a system of elements which are interconnected at joints or nodal points. Equilibrium equations, in terms of unknown nodal point displacements, are developed at each nodal point.

A complete set of equations for all elements in the structure is solved by means of an elimination simultaneous equation technique.

a. Large Deformation Analysis

There are two basic approaches to the formulation of a large deformation analysis; the difference depends on expressing the equations in terms of the deformed or the undeformed geometry of the body. The convenience of one or the other approach is contingent on the type of boundary conditions. When a surface pressure is specified it is usually most convenient to express the analysis in terms of the deformed geometry.

The material coordinate system (a system that is inherently attached to the body) will be denoted by (x^i) and will be selected such that in the deformed body, it coincides with a spatial rectangular Cartesian system (z^i); in the undeformed body the (x^i) coordinate system will be curvilinear

(Figure 120). The coordinates in the x system of a material point P are (x^1, x^2, x^3) for both the deformed and the undeformed positions. The coordinates in the spatial system of point P are (x^1, x^2, x^3) for the deformed body and $(x^1-u^1, x^2-u^2, x^3-u^3)$ for the undeformed body. The components of the displacement of point P are denoted by u^i. The final and initial locations of point P are shown in Figure 121. The distances in the deformed and undeformed body between the points P and P' are respectively denoted as dS and dS_o. The squares of these distances are given by (where δ_{ij} denotes the Kronecker delta):

$$(dS)^2 = \delta_{ij}\, dz^i\, dz^j \tag{1}$$

$$(dS_o)^2 = \delta_{ij}\, dz^i\, dz^j \tag{2}$$

Utilizing the fact that in the deformed body $z^i = x^i$ and in the undeformed body $z^i = x^i - u^i$, Equations (1) and (2) become

$$(dS)^2 = \delta_{ij}\, dx^i\, dx^j \tag{3}$$

$$(dS_o)^2 = h_{ij}\, dx^i\, dx^j \tag{4}$$

where

$$h_{ij} = \delta_{\alpha\beta} \left(\delta_i^\alpha - \frac{\partial u^\alpha}{\partial x^i}\right) \left(\delta_j^\beta - \frac{\partial u^\beta}{\partial x^i}\right) \tag{5}$$

Equations (3) and (4) are the expressions for the final and initial distances between P and P' expressed in the material coordinate system. The measure of deformation $(dS)^2 - (dS_o)^2$ defines the strain tensor E_{ij}, i.e.,

$$(dS)^2 - (dS_o)^2 = 2E_{ij}\, dx^i\, dx^j \tag{6}$$

Utilizing Equations (3) and (4), the following expression is obtained

$$E_{ij} = \frac{1}{2}(\delta_{ij} - h_{ij}) \tag{7}$$

The strain tensor (referred to as the large strain tensor) E_{ij} is expressed in terms of the displacements by using Equation (5); in this utilization the conditions of plane strain are employed (i.e., $\frac{\partial u^1}{\partial x^3} = \frac{\partial u^2}{\partial x^3} = u^3 = 0$), for simplicity let $u^1 = u$, $u^2 = v$, $x^1 = x$ and $x^2 = y$

$$E_{11} = \frac{\partial u}{\partial x} - \frac{1}{2}\left[\left(\frac{\partial u}{\partial x}\right)^2 + \left(\frac{\partial v}{\partial x}\right)^2\right] \tag{8}$$

$$E_{12} = E_{21} = \frac{1}{2}\left(\frac{\partial u}{\partial y} + \frac{\partial v}{\partial x}\right) - \frac{1}{2}\left(\frac{\partial u}{\partial x}\frac{\partial u}{\partial y} + \frac{\partial v}{\partial x}\frac{\partial v}{\partial y}\right) \tag{9}$$

$$E_{22} = \frac{\partial v}{\partial y} - \frac{1}{2}\left[\left(\frac{\partial u}{\partial y}\right)^2 + \left(\frac{\partial v}{\partial y}\right)^2\right] \tag{10}$$

$$E_{33} = E_{23} = E_{13} = 0 \tag{11}$$

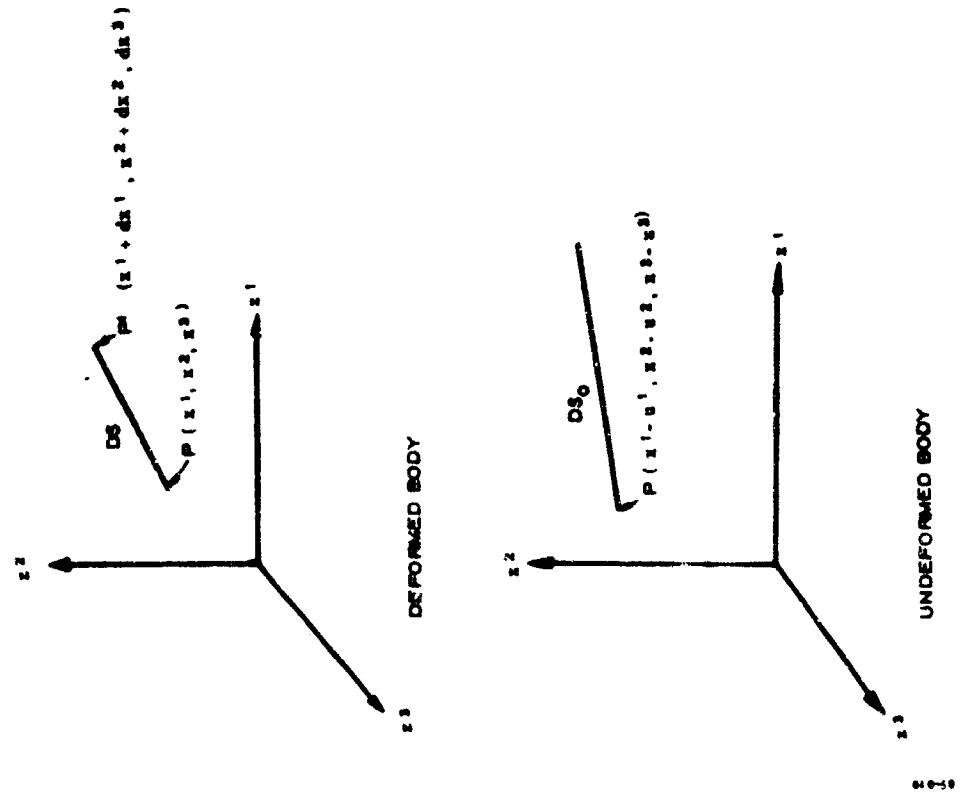

Figure 121 Location of Two Points in the Deformed and Undeformed Body

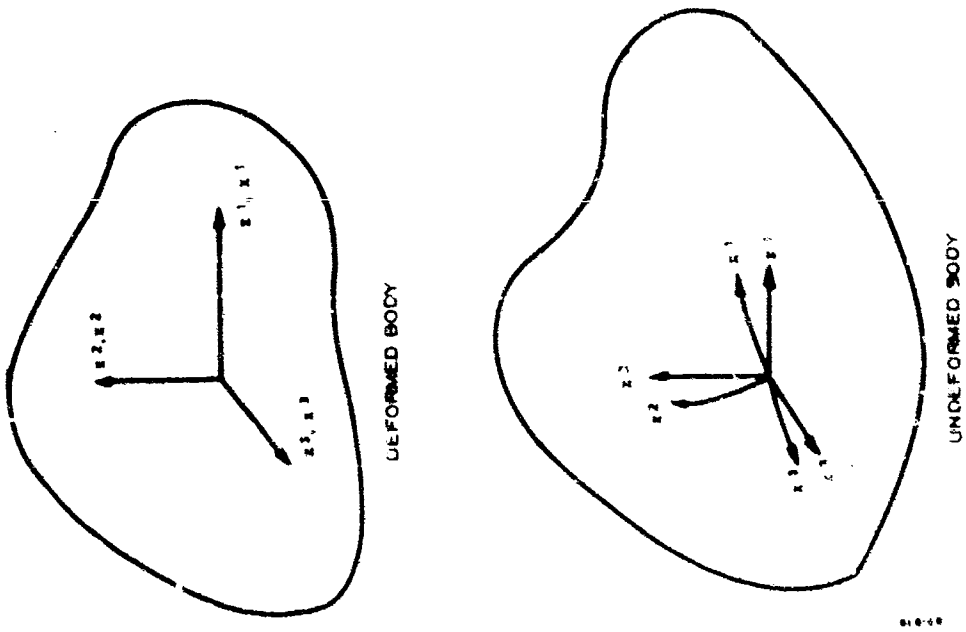

Figure 120 Coordinate Systems

The equilibrium equations, written in terms of the true stress, for the deformed body are

$$\frac{\partial \sigma_{11}}{\partial x} + \frac{\partial \sigma_{12}}{\partial y} = 0 \tag{12}$$

$$\frac{\partial \sigma_{12}}{\partial x} + \frac{\partial \sigma_{22}}{\partial y} = 0 \tag{13}$$

Equations (8) through (11) define the two-dimensional deformation state for the body; equilibrium of the body is specified by Equations (12) and (13). In the following section the constitutive law will be developed which determines the relationship between the stress and strain components. As a preliminary to this consideration, the relationships between the extension ratios and the large strain components for a homogeneous strain state will be established. The extension ratio λ is equal to the quotient of the final length over the initial length, i.e.,

$$\lambda_i = \frac{L_i}{L_{oi}} \tag{14}$$

By utilizing Equation (5), the desired relations are found to be

$$E_{ij} = \begin{bmatrix} \frac{1}{2}\left[1 - \left(\frac{1}{\lambda_1}\right)^2\right] & 0 & 0 \\ 0 & \frac{1}{2}\left[1 - \left(\frac{1}{\lambda_2}\right)^2\right] & 0 \\ 0 & 0 & \frac{1}{2}\left[1 - \left(\frac{1}{\lambda_3}\right)^2\right] \end{bmatrix} \tag{15}$$

Equation (15) will be used in the interpretation of simple tests. In addition, the physical significance of any general strain state may be determined by finding the principal strains and then interpreting them in terms of extension ratios by utilizing Equation (15).

In the following section, it will also be necessary to have a measure of the volume change of the deformed body. The volumes of an element of material (specified by dx^1, dx^2 and dx^3) in the deformed and undeformed state, will be denoted as V and V_o, respectively, and are given by

$$V = \sqrt{|\delta_{ij}|}\, dx^1\, dx^2\, dx^3 \tag{16}$$

$$V_o = \sqrt{|h_{ij}|}\, dx^1\, dx^2\, dx^3 \tag{17}$$

where $|h_{ij}|$ is the determinant of h_{ij}.

With Equations (7) and (11), and noting that $|\delta_{ij}| = 1$,

$$V = dx^1\, dx^2\, dx^3 \tag{18}$$

$$V_o = \sqrt{(1 - 2E_{11})(1 - 2E_{22}) - 4(E_{12})^2}\, dx^1\, dx^2\, dx^3 \tag{19}$$

The measure of volume change "e_v" to be employed is defined as

$$e_v = \frac{V^2 - V_o^2}{2V^2} \tag{20}$$

or

$$e_v = \frac{\Delta V}{V_o} - \frac{3\left(\frac{\Delta V}{V_o}\right)^2 + 2\left(\frac{\Delta V}{V_o}\right)^3}{2 + 4\left(\frac{\Delta V}{V_o}\right) + 2\left(\frac{\Delta V}{V_o}\right)^2} \tag{21}$$

where

$$\Delta V = V - V_o \tag{22}$$

From Equations (18), (19) and (20), the measure of volume change can be expressed as

$$e_v = (E_{11} + E_{22}) - 2\,(E_{11}\, E_{22} - E_{12}^2) \tag{23}$$

or

$$e_v = (E_{11} + E_{22}) + c \tag{24}$$

where

$$c = -2\,(E_{11}\, E_{22} - E_{12}^2) \tag{25}$$

b. Material Properties

The problem under consideration is the plane strain response of a rocket motor case to pressurization; the critical time, t_o (time at which the critical state of stress and deformation occurs) is assumed to coincide with the time when maximum pressure is reached. It is anticipated that the state of stress and strain existing throughout the case at some time, t, during pressurization will be shown in Figure 122.

If the history of the pressure, p, is taken to be linear, it is assumed that the history of σ_1 will also be approximately linear. Thus, a constitutive law which governs the behavior of the strain and stress state may be used as an approximate description of the material mechanical response.

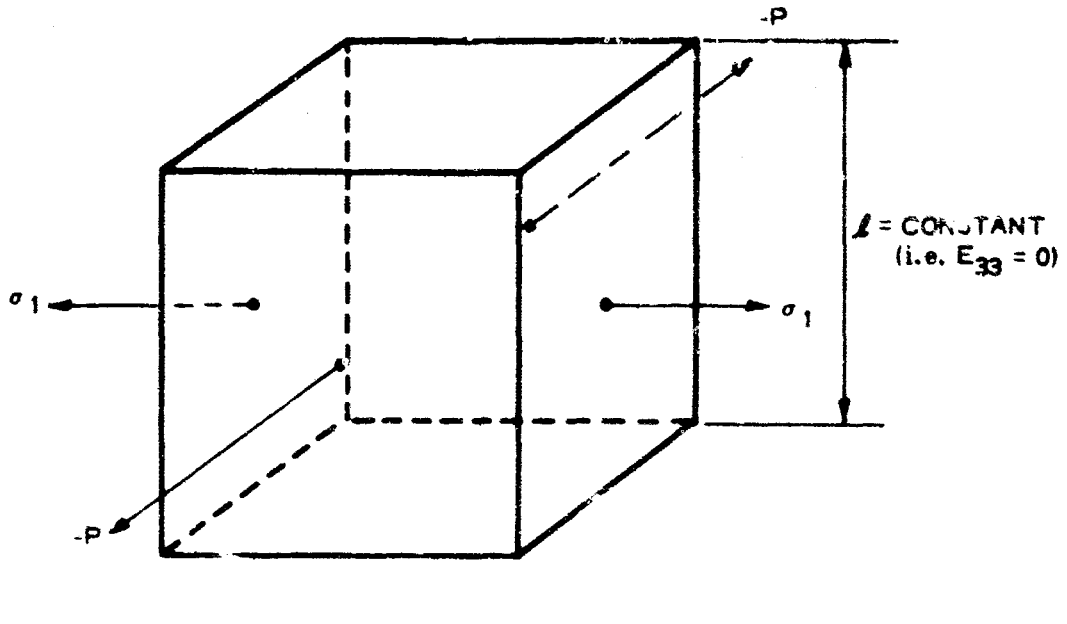

Figure 122 Anticipated Stress State Occurring in the Pressurized Case

For a typical region, the relationship between the true mean stress and the measure of volume change "e_v" [Equation (20)] will be expressed as ($\sigma = \frac{\sigma_{11} + \sigma_{22} + \sigma_{33}}{3}$

$$e_v = \frac{3(1 - 2K_2)\,\sigma}{2K_1(1 + K_2)} \tag{26}$$

By defining a nondimensional mean pressure by the variable H,

$$H = \frac{3\sigma}{2K_1(1 + K_2)} \tag{27}$$

Then Equation (26) becomes

$$e_v = (1 - 2K_2)\,H \tag{28}$$

The relationship between the stress and strain components (at time t_o) will then be written as [c is defined by Equation (25)]:

$$\sigma_{11} = 2K_1\,[E_{11} + K_2\,H + c/3] \tag{29}$$

$$\sigma_{22} = 2K_1\,[E_{22} + K_2\,H + c/3] \tag{30}$$

Equations (28), (29) and (30) express the approximate constitutive equations that will be used to describe the behavior of the material. The form of the equations have been so selected that they are valid for both compressible and incompressible materials. Incompressibility is expressed by setting the parameter K_2 equal to one-half. For an elastic material subjected to infinitesimal strains, the parameters K_1 and K_2, respectively, become the shear modulus and Poisson's ratio.

Alternatively, the dependence upon the principal stress σ_1 can be expressed as a dependence upon the principal strain E. Hence, the dependence of the parameters K_1 and K_2 upon the principal strain E_1 must be established. These can be obtained by knowing the extension ratios λ_1 and λ_2 that correspond to the principal stresses σ_1 and σ_2. Then the values of E_1 and E_2 may be calculated. The parameters K_1 and K_2 may then be determined from the solution of Equations (29) and (30).

c. Iterative Solution Procedure

The equations governing the behavior of the motor case are the equilibrium equations (12, 13), the strain displacement relations (8, 9, 10, 11), and the stress-strain law (28, 29, 30). These equations, when combined with the appropriate boundary conditions (expressed in terms of the deformed geometry), constitute the boundary value problem that must be solved. Nonlinear effects appear in (a) the strain-displacement relationships, (b) the stress-strain law (c is a nonlinear function of the strain), and (c) the boundary conditions (the displacements must be known before the geometry of the deformed boundary may be described). The solution of this nonlinear boundary value problem is obtained by an iterative procedure. The nonlinear effects for each iteration will be approximately evaluated by utilizing the results from the previous iteration. Thus, for example, the coordinates of a point in the deformed body for the βth iteration will be approximated by

$$z^{i(\beta)} = z^{i(0)} + u^{i(\beta - 1)} \tag{31}$$

where $z^{i(0)}$ denotes its position in the undeformed body and $u^{i(\beta - 1)}$, the displacement components calculated in the $(\beta - 1)$ iteration.

The strain displacement relationships will be expressed in the form

$$E_{ij}^{(\beta)} = \epsilon_{ij}^{(\beta)} + \sigma_{ij}^{(\beta - 1)} \tag{32}$$

where

$$\epsilon_{ij} = \begin{bmatrix} \dfrac{\partial u}{\partial x} & \dfrac{1}{2}\left(\dfrac{\partial u}{\partial y} + \dfrac{\partial v}{\partial x}\right) \\ \dfrac{1}{2}\left(\dfrac{\partial u}{\partial y} + \dfrac{\partial v}{\partial x}\right) & \dfrac{\partial v}{\partial y} \end{bmatrix} \tag{33}$$

and

$$\alpha_{ij} = \begin{bmatrix} -\frac{1}{2}\left[\left(\frac{\partial u}{\partial x}\right)^2 + \left(\frac{\partial v}{\partial x}\right)^2\right] & -\frac{1}{2}\left[\frac{\partial u}{\partial x}\frac{\partial u}{\partial y} + \frac{\partial v}{\partial x}\frac{\partial v}{\partial y}\right] \\ -\frac{1}{2}\left[\frac{\partial u}{\partial x}\frac{\partial u}{\partial y} + \frac{\partial v}{\partial x}\frac{\partial v}{\partial y}\right] & -\frac{1}{2}\left[\left(\frac{\partial u}{\partial y}\right)^2 + \left(\frac{\partial v}{\partial y}\right)^2\right] \end{bmatrix} \tag{34}$$

The stress-strain law will be written as ($K_1^{(\beta-1)}$ is determined by the value of $E_1^{(\beta-1)}$)

$$\epsilon_{11}^{(\beta)} + c_{22}^{(\beta)} = (1 - 2K_2^{(\beta-1)})\, H^{(\beta)} - c^{(\beta-1)} - \alpha_{11}^{(\beta-1)} - \alpha_{22}^{(\beta-1)} \tag{35}$$

$$\sigma_{11}^{(\beta)} = 2K_1^{(\beta-1)}\left[\epsilon_{11}^{(\beta)} + K_2^{(\beta-1)}\, H^{(\beta)} + \alpha_{11}^{(\beta-1)} + \tfrac{1}{3}\, c^{(\beta-1)}\right] \tag{36}$$

$$\sigma_{22}^{(\beta)} = 2K_1^{(\beta-1)}\left[\epsilon_{22}^{(\beta)} + K_2^{(\beta-1)}\, H^{(\beta)} + \alpha_{22}^{(\beta-1)} + \tfrac{1}{3}\, c^{(\beta-1)}\right] \tag{37}$$

$$\sigma_{12}^{(\beta)} = 2K_1^{(\beta-1)}\left[\epsilon_{12}^{(\beta)} + \alpha_{12}^{(\beta-1)}\right] \tag{38}$$

Thus, for any given iteration, the unknowns appear in a linear fashion and the analysis reduces to one of solving a series of linear problems. The governing equations written in this way are identical in form to those of a linear elastic analysis where there are anisotropic thermal effects. The technique that will be used to solve this set of equations is the finite element procedure. It was necessary to utilize this particular formulation in order to consider incompressible and nearly incompressible materials. Preliminary to the development of the finite element solution, it is necessary to express the governing equations in terms of a variational equation. By including the nonlinear terms in the variational function, the following function is obtained:

$$\begin{aligned} F^{(\beta)} = \iint_{R^{(\beta-1)}} \mu \Big\{ & \left[\epsilon_{11}^{(\beta)}\right]^2 + \left[\epsilon_{22}^{(\beta)}\right]^2 + 2\left[\epsilon_{12}^{(\beta)}\right]^2 + 2\nu\, H^{(\beta)}\left[\epsilon_{11}^{(\beta)} + \epsilon_{22}^{(\beta)}\right] - \nu(1-2\nu)\left[H^{(\beta)}\right]^2 \\ & + 2\nu\, H^{(\beta)}\left[\alpha_{22}^{(\beta-1)} + \alpha_{11}^{(\beta-1)} + c^{(\beta-1)}\right] + 2\epsilon_{11}^{(\beta)}\left[\alpha_{11}^{(\beta-1)} + \tfrac{1}{3}\, c^{(\beta-1)}\right] + 2\epsilon_{22}^{(\beta)}\left[\alpha_{22}^{(\beta-1)} \right. \\ & \left. + \tfrac{1}{3}\, c^{(\beta-1)}\right] + 4\epsilon_{12}^{(\beta)}\, \alpha_{12}^{(\beta-1)} \Big\} - \int_{S_1^{(\beta-1)}} \left[P_x^{(\beta-1)}\, u^{(\beta)} \right. \\ & \left. + P_y^{(\beta-1)}\, v^{(\beta)}\right] dS \end{aligned} \tag{39}$$

where

$$\mu = K_1^{(\beta-1)} \tag{40}$$

$$\nu = K_2^{(\beta-1)} \tag{41}$$

The surface integral is to be evaluated over the deformed body as defined by the previous iteration and the line integral is to be evaluated over that portion of the deformed boundary where surface stresses are prescribed.

The finite element solution is formulated by representing the case cross-section by a series of triangles, selecting a trial form of the primary dependent variables (H, μ and ν) within each triangle and choosing their final form by the Ritz procedure 7, 8, 9, 10. A coarse finite element representation of a portion of case cross-section is shown in Figure 123. For convenience in the following derivation, the superscript indicating the number of the iteration will be deleted (i.e., $c_{ij}^{(\beta)}$ will be denoted as c_{ij}, etc.). The family of trial functions for use in the Ritz procedure is formed by assuming that the displacements are linear within each triangular element (expressed as a function of the values of the displacements at the nodes) and continuous across the element interfaces and that the mean pressure variable H is constant within each element. A particular member of the family is uniquely determined by assigning values to all the node values of the displacements and the element values of H. These values will be selected by setting the variation of F equal to zero.

The case cross-section is represented by Q elements; associated with these Q elements are N nodal points (a typical nodal point is denoted by n). The values of the displacements at the nth nodal point are denoted as u^n and v^n and the coordinates of the point by (x^n, y^n). The value of H in element q is denoted as H^q. A particular node n is common to M elements: in the consideration of the mth element of this group, it will be represented as shown in the lower portion of Figure 124. The coordinates of the vertices of this triangle are $x_i = x^n$, $x_j = x^r$, etc. The values of the displacements at its vertices are denoted by $u_m^i = u^n$, $u_m^j = u^r$, etc.

Within the element m, the displacements and H are expressed as

$$u(x, y) = C_1 + C_2 x + C_3 y \tag{42}$$

$$v(x, y) = C_4 + C_5 x + C_6 y \tag{43}$$

$$H = H^m \tag{44}$$

where

$$\begin{bmatrix} C_1 & C_4 \\ C_2 & C_5 \\ C_3 & C_6 \end{bmatrix} = [T] \begin{bmatrix} u_m^i & v_m^i \\ u_m^j & v_m^j \\ u_m^k & v_m^k \end{bmatrix} \tag{45}$$

$$[T] = \frac{1}{2A} \begin{bmatrix} x_j y_k - x_k y_j & x_k y_i - x_i y_k & x_i y_j - x_j y_i \\ y_j - y_k & y_k - y_i & y_i - y_j \\ x_k - x_j & x_i - x_k & x_j - x_i \end{bmatrix} \tag{46}$$

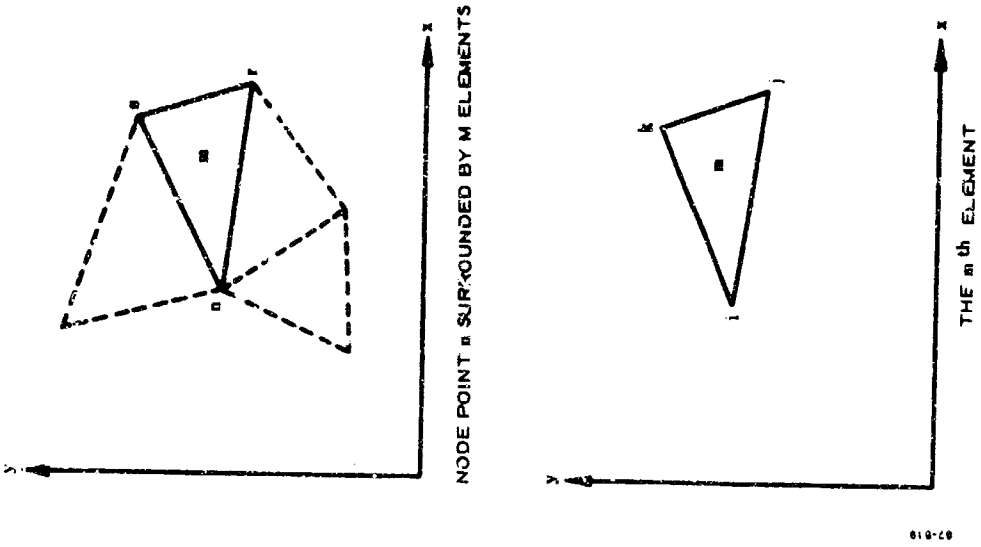

Figure 124 Detailed View of the Elements Surrounding Node Point n

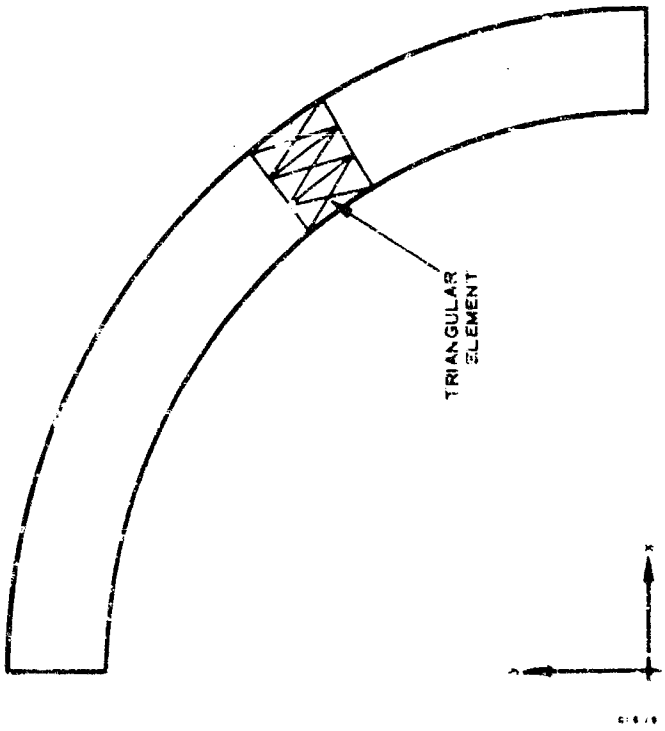

Figure 123 Finite Element Representation of Chamber

$$A = \frac{1}{2}\left[x_j(y_k - y_i) + x_i(y_j - y_k) + x_k(y_i - y_j)\right] \tag{47}$$

The variational function F for the system is the sum of the values of the function for each element, i.e.,

$$F = \sum_{q=1}^{Q} F^q \tag{48}$$

Upon substituting Equations (42), (43), and (44) into Equations (48) and (39) and setting the variation with respect to the unknown parameters u^n and v^n equal to zero, the following equations are obtained (note that only the M triangles surrounding node n contribute to these equations):

$$\sum_{m=1}^{M}\left[B_{11}\,u_m^i + B_{12}\,u_m^j + B_{13}\,u_m^k + B_{21}\,v_m^i + B_{22}\,v_m^j + B_{23}\,v_m^k + B_3 H^m\right] = \sum_{m=1}^{M}\left[D_1(\alpha_{11} + \tfrac{1}{3}\,c) + D_2\,\alpha_{12}\right] \tag{49}$$

and

$$\sum_{m=1}^{M}\left[B_{41}\,u_m^i + B_{42}\,u_m^j + B_{43}\,u_m^k + B_{51}\,v_m^i + B_{52}\,v_m^j + B_{53}\,v_m^k + B_6 H^m\right] = \sum_{m=1}^{M}\left[D_2(\alpha_{22} + \tfrac{1}{3}\,c) + D_1\,\alpha_{12}\right] \tag{50}$$

where

$$B_{1\ell} = \mu A\,(2\,T_{21}\,T_{2\ell} + T_{31}\,T_{3\ell}) \tag{51}$$

$$B_{2\ell} = \mu A\,T_{31}\,T_{2\ell} \tag{52}$$

$$B_3 = 2\mu\nu A\,T_{21} \tag{53}$$

$$B_{4\ell} = \mu A\,T_{21}\,T_{3\ell} \tag{54}$$

$$B_{5\ell} = \mu A\,(2\,T_{31}\,T_{3\ell} + T_{21}\,T_{2\ell}) \tag{55}$$

$$B_6 = 2\mu\nu A\,T_{3\ell} \tag{56}$$

$$D_1 = -2\mu A\,T_{21} \tag{57}$$

$$D_2 = -2\mu A\,T_{31} \tag{58}$$

Setting the variation of F with respect to the unknown parameter H^m equal to zero, yields the equation

$$B_{71}u_m^i + B_{72}u_m^j + B_{73}u_m^k + B_{81}v_m^i + B_{82}v_m^j + B_{83}v_m^k + B_9 H^m = D_3 (\alpha_{11} + \alpha_{22} + c) \tag{59}$$

where

$$B_{7\ell} = 2\mu \nu A T_{2\ell} \tag{60}$$

$$B_{8\ell} = 2\mu \nu A T_{3\ell} \tag{61}$$

$$B_9 = -2(1 - 2\nu) \mu \nu A \tag{62}$$

$$D_3 = -2\mu \nu A \tag{63}$$

Thus, setting the variations of F with respect to the 2N node values of the displacements and the Q element values of H* equal to zero yields a total of (2N + Q) equation whose solution determines the approximate values of the displacements and of H. From this solution approximate values of the stresses and strains are calculated by combining Equations (33), (36), (37), and (38). Similarly, the nonlinear terms (α_{11}, etc.) are evaluated and entered into the next iteration.

d. Conclusion

The method of analysis is completely general with respect to geometry and material properties. Complex bodies composed of many different materials can be easily represented. Displacement or stress boundary conditions may be specified at any nodal point within the finite element system. Arbitrary thermal and mechanical loads are possible. Mathematically, it can be shown that the method converges to the exact solution as the number of elements is increased; therefore, any desired degree of accuracy may be obtained. In addition, the finite element approach generates equilibrium equations which produce a symmetric, positive-definite matrix which may be placed in a band form and solved with a minimum of computer storage and time.

While the computer routine described above was used for the discontinuity stress analysis, the finite deformation, nonlinear portion of the computer routine was not required as the material behavior occurred in the elastic range and multiple iterations were not required. No attempt was made to investigate higher pressures to obtain ultimate results in the elastic-plastic regime as the failure occurred below the elastic limit of the case material.

* The case cross-sections were first divided into a grid of quadrilateral elements which were in turn subdivided into four triangles, Figure 125. To facilitate the computations, it was found desirable to select only three of the four values of H (for each quadrilateral) independently and to determine the fourth by the equation $H^1 - H^2 + H^3 - H^4 = 0$.

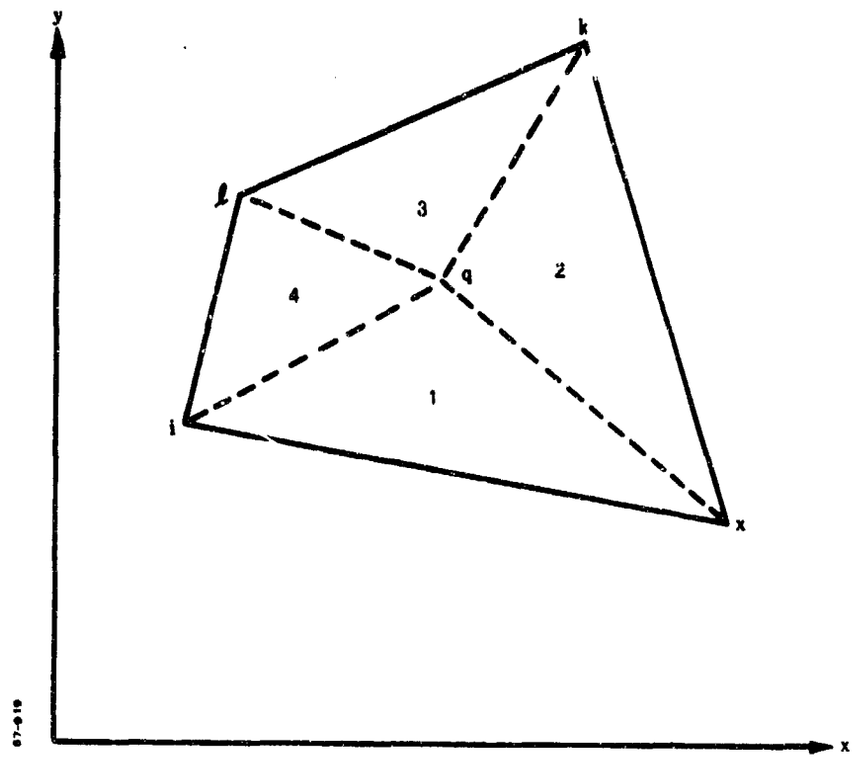

Figure 125 Division of Quadrilateral into Four Triangles

5. DISCUSSION OF ANALYSES

a. Discontinuity Stress Analysis

The discontinuity stress analysis shows that failure would not occur due to the irregular shape of the chamber. The Nonlinear Plane Strain Program No. 287 was used to analyze the chamber's most severe discontinuous cross-section; the results are presented in Figure 126, where the hoop stresses versus circumferential position are plotted. The analysis showed significant effects of bending and shear stresses in the chamber.

At the point of maximum stress, a minimum margin of safety of 0.14 occurs. This margin, based upon the uniaxial membrane ultimate allowable strength and a bending modulus equal to 1.25 times the uniaxial allowable, is adequate to ensure the structural integrity of both the continuous and discontinuous portions of the chamber.

b. Bolt Adapter-Aft Closure

The area chiefly suspected of possible failure was in the bolts. Post-hydroburst inspection of the bolts showed indications of environment deterioration. The Shell of Revolution Program 124 (see Appendix) was used to analyze the loading on the closure forging due to discontinuity stress resultants. The analysis showed a basic bolt load of 44,625 pounds per bolt

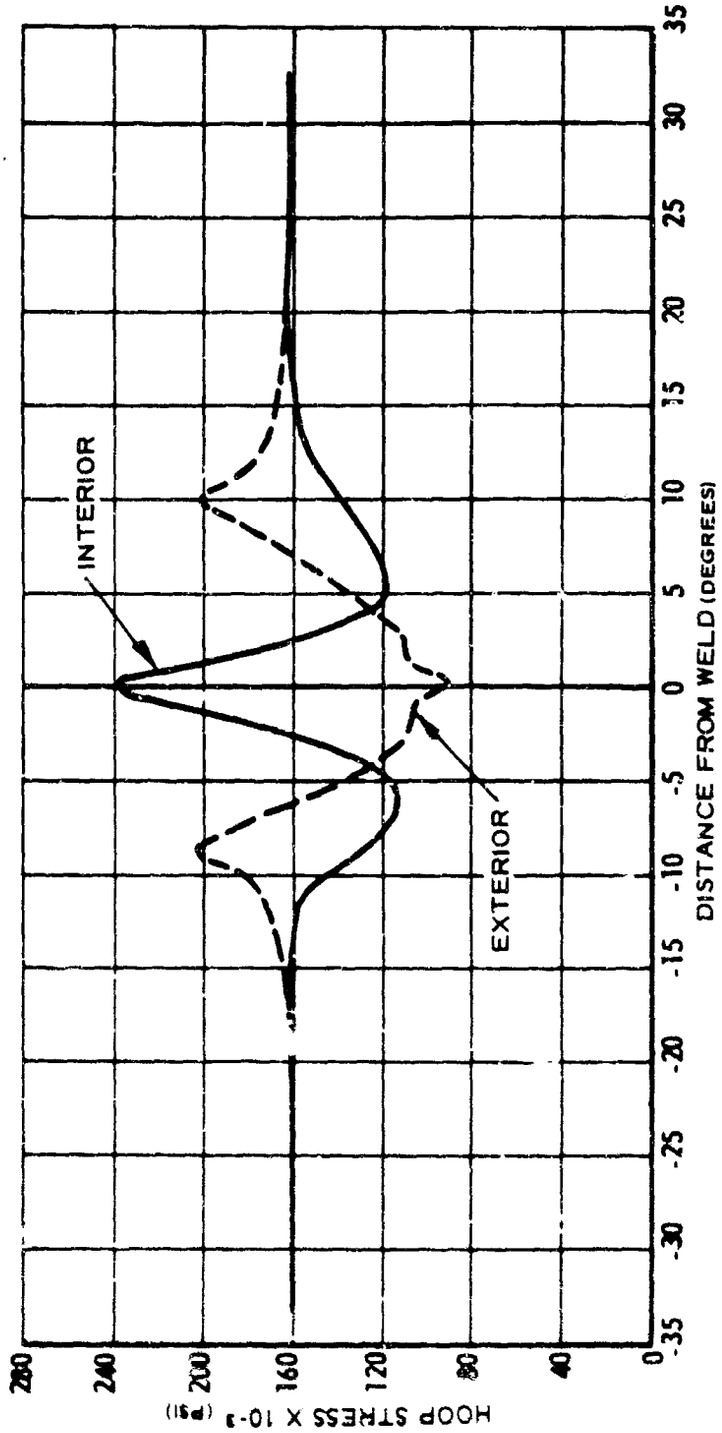

Figure 126 Hoop Stress versus Circumferential Position at Point of Greatest Discontinuity

and 13,985 pounds per bolt due to the interface loads at a pressure of 1038 psi. Comparing these loads with the listed properties of the $^3/_4$-16 UNF bolts (Ref.), the minimum margin of safety is 0.76. At 800 psi, the calculated margin of safety is 1.28; however, a stress of 50% of the proportional limit or greater, as discussed in Section V, is sufficient to produce stress corrosion failure under specific conditions.

c. Pin Joint Analysis

The case consisted of two segments attached by 200 pin clevis joints. The ejection loads on the pins were determined for various levels of pressure loading from 200 psi to 800 psi and are plotted in Figure 127.

The static coefficient of friction, μ, required to balance the pin ejection load for a 5-degree half-angle pin, is 0.0875. When μ is less than 0.0875, the ejection load is reacted by the retainer (or "keeper") bars and cap screws. Average values of μ for metals are tabulated in Ref. 3. The value listed for steel-on-steel lubricated with light machine oil is 0.16. For the hydrotest, the pins were assembled clean and dry (no lubricant), $\mu = 0.58$.

The load calculated to fail the retainer bars is 396 pounds, minimum; 857 pounds, maximum. These loads correspond to anticipated ejection loads for static friction coefficients of 0.085 to 0.082. It is also necessary to keep in mind that dynamic coefficients of friction are much lower than static. The lack of the empirical dynamic data suggests that rapid rate (vibration) tensile tests should be initiated. Calculations for the tapered pin joint are shown in the appendix, subsection 8.

6. EMPIRICAL DATA VERSUS ANALYTICAL RESULTS OF DISCONTINUITY STRESS ANALYSIS

The maximum stress realized in the motor case at 800 psi was compared to the calculated stresses around the longitudinal welds:

Measured stress (psi)	231,300
Calculated stress (psi)	226,000
Circular membrane hoop stress (psi)	162,000

Comparison of the analytical and measured stresses show a relative variation in the maximum interior stresses of 2.3% for the two approaches. This variance is within the accuracy of the pre-test geometric measurements, which was used in the analysis, and strain gage placement and readings. The assumption was made that the measurements of chamber peaking were accurate and were input to the program as such. The comparison of the measured and analytic stresses validate the input data.

[3] Strength of Material, McGraw-Hill Book Company, Inc., New York, 1957.

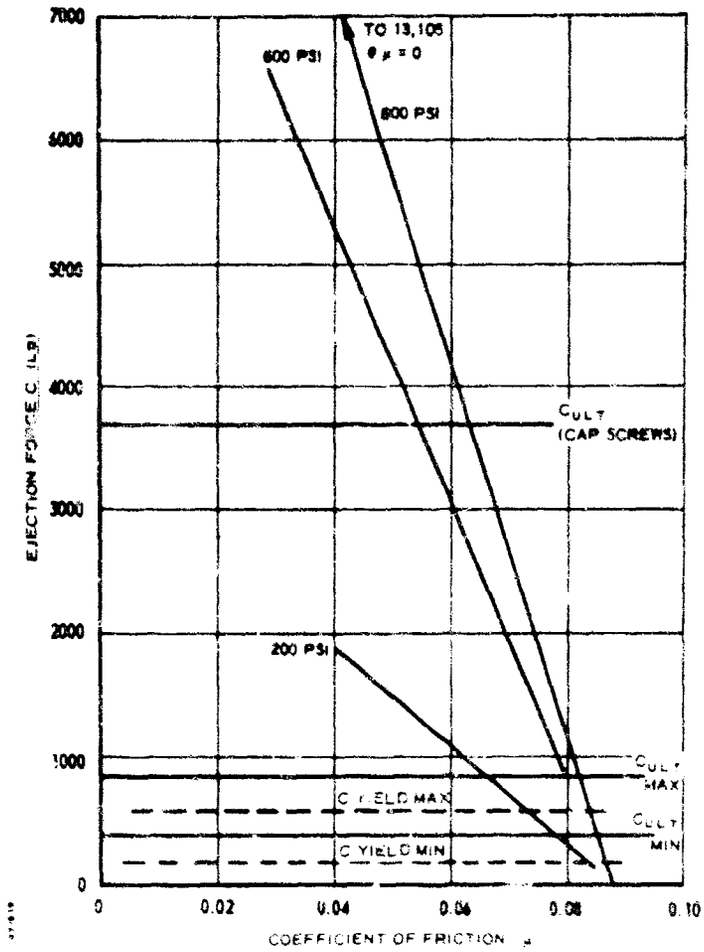

Figure 127 Ejection Force versus Coefficient of Friction

7. CONCLUSIONS

(1) The plane strain analysis of the discontinuities around the longitudinal weld has shown that the failure of the case would not initiate at 800 psi due to these discontinuities. The minimum margin of safety was 0.14. The analysis showed severe localized bending occurred at the weld.

(2) While the stress level in the bolts at 800 psig was not high enough to initiate an overload failure, the presence of stress corrosion could have initiated the premature failure.

(3) Ejection load on the tapered pins in previous tests was sufficient to cause the retainer bars to bend. It is possible that a premature failure of a "keeper" bar initiated the ejection of all the tapered pins. A re-evaluation of the optimum pin taper angle should be made, and the retainer assembly should be designed to withstand higher ejection forces.

(4) To evaluate the assumptions on dynamic ejection of the pins, it is recommended that laboratory tests be performed to simulate those conditions in the motor. Simple pin extraction under rapid-rate vibration and analog tests of the assemblage would give better foundation for analytic assumptions.

8. STRUCTURAL ANALYSIS OF DISCONTINUITY STRESSES

To analyze the effects of nonsymmetry, Lockheed Propulsion Company's Nonlinear Plane Strain Computer Program No. 287 was employed. The program provides a generalized plane strain analysis in that equations have been modified to take into account the effect of any axial strains. The program considers both large and small deformations and nonlinear stress-strain laws.

A finite element variational method of analysis is used in this program. The cross-section of interest is represented by a mesh of quadrilateral elements which can fit arbitrary shapes. Mesh generation routines, for regular geometric shapes, have been incorporated in the program in order to reduce the amount of input preparation required. Equations are then presented for each nodal point, and the set of simultaneous equations form a band type matrix which is solved and gives the required stresses and strains at the center of each element.

The necessary boundary conditions for the analysis are the normal and tangential forces equal to zero at the exterior surface and the normal and tangential forces calculated as a function of internal pressure and equal to zero, respectively, at the interior surface. Since the discontinuities occur near the longitudinal weld, damping of bending stresses is achieved prior to termination of the section under consideration. At the termination of the section analyzed, the boundary conditions must simulate the continuous circular cylindrical contour and are, therefore, the normal displacement, and the tangential forces equal to zero.

The output of the program consists of radial and hoop stresses and strains, shear-stresses, and deflections at each point.

After the hoop stresses were determined the appropriate margin of safety was calculated.

$$\text{Margin of Safety} = \frac{\text{Minimum allowable stress}}{\text{Maximum induced stress}} - 1$$

Minimum yield strength of welded metal = 240,000 psi

Maximum induced hoop stress at 800 psig = 162,000 ± 62,000 psi

$$\text{M.S.} = \frac{1}{\dfrac{162{,}000}{240{,}000} + \dfrac{62{,}000}{1.25 \times 240{,}000}} - 1 = 0.14$$

SECTION VII

NONDESTRUCTIVE TESTING EVALUATION

1. INTRODUCTION AND SUMMARY

This program effort was aimed at providing quantitative data on UT effectiveness in the detection and definition of defects, correlating the inspection results with the characteristics of the actual flaws. Microscopic evaluation of the UT indications was accomplished at both LPC and Mellon Institute. The report from Mellon is included as subsection 2.d at the end of this section (pages 1 - 19).

The microscopic results were accurately predicted by the UT inspection, which had indicated mid-plate, noncontinuous planar delaminations. As expected, all delaminations were associated with heavy banding and were located in the weld heat-affected zone. None were cracks extending into the weld deposit.

Two minor weld defects were detected: a 0.030-inch porosity and a 0.30-inch length lack of fusion. These defects were verified by radiographic inspection at LPC.

2. NONDESTRUCTIVE TESTING

The 156-inch diameter hydroburst chamber was ultrasonically inspected both prior to and after the hydroburst test. The results of the inspections are described in the following.

a. Pre-Hydroburst Inspection

The weld orientation and identification utilized on this chamber are illustrated in Figure 128. Records obtained from the original manufacturing log book, regarding defect size and location in the parent metal adjacent to the weld area, are shown in Table X, and illustrated in Figures 129 through 133. The original tests by the manufacturer utilized longitudinal wave methods and indicated no defects in the parent material adjacent to the longitudinal welds or in the weld bead. Nondestructive testing of the weld consisted of radiographic and dye-penetrant inspection before and after hydrotest at the manufacturer's plant. The longitudinal wave ultrasonic tests were applied to detect banding or delaminations in the plate material adjacent to the weld. Because the longitudinal welds were reported free of delaminations, shear wave testing was used exclusively during pre-hydroburst inspection at LPC.

Based upon case visual evaluation and previous strain gage results, the longitudinal welds in both segments were considered to be the critical areas. Thus, nondestructive inspections conducted prior to hydroburst were concentrated in these regions. In preparation for testing, the protective paint coating was stripped from the longitudinal welds to provide an eight-inch, bare metal band on either side of the welds on the case outside diameter. Insulation and liner from the previous test was not removed from the inner surface.

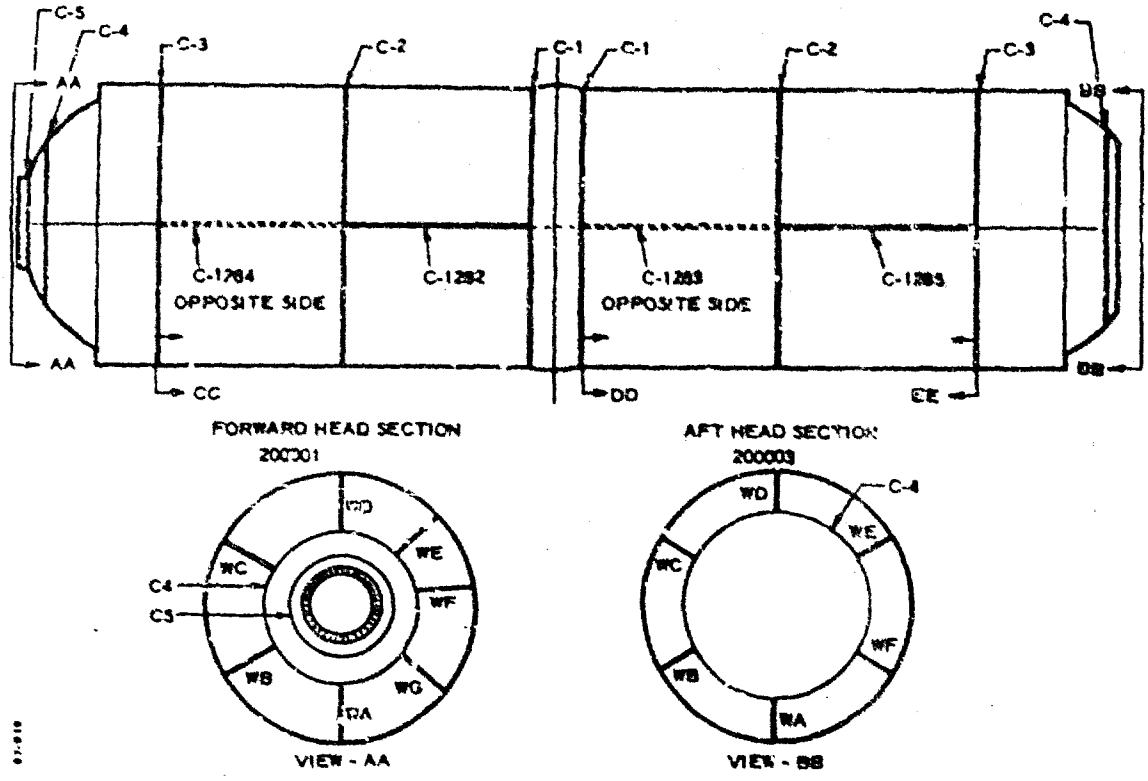

Figure 128 156-Inch Diameter Hydroburst Weld Identification

TABLE X

156-INCH DIAMETER HYDROBURST WELD IDENTIFICATION AND DEFECT LOCATION (All Ultrasonic Indications in Parent Metal Only Original Manufacturing Inspection)

Forward Head Section 200001

C-5	Igniter boss weld	See Figure 129
C-4	Forward dome weld	(No delaminations)
C-3	Dome to cylinder girth weld	See Figure 130
C-2	Center girth weld	(No delaminations)
C-1	Cylinder to joint forging	(No delaminations)
C-1284	Forward longitudinal weld	(No delaminations)
C-1282	Aft longitudinal weld	(No delaminations)

Aft Head Section 200003

C-1	Joint forging to cylinder weld	See Figure 131
C-2	Center girth weld	(No delaminations)
C-3	Cylinder to dome weld	See Figure 132
C-4	Nozzle adapter to dome weld	See Figure 133
C-1283	Forward longitudinal weld	(No delaminations)
C-1285	Aft longitudinal weld	(No delaminations)

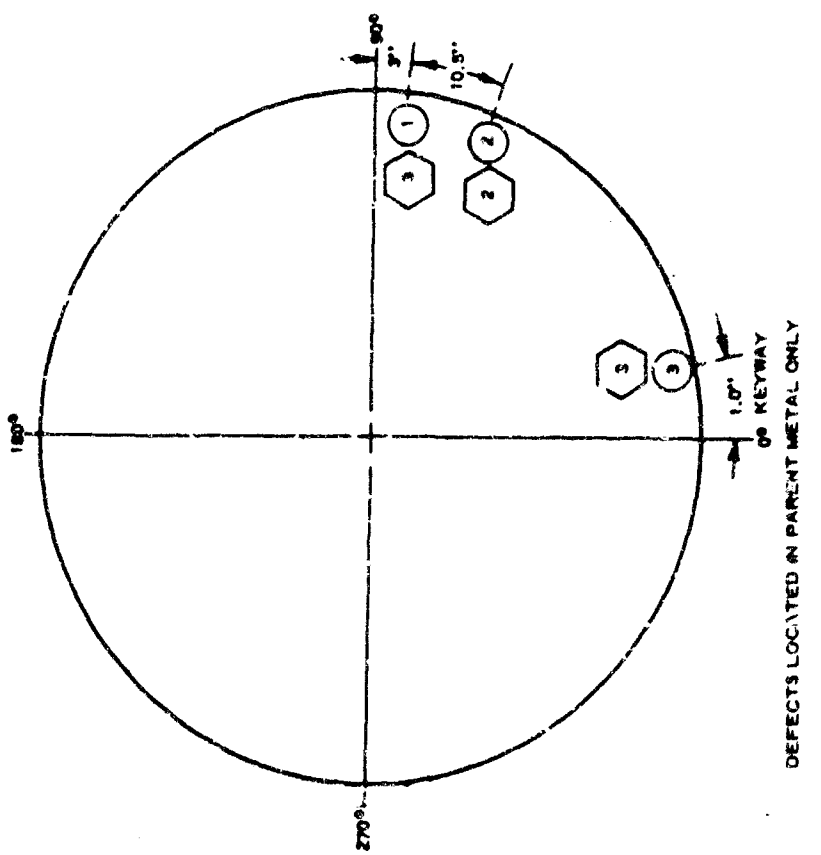

Figure 129 Forward Head Section, Weld C-5, Igniter Boss Weld, View AA

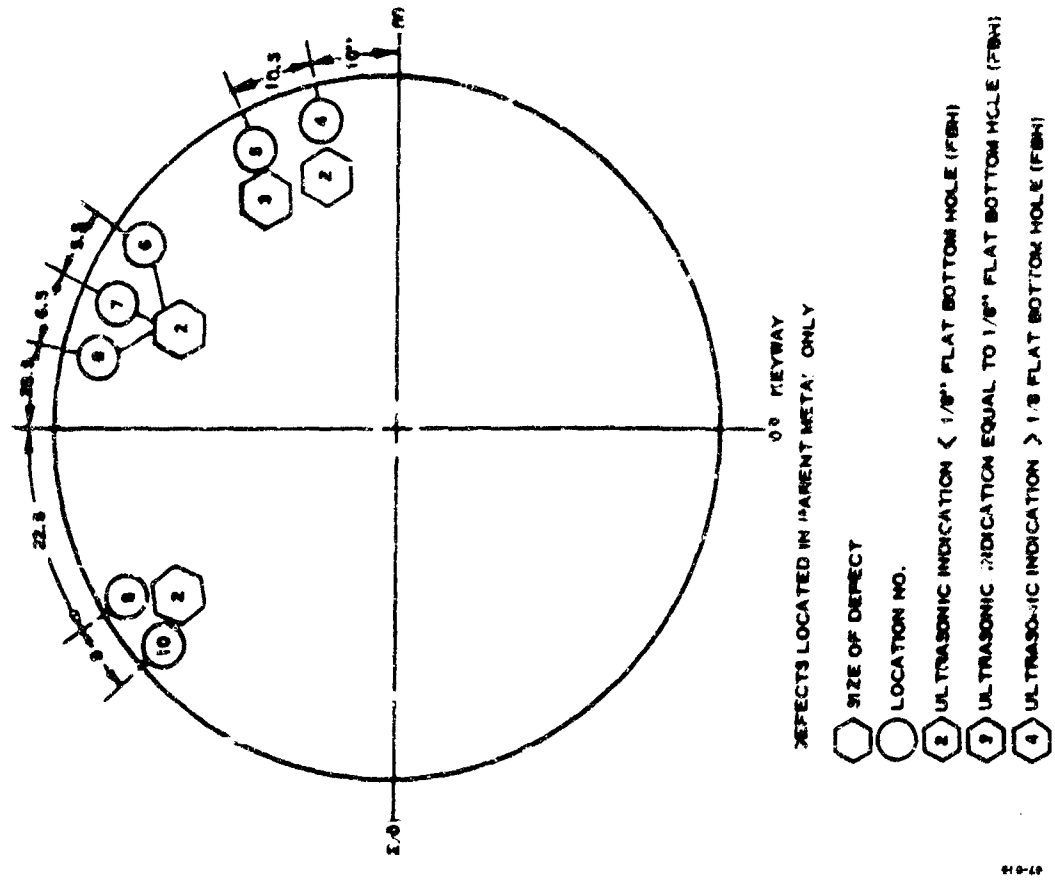

Figure 130 Forward Head Section, Weld C-3, Forward Girth Weld, View CC

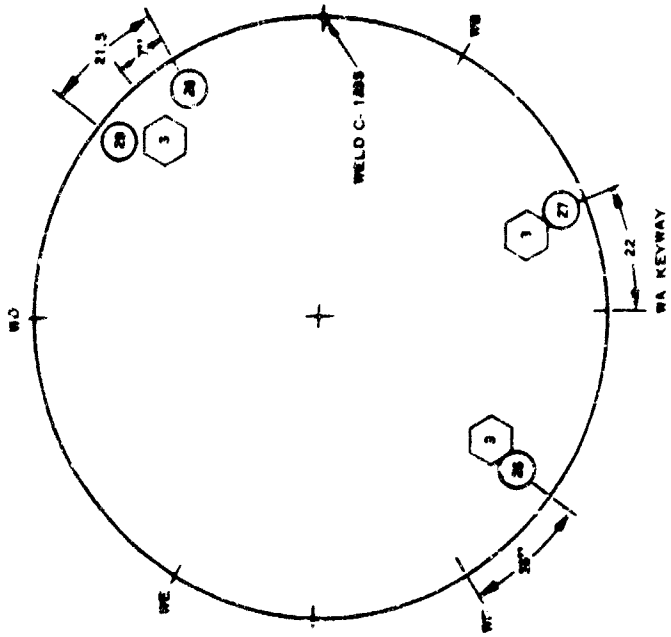

Figure 132 Aft Head Section, Weld C-3, Cylinder to Dome Weld, View EE

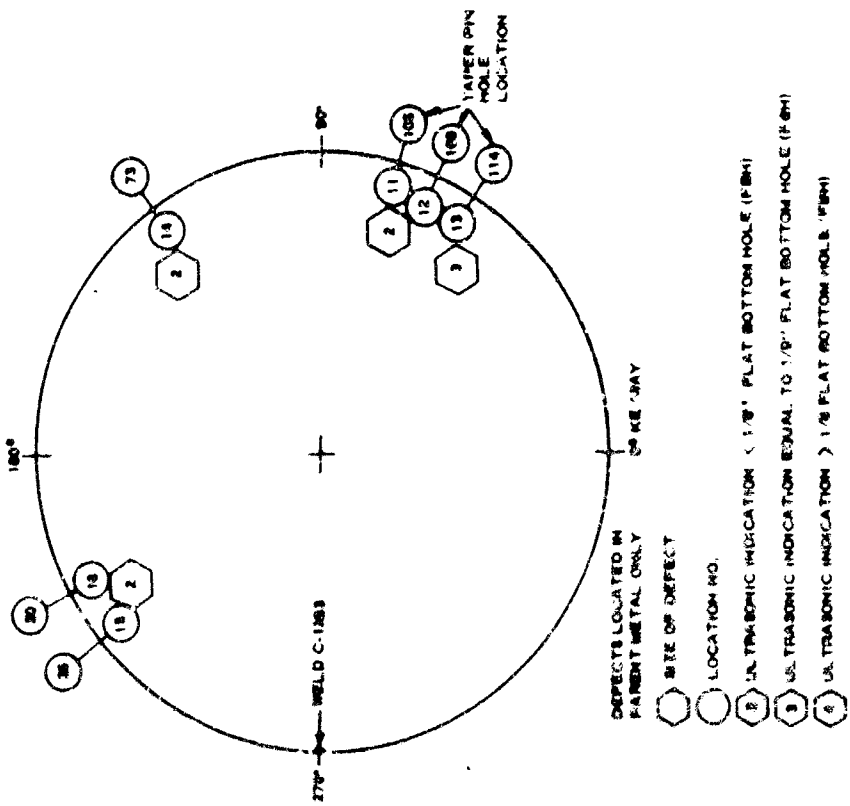

Figure 131 Aft Head Section, Weld C-1, Joint to Cylinder Section Weld, View DD

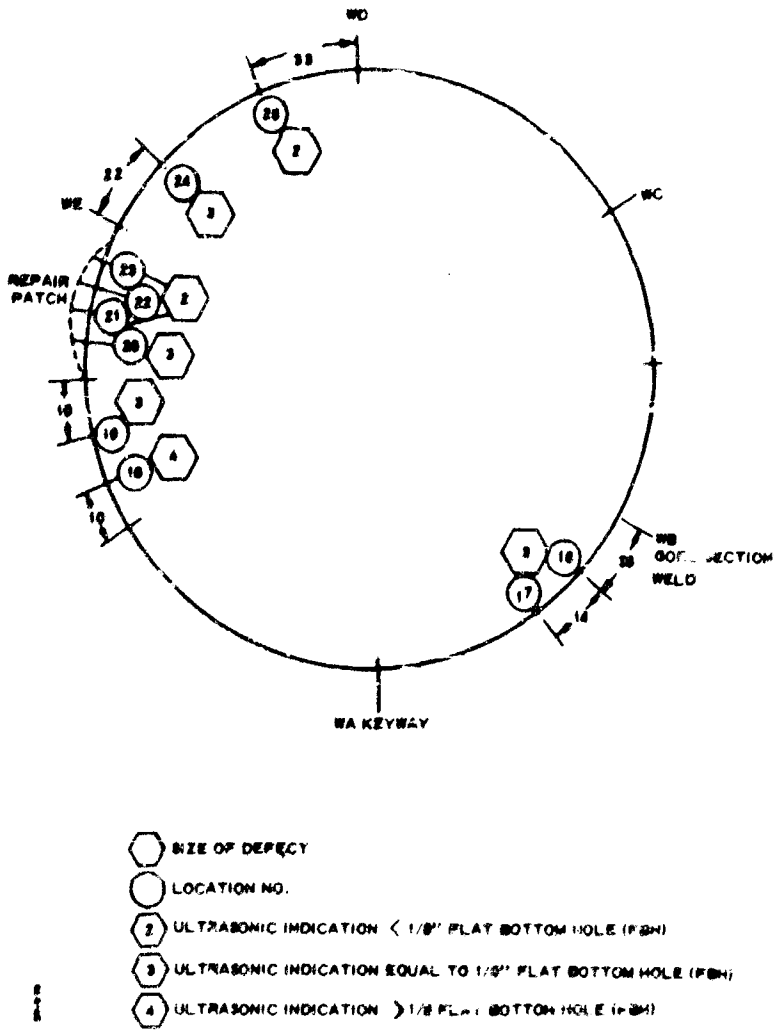

Figure 133 Aft Head Section, Weld C-4, Nozzle Adapter to Dome Weld, View BB

Initial inspection of the cleaned weld areas was with fluorescent dye penetrant. The penetrant, cleaner, and developer were applied from pressurized portable containers. The areas being inspected were recoated with penetrant at regular intervals to prevent loss of sensitivity due to drying and run-off. A 30-minute dwell-time was allowed for the penetrant. After cleaning and application of a liquid developer, the welds were inspected under ultraviolet illumination. No defects were detected by this method in the areas inspected.

The ultrasonic inspections were conducted with a Sperry model 721 reflectoscope using the 5N and 10N plug-in pulser-receiver units. Calibration of the transducers for beam angle was accomplished with a standard IIW-V-4 block. Signal response was calibrated to the shear wave reference standard described in LPC's Process Specification 207B (Ultrasonic Inspection of Fusion Welds). The calibration was performed for three notch areas

of 001, 002 and 004 square inches. Figure 134 illustrates the calibration plate removed from the case and subsequently elox-notched. The ultrasonic response from these notches is illustrated in Figure 135. The notch depth and length are tabulated below:

Notch Depth (in.)	Length (in.)	Designation
0.015	0.075	(half critical length)
0.020	0.100	(critical length)
0.030	0.150	(twice critical length)

Based on the work and conclusion of Strawley (Ref.) in connection with the failure investigation of Thiokol's 260-inch diameter hydroburst, the shear wave calibration and inspection methods may not have been adequate to detect either surface or subsurface zero-gap flaws (cracks); however, the dye penetrant means employed in the longitudinal weld inspections would have detected any existent surface flaws.

The shear wave transducers used were 2.25 MC frequency with shear angles of 45, 60 and 70 degrees. Transducers with crystal sizes of 1 by ½-inch, ½-inch square, and ¼-inch square were used. The shear wave inspection was mainly performed with the 1 by ½-inch size because of handling ease and resolution equivalent to the miniature and subminiature sizes. The 45 degree shear angle was used only to clarify indications from the 60 to 70 degree angle transducers.

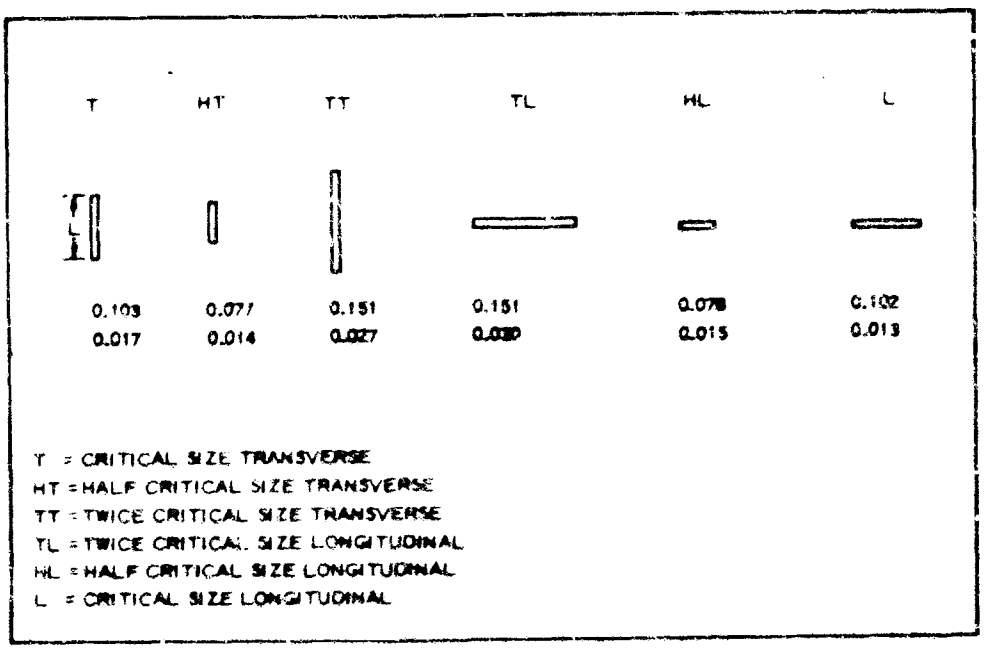

Figure 134 Ultrasonic Calibration, LPC Shear Wave Test Plate, 250 Grade Marage, 0.375 to 0.400-inch Thickness

2.25 MHZ TRANSDUCER
60° SHEAR ANGLE
1/2" X 1/2" CRYSTAL SIZE

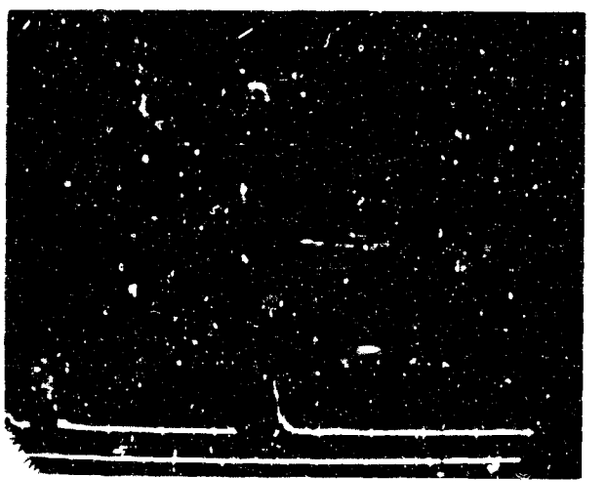

Shear Wave Calibration
Response to Notch (TL)

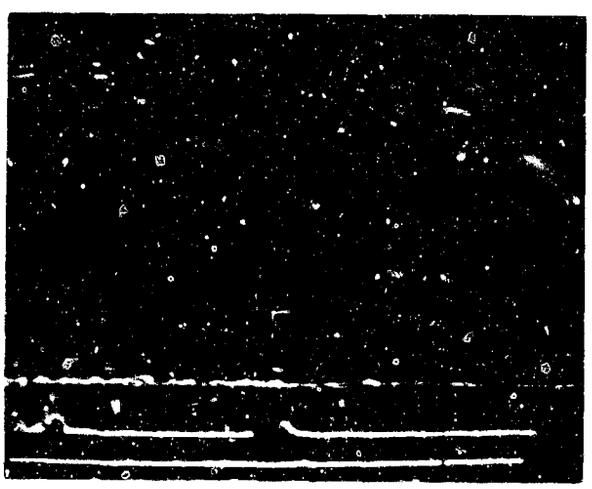

Shear Wave Calibration
Response to Notch (L)

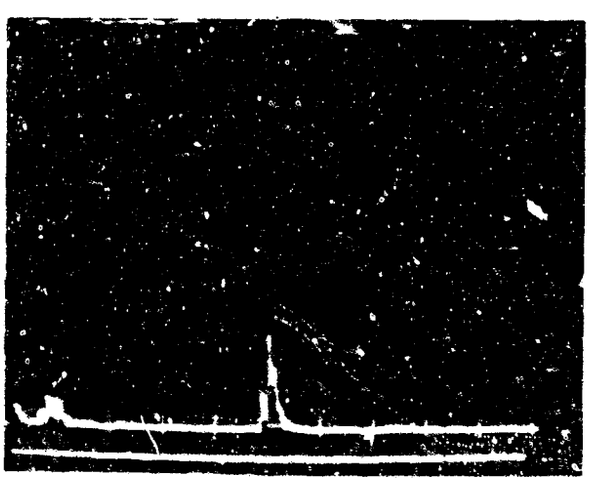

Shear Wave Calibration
Response to Notch (HL)

Figure 135 Ultrasonic Signal Indication from Shear Wave Calibration

The results of LPC's initial pre-hydroburst inspection of the aft head section are shown below:

Aft Head Section 200003

Plate adjacent to Weld C-1283

Girthweld C-1 is "O" station; all locations are aft of C-1. Defect areas are illustrated in Figure 136.

Defect Area	Station Location (in.)	
32	6 to 7.5	3 shear (S) indications 100% amplitude adjacent to weld bead/ detected from all approach angles.
33	22 to 24	Continuous indication (S) 80% amplitude/detectable from all approach angles.
34	32 to 35	Continuous indication (S) 80% amplitude/detectable from all approach angles.
35	74 to 91.5	Continuous indication (S) maximum signal amplitude at 6 inches from weld 60 degree S transducer at Station 90.

Plate adjacent to Weld C-1285

Girthweld C-2 is "O" station; all locations are aft of C-2.

Defect Area	Station Location (in.)	
27	9 to 26	Intermittent indication (S) 50 to 80% amplitude.
28	43.5 to 69.5	Intermittent indication (S) 40 to 80% amplitude.

b. Post-Hydroburst Inspection

After hydroburst, test plates were removed from the damaged aft-head section by carbon-arc cutting. The plates contained representative ultrasonic indications detected during the pre-hydroburst inspections. The areas from which the plates were removed and plate identification are shown in Figure 136. After removal of the plates from the case section they were solvent cleaned to remove the old liner and insulation materials so that additional ultrasonic testing could be accomplished from both sides of the plate.

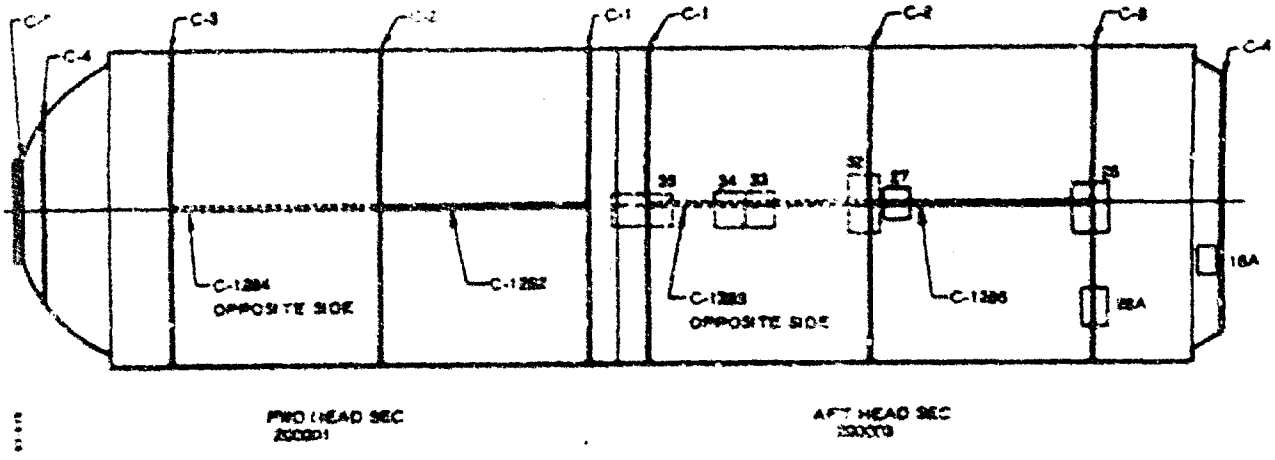

Figure 136 156-Inch Diameter Hydroburst Weld Identification and Test Plate Location (Post-Hydroburst)

A series of ultrasonic test methods were used on the cleaned plate to determine which method provided the best sensitivity. The methods used were:

(1) Pulse echo longitudinal wave immersion tests

(2) Transmit and receive longitudinal wave (twin transducers)

(3) Pulse echo longitudinal wave contact testing

(4) Shear wave contact testing

Method (1) above was discontinued after initial tests because of plate curvature. The curved plate required constant repositioning of the search tube to maintain the sound path perpendicular to the surface of the plate. Methods (2) and (3) were equally effective in detecting laminar flaws. If the laminar flaws had occurred near the surface of the plate, method (3) would not have been as sensitive as method (2). They were equal because all laminar defects detected were in the center of the plate. A miniature ($^1/_4$-inch diameter crystal) longitudinal contact transducer provided the best procedure for locating the boundaries of laminar defects.

Five types of indications were detected by ultrasonic inspection. These were:

(a) Three-inch long lack of fusion in plate No. 27, detected by shear waves; interpretation was verified by radiography.

(b) A single spot of porosity approximately 0.030-inch in diameter. The defect was found by shear waves and verified by radiography and longitudinal wave tests in plate No. 28A.

(c) A laminar defect detected by longitudinal wave testing not detected by shear waves. The areas were detectable by attenuation in reflected signal as well as positive indication from the transmitted signal. Typical indications were 18A-2 and 18A-4 through 18A-13.

(d) A condition as described in (c) but also detectable by shear waves from multiple directions of approach. When this condition was near the weld bead, the indication was assumed to be small, randomly scattered porosity not detectable by X-ray. When this condition was away from the weld zone, such as 18-3, no ultrasonic interpretation was reasonable. See Figure 137 for a typical signal response from this type defect.

(e) A false shear wave indication caused by the weld bead was not interpretable when the inside of the bead was obscured by case insulation. However, the weld bead indication was interpretable when both sides of the case were accessible.

The ultrasonic indications found were numbered as a dash number to the basic plate number, i.e., 18A-1 is defect No. 1, detected in plate 18A. For an explanation and location of the defects found by ultrasonic inspections of the two plates (18A and 28A) which were selected for a metallurgical investigation, see Tables XI and XII, and Figures 138 and 139, respectively.

The porosity was detected in the original X-rays made at the fabricator, but was passed as within specification. The lack of funsion was a rejectable defect and was not detected. A thin planar defect of this type often goes undetected with radiographic inspection due to the difficulty in locating the source exactly vertical to the weld-land surface. If the plane of the flaw is other than parallel to the beam center, its detectability is greatly reduced. The radiographs taken after the hardware was sectioned were made using a constant potential X-ray machine with extra-fine grain film. This procedure yielded sensitivity of better than 1%; typical minimum specification sensitivity is 2%.

c. Metallurgical Investigation

As previously indicated, 18 defective areas in the two selected plates were detected by ultrasonic inspection (defect 28A-6 which was identified as porosity was not utilized in the metallurgical investigation). Nine defective areas were retained to be investigated by LPC, and the remaining nine defective areas were sent to Mellon Institute for evaluation. The areas, marked in Figures 138 and 139, were sectioned and metallurgical evaluation was conducted as follows:

(1) Macroscopic Examination

Nine specimens were cut from the plate and examined with a binocular microscope at magnifications varying from 10 to 40X. All of the specimens, "as sectioned" or after removing 1/16 inch of material from one of the cut surfaces, disclosed the presence of delaminations located midway between the surfaces of the plate. Specimen No. 1, from plate 28A, fell into

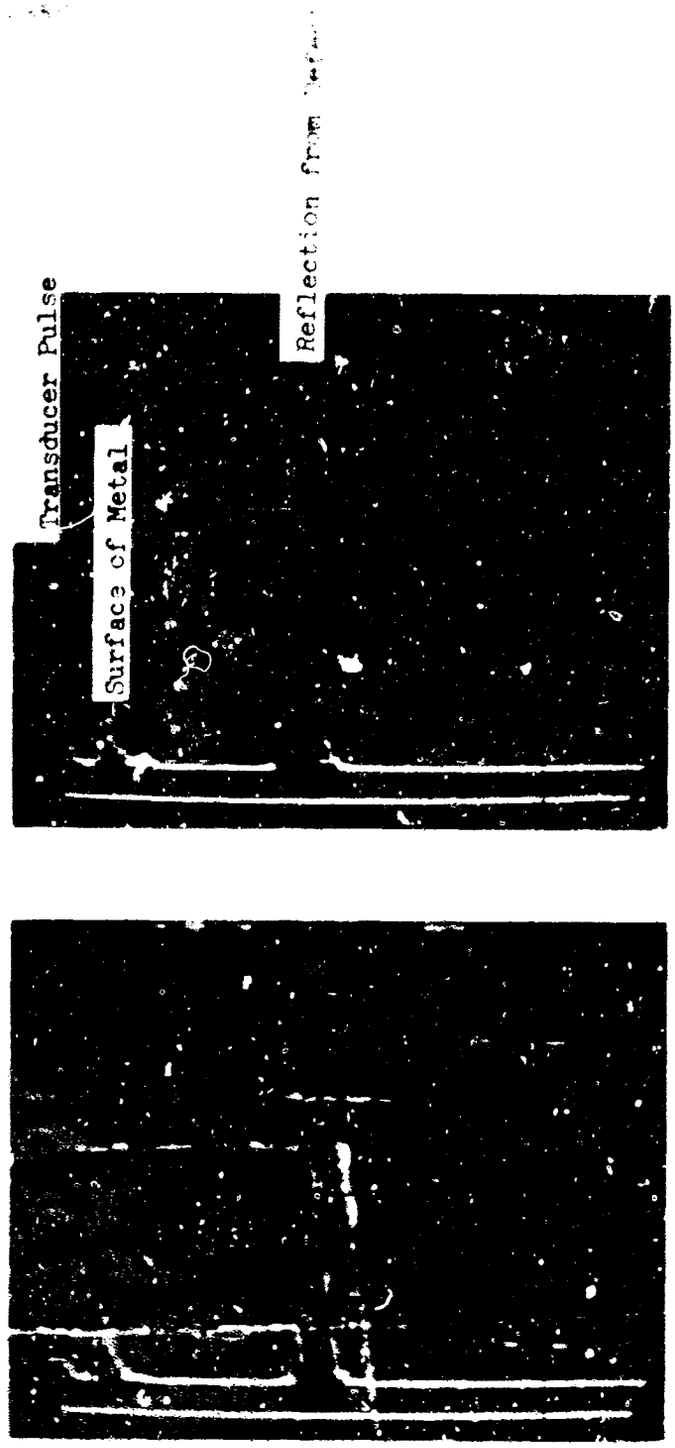

Top and bottom photos are
with transducer at 90° to weld Bottom photo
with transducer on the weld bead parallel to the bead.
2.25 mc transducer - ½ x ½" crystal
60° shear angle

Figure 1[illegible] Shear Wave Indication From 32-3

TABLE XI

ULTRASONIC TEST INDICATION FROM PLATE 18A

Post-Hydrotest

Plate No. 18A — Aft Head Section Weld C-4 (Nozzle Adapter to Dome Weld) All defects located in parent metal.

Indication No.	
18A-1	Shear wave indication greater than TL notch (0.003 in.^{2}) Detectable from multiple directions Longitudinal indication >0.100 FBH 0.2-in. below surface
18A-2	Longitudinal indication >0.100 FBH 0.2-in. below surface
18A-3	Shear wave indication greater than TL notch (0.003 in.^{2})
18A-4	Longitudinal indication >0.100 FBH -0.2-in. below surface
18A-5	Longitudinal indication >0.100 FBH -0.2-in. below surface
18A-6	Longitudinal indication <0.100 >0.040 FBH -0.2-in. below surface
18A-7	Longitudinal indication <0.100 >0.040 FBH -0.2-in. below surface
18A-8	Longitudinal indication >0.100 FBH -0.2-in. below surface
18A-9	Longitudinal indication >0.100 FBH -0.2-in. below surface
18A-10	Longitudinal indication >0.100 FBH -0.2-in. below surface
18A-11	Longitudinal indication <0.100 >0.040 FBH 0.2-in. below surface
18A-12	Longitudinal indication <0.100 >0.040 FBH 0.2-in. below surface
18A-13	Longitudinal indication <0.100 >0.040 FBH 0.2-in. below surface

The term > and <0.100 flat bottom hole (FBH) refers to amplitude of the reflected signal and has no reference to size of area over which the signal amplitude was obtained. For size and location see photo of Plate 18A.

TABLE XII

ULTRASONIC TEST INDICATIONS FROM PLATE 28A, AFT HEAD SECTION WELD C-3

Indication No.	
28A-1	A 2-in. long indication adjacent to weld bead. A continuous shear wave indication detectable from multiple approach directions. 100% signal amplitude. Detectable by longitudinal wave signal amplitude >0.100 FBH. Negative radiographic indications.
28A-2	A shear wave indication >100% amplitude detectable from multiple approaches. A longitudinal wave indication >0.100 FBH. Area is 2 inches from weld.
28A-3	Same as 28A-2 except 3 inches from weld.
28A-4	Same as 28A-2 except smaller in area.
28A-5	A ¾-in. square indication adjacent to weld area. Shear wave indication of 50% amplitude detectable through 180° arc. Detected by longitudinal wave signal amplitude <0.100 FBH. Negative radiographic indication.
28A-6	A single spot of porosity in weld bead. Detected by shear longitudinal waves. Verified by radiography.

The term > and <0.100 flat bottom hole (FBH) refers to amplitude of the reflected signal and has no reference to size of area over which the signal amplitude was obtained. For size and location see photo of Plate 18A (Figure VII-11).

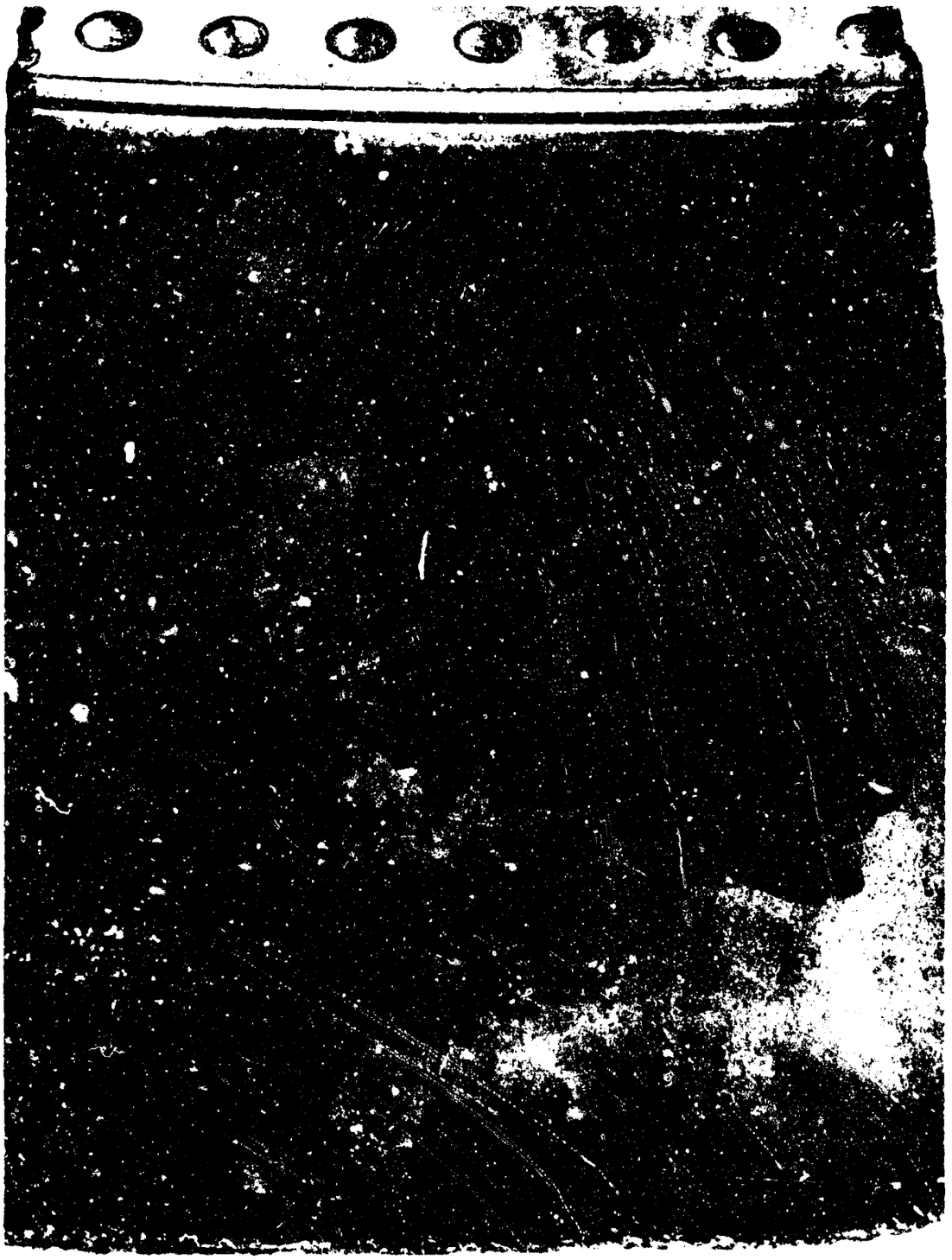

Figure 138 Aft Section Plate Weld C-4 (Plate 18A)

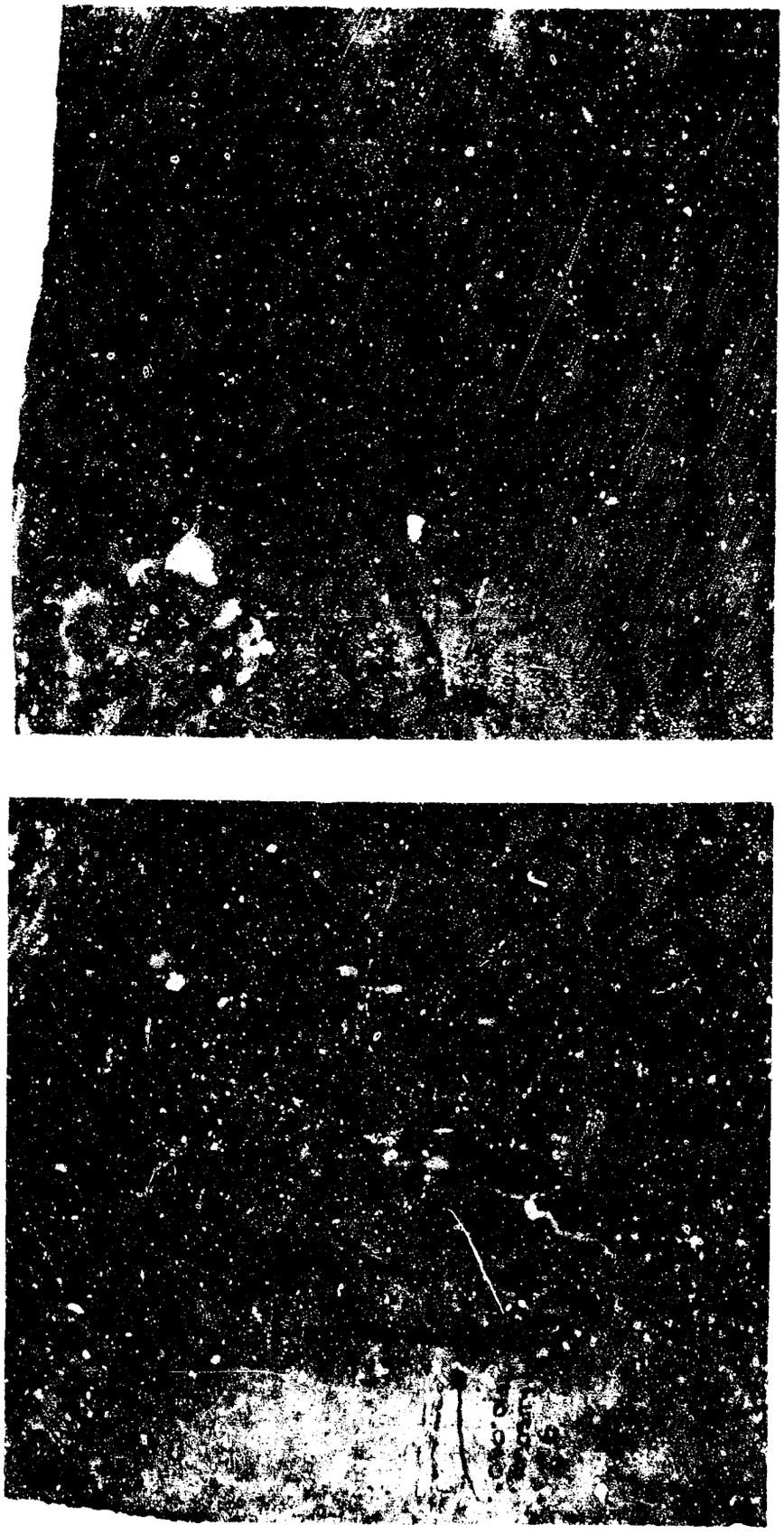

Figure 139 Aft Segment Plate 28A Containing Girth Weld C-3

two pieces when it was cut from the plate. Therefore, the size of the delamination found in this specimen was larger than the area sectioned ($^5/_{16}$ by 2 inches). The face of the delamination exhibited discoloration which was caused by oxidation. The length of the delaminations found in the nine specimens evaluated by LPC are presented in Table XIII.

Figures 140 and 141 are photographs of the delaminations exhibited by specimens Nos. 28A-2 and 18A-13. These photographs are typical of the delaminations found in all the specimens.

(2) Microscopic Examination

Examination of the unetched microstructures revealed that all of the delaminations were associated with areas exhibiting numerous inclusions in the form of titanium carbonitrides and oxides. Figures 142 through 149 are photomicrographs of the delaminations exhibited by the specimens. Etching of the specimens disclosed the delaminations occurred in segregated bands of retained austenite. This banding is illustrated in Figure 150. Figure 148 also reveals the presence of a smaller delamination running parallel with the large delaminations

(3) Discussion

The defects revealed by this investigation are delaminations. The delaminations were caused by segregation and inclusions in the form of complex titanium carbonitrides, oxides and retained austenite. This segregation and increased inclusion content (beyond rating on the ASTM charts) occurred upon solidification of the ingot. The austenite, as illustrated in Figure 142, was stabilized by a localized increase in the percentage of austenitizers such as nickel in the last low-melting liquid to freeze in the ingot. Subsequent homogenization treatments and hot working in plate rolling failed to break up this segregation.

The delaminated surface of specimen No. 1, from Section 8, revealed the presence of discoloration caused by oxidation. This indicates the delamination was open to the adjacent weld (C-3). The presence of these types of delaminations would be only slightly detrimental to the tensile strength for stresses applied parallel to the delaminations.

By comparing the size of the defects reported by ultrasonic inspection (Tables XI and XII) and the size of the defects measured after sectioning (Table XIII), one can see that an excellent correlation exists between the two sets of data. This reveals that the ultrasonic techniques utilized to find and measure the delaminations are extremely reliable.

d. Mellon Institute Report

(1) Introduction

This report presents the results of the inspection conducted on the six samples of air-melt maraging steel plate recovered from the 156-inch diameter Lockheed Propulsion Company hydroburst booster case. Attempts

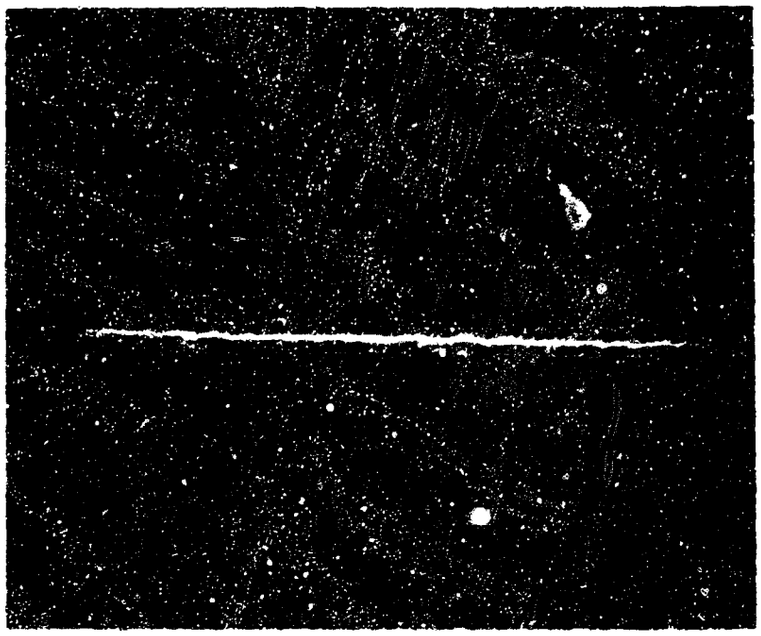

Figure 140 Photograph of Defect No. 13 Illustrating the Delaminations Found in Plate 28A. The Thick White Line is the Delamination and the Thin White Lines are Segregated Stringers of Titanium Carbonitrides.

Mag. 12X

Figure 141 Photograph of Defect No. 2 Illustrating the Delaminations Found in Plate 18A. The Thick White Line is the Delamination and the Thin White Lines are Segregated Stringers of Titanium Carbonitrides.

120X

Figure 142 Photomicrograph of Delamination Exhibited by Defect No. 2 Located in Plate 28A

Figure 143 Photomicrograph of Delamination Exhibited by Defect No. 3 Located in Plate 28A

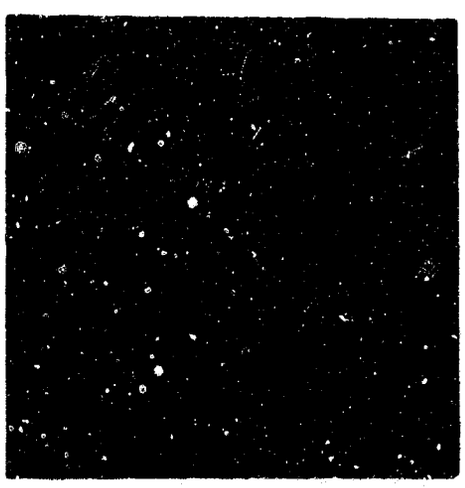

Figure 144 Photomicrograph of Delamination Exhibited by Defect No. 4 Located in Plate 28A

Figure 145 Photomicrograph of Delamination Exhibited by Defect No. 5 Located in Plate 28A

260X

Figure 146 Photomicrograph of a Small Delamination Exhibited by Defect No. 10 Located in Plate 18A

120X

Figure 147 Photomicrograph of Delamination Exhibited by Defect No. 11 Located in Plate 18A

120X

Figure 148 Photomicrograph of Delamination Exhibited by Defect No. 12 Located in Plate 18A

120X

Figure 149 Photomicrograph of Delamination Exhibited by Defect No. 13 Located in Plate 18A

MAGNIFICATION: 150X Etchant: Marbles Reagent

Figure 150 Photomicrograph of Defect No. 12 Located in Plate 18A.

NOTE: The white structure associated with the delaminations is retained austenite. The darker structure is the normal structure for hardened maraging steel.

TABLE XIII

SIZE OF DELAMINATIONS

Specimen No.	Plate Section 28A	Plate Section 18A
1	5/16 wide by 32-in. long*	
2	5/16 wide by 17/64-in. long	
3	5/16 wide by 27/64-in. long	
4	5/16 wide by 3/64-in. long	
5	5/16 wide by 5/64-in. long	
10		5/64-in. long
11		3/64-in. long
12		1/8-in. long
13		5/64-in. long

* The only specimen that split apart.

were made to correlate non-destructive testing results with the defects and uncover information as to the cause of the defects.

(2) Experimental

(a) Material

The markings on the sample surfaces chart the suspected positions of defects in the samples, as determined by ultrasonic detection techniques at LPC. A total of nine defects were charted.

(b) Procedure

All six samples were recharted at Mellon Institute using a Branson Sonoray ultrasonic defect search unit. Oscillograph displays for each of the defects were photographed. The samples were then sectioned in a manner to most rapidly reveal the presence of defects. Dye-penetrant checking techniques were used frequently during the search period.

(3) Results

The results of the inspection of the six maraging steel samples are summarized in Table XIV. The table shows that eight of the nine charted defects were found. These defects were in all cases thin cracks, generally located in one plane parallel to the sample surfaces and approximately mid-way between them. The defect lengths* were measured

* One of the three crack dimensions, referred to here as the length simply for convenience.

TABLE XIV

DESCRIPTION OF THE RESULTS OF THE DEFECT SEARCH

Sample Number	Defect Found	Defect Not Found	Defect Type[1]	Defect Depth[2] (in.)	Defect Position[3]	Defect Length[4] (in.)	Defect Breadth[5] (in.)
1	X		Planar Crack	0.21	HAZ	0.50	0.20
2		X	------	---	---	---	---
3A	X		Planar Crack	0.18	HAZ	0.88	0.20
3B	X		Planar Crack	0.18	PM	0.66	0.40
3C		X	------	---	---	---	---
(3) Total	X		------	---	---	---	0.60
4	X		Planar Crack	0.18	PM	0.13	0.14
5	X		Planar Crack	0.17	HAZ	0.18	0.36
6	X		Planar Crack	0.18	HAZ	0.05	---
7	X		Planar Crack	0.18	HAZ	0.12	0.25
8	X		Planar Crack	0.17	PM	0.10	0.20
9	X		Planar Crack	0.17	PM	0.10	0.15

[1] Defects were all narrow cracks, generally uni-planar and parallel to the as-received sample surfaces.
[2] Gives the approximate distance from the closest surface to the plane of cracking.
[3] HAZ - heat affected zone; PM - parent metal
[4] Gives the length of the crack visible to the unaided eye. In all cases, there are hair-line crack extensions visible only at high magnification.
[5] Gives the approximate size of the third dimension of the crack.

on the face of the polished metallographic sample which, in most cases, represents the broadest portion of the crack. The measurement given is the length of the crack visible on the sample to the unaided eye. Microscopic examination reveals very thin crack extensions beyond the main crack, but these are difficult to measure since, in addition to their thinness, they are often discontinuous.

The breadth of the crack was determined by sectioning perpendicular to the crack length at its widest opening and measuring the depth of penetration in this direction. Losses incurred during sectioning were also accounted for.

The position of the crack relative to the entire sample was determined by an examination of the etched sample. In specimens with dual structures (weld metal and parent metal) this task was straightforward. However, in specimens of a continuous structure, particular attention was given to the rates and evenness of etching. Thus, it is possible in most cases to make a fair judgement as to whether the major cracking is in the parent metal or in a heat-affected zone of the parent metal. A truly valid judgement on this point can only be made from a knowledge of the positions in the case from which the samples were obtained.

Figures 151 through 165 present sketches, oscillograph displays, and photomicrographs showing the qualitative results of the inspection. Figures 151, 153, 158, 160, and 163 are "lead-off" pages to each one of the five samples in which defects were found of the total of six received at Mellon Institute. These figures include (a) sketches of the as-received samples and the manner in which they were sectioned (dotted lines), (b) sketches of the resulting metallographic samples, (c) oscillograph displays of the charted defects, and (d) a photomicrograph of the "most open" portion of the crack.

Following each of these above listed figures are additional photomicrographs showing the condition of the sample in the area of cracking. These photomicrographs are of (1) low and (2) high magnification to reveal the noted association of the cracks with (1) the segregation phenomenon known as banding and (2) stringers of secondary phase particles.

(4) Conclusions

A 90 percent correlation between ultrasonic inspection at Mellon Institute and defect discovery was experienced.

All defects were thin delaminations generally located in one plane which was parallel to the sample surfaces and located approximately equidistant from them.

All delaminations examined were associated with a banded microstructure and stringers of secondary phase particles.

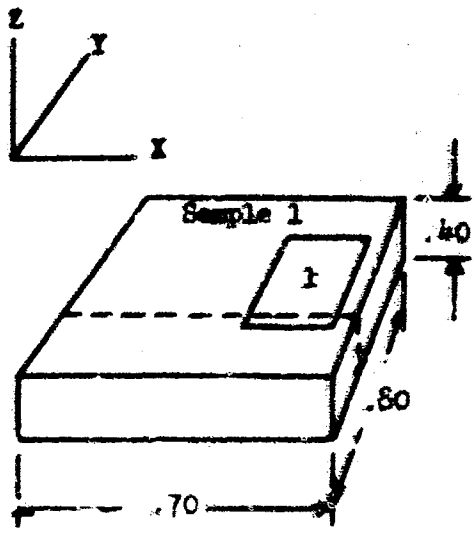

(a)

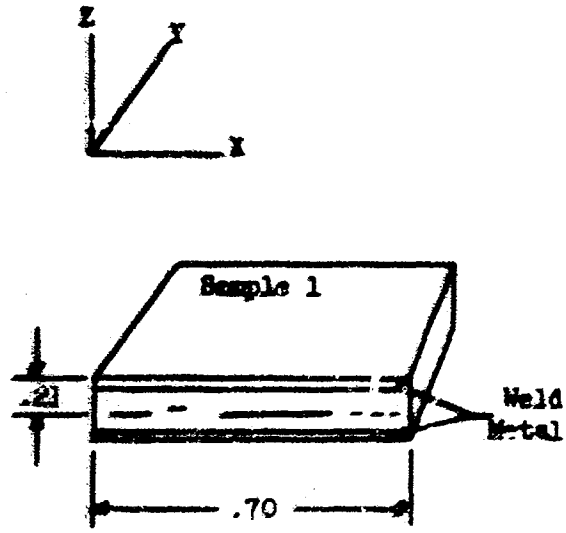

(b)

(c)

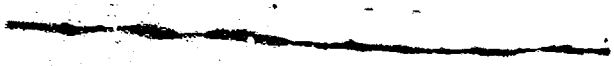

100X (d)

Figure 151 "Lead-Off" Page for Sample 1 Showing (a) a Sketch of the Sample, (b) a Sketch of the Sectioned Metallographic Specimens, (c) an Oscillograph Display of the Defect, and (d) a Photomicrograph of the "Most Open" Portion of the Crack.

100X Etch: Mixed Acid

(a)

500X Etch: None

(b)

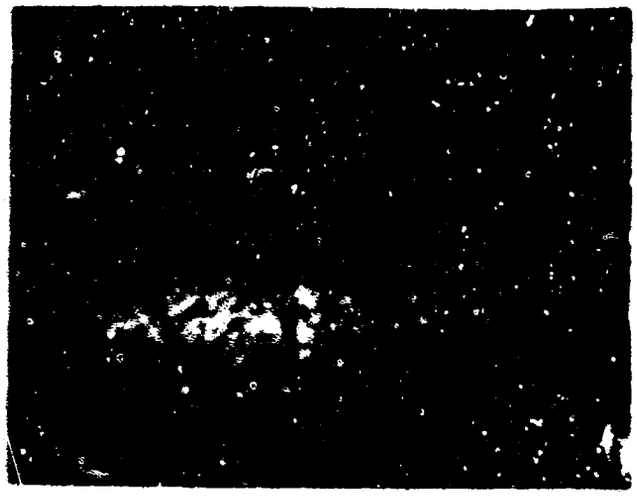

500X Etch: Mixed Acid

(c)

Figure 152 Photomicrographs Showing the Association of the Cracks with the Banding (a) and the Stringers of Secondary Phase Particles, (b) and (c) in Sample 1.

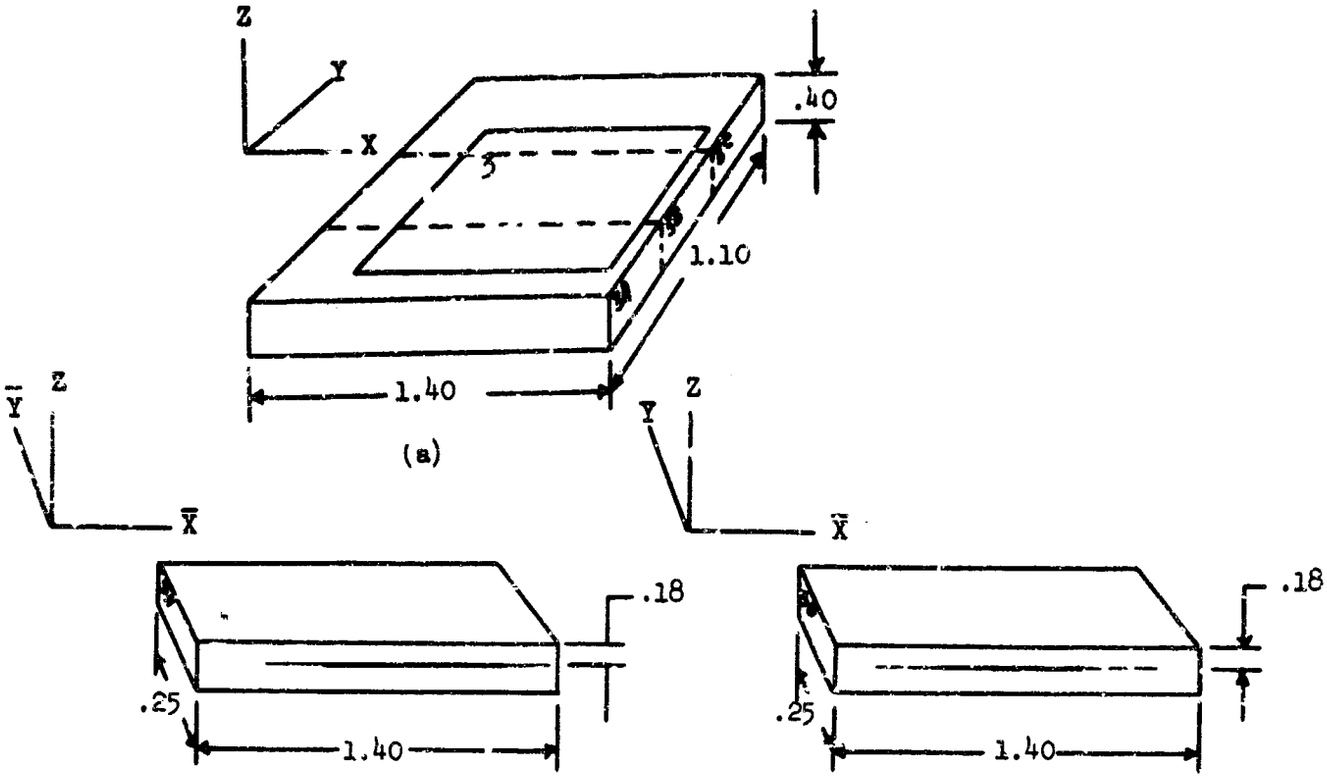

(c)

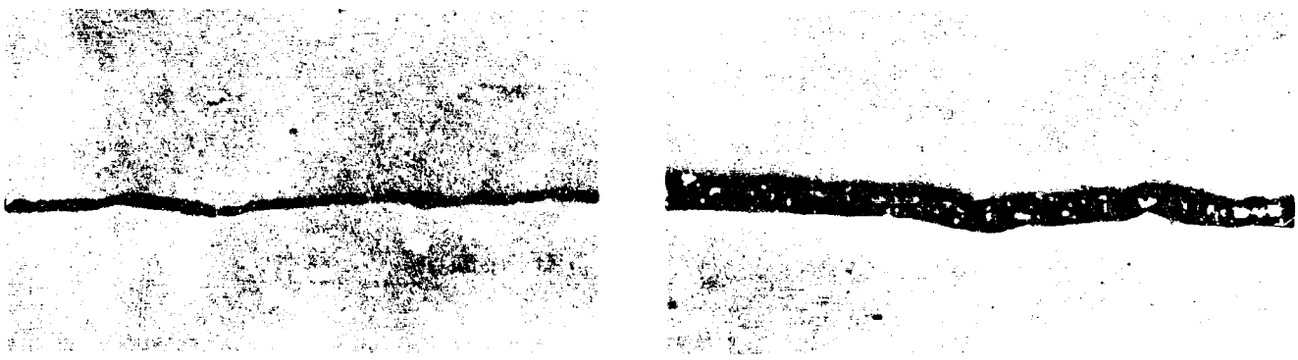

100X 100X

(d)

Figure 153 "Lead-Off" Page for Sample 3 Showing (a) a Sketch of the Sample, (b) Sketches of the Section Metallographic Specimens, (c) an Oscillograph Display of the Defect, and (d) Photomicrographs of the "Most Open" Portion of the Cracks in Specimens 3A and 3B, Respectively

500 X Etch: None

(a)

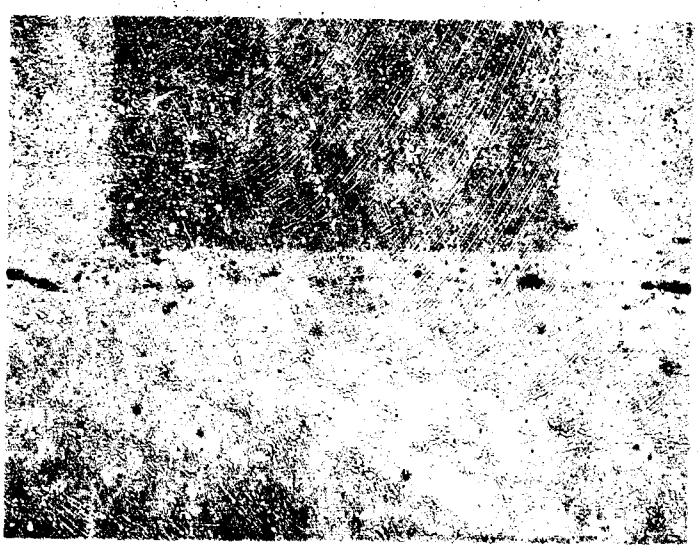

500 X Etch: None

(b)

Figure 154 Photomicrographs Showing the Association of the Cracks with Stringers of Secondary Phase Particles in (a) Sample 3A and (b) Sample 3B.

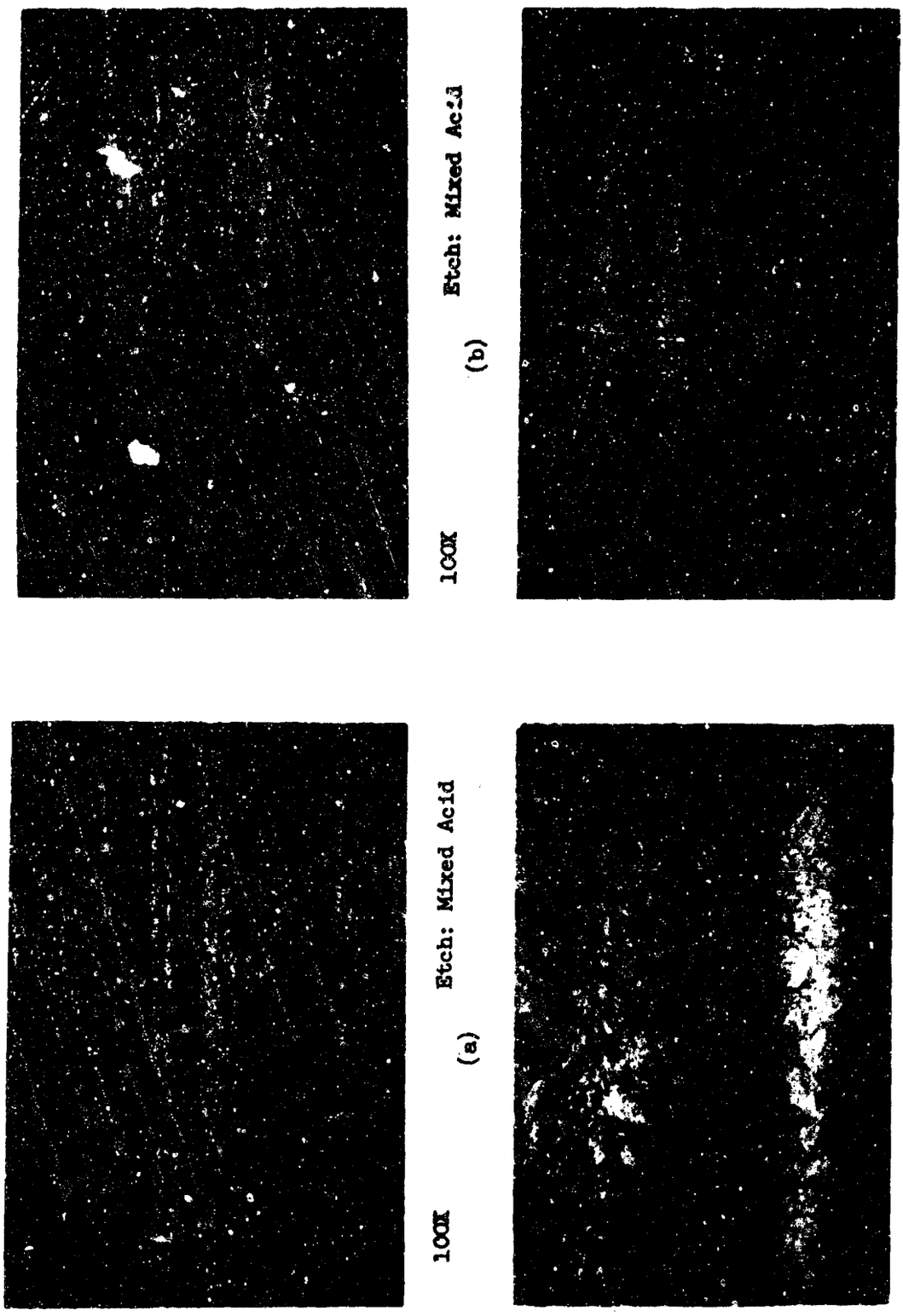

100X Etch: Mixed Acid (a)

100X Etch: Mixed Acid (b)

500X Etch: Mixed Acid (c)

500X Etch: Mixed Acid (d)

Figure 155 Photomicrographs Showing the Association of the Cracks with (a) and (b) Banding and (c) and (d) Stringers of Secondary Phase Particles in Sample 3A

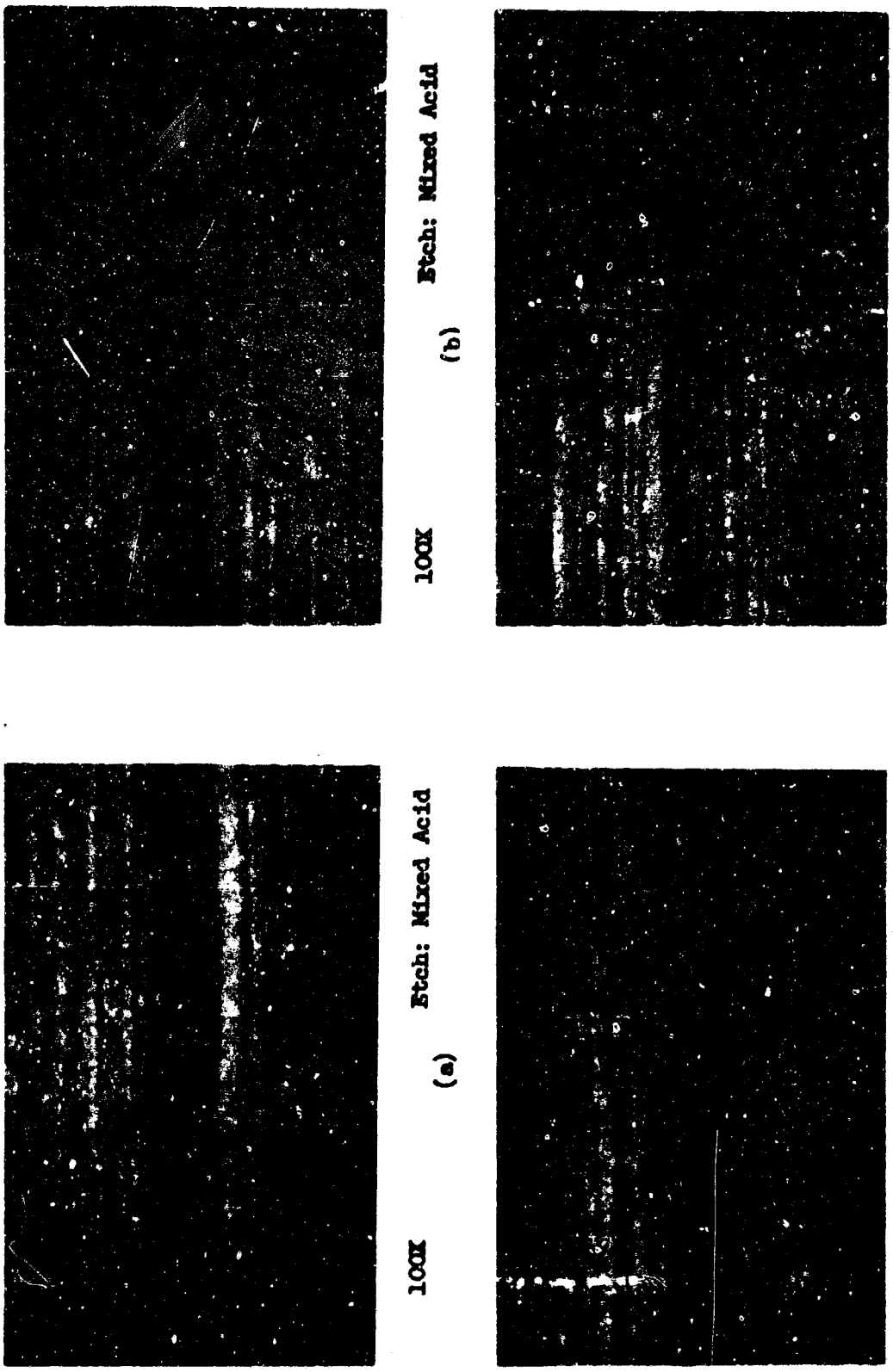

100X Etch: Mixed Acid (a)

100X Etch: Mixed Acid (b)

100X Etch: Mixed Acid (c)

100X Etch: Mixed Acid (d)

Figure 156 Photomicrographs Showing the Association of the Cracks with Banding in Sample 3B

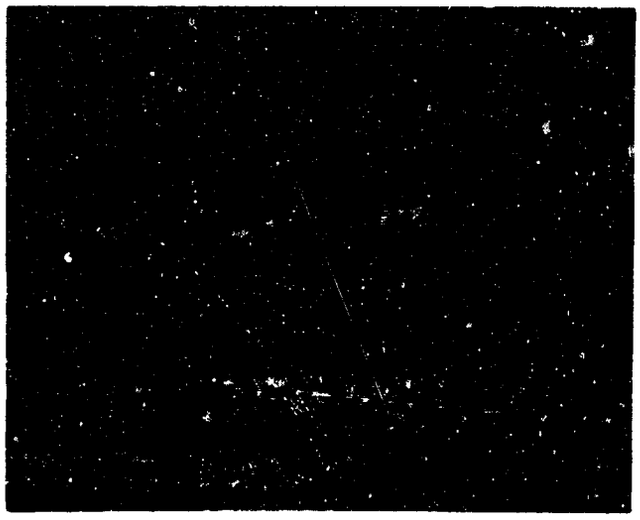

250X Etch: Mixed Acid

(a)

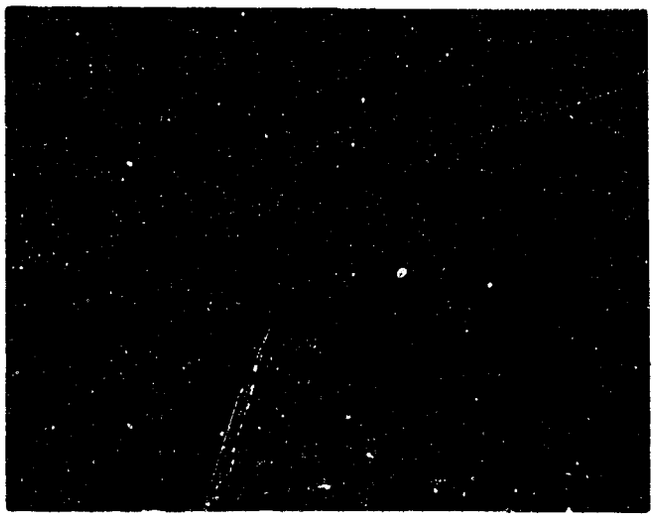

250X Etch: Mixed Acid

(b)

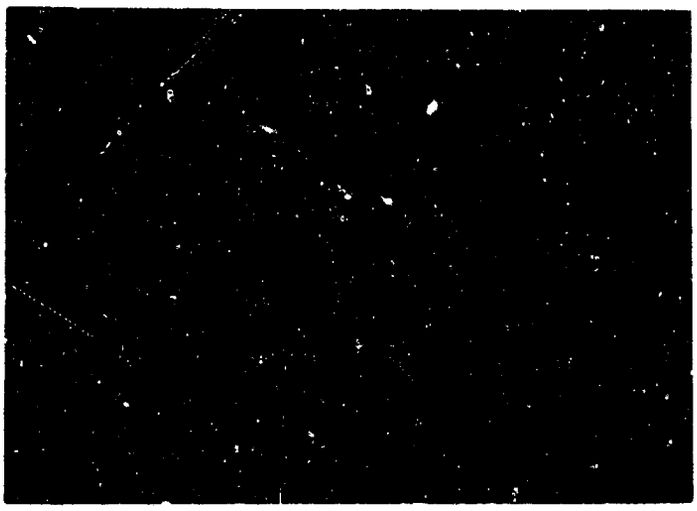

500X Etch: Mixed Acid

(c)

Figure 157 Photomicrographs Showing the Association of the Cracks with Stringers of Secondary Phase Particles in Sample 3B

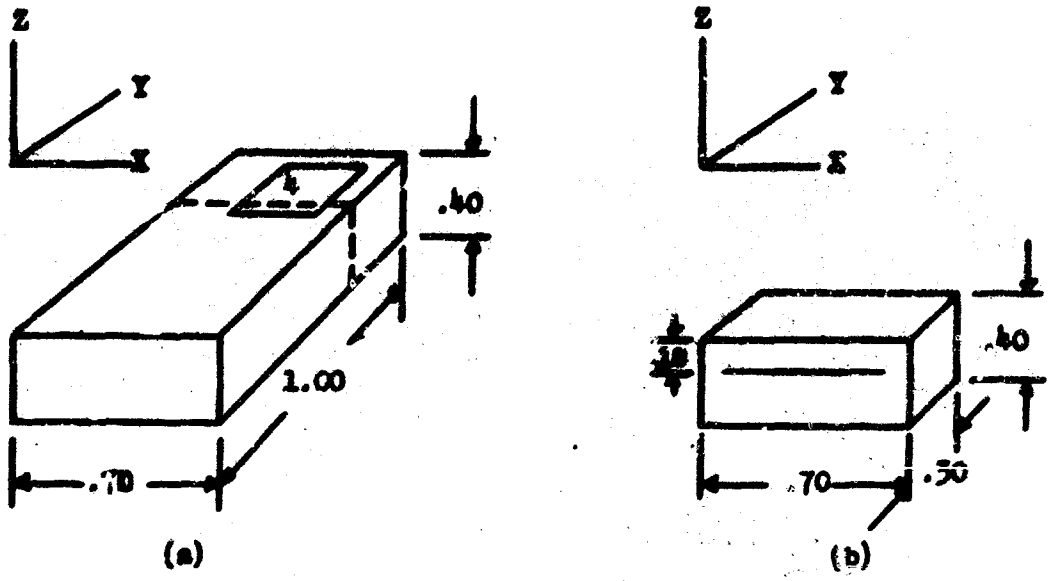

(a) (b)

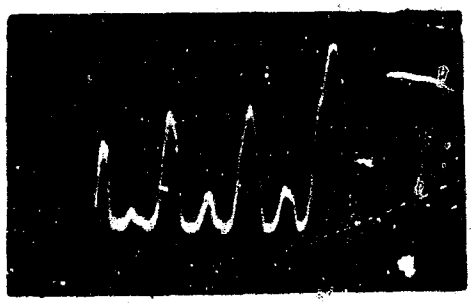

(c)

100X Etch: None

(d)

Figure 158 "Lead-Off" Page for Sample 4 Showing (a) a Sketch of the Sample, (b) a Sketch of the Sectioned Metallographic Specimen, (c) an Oscillograph Display of the Defect, and (d) a Photomicrograph of the "Most Open" Portion of the Crack

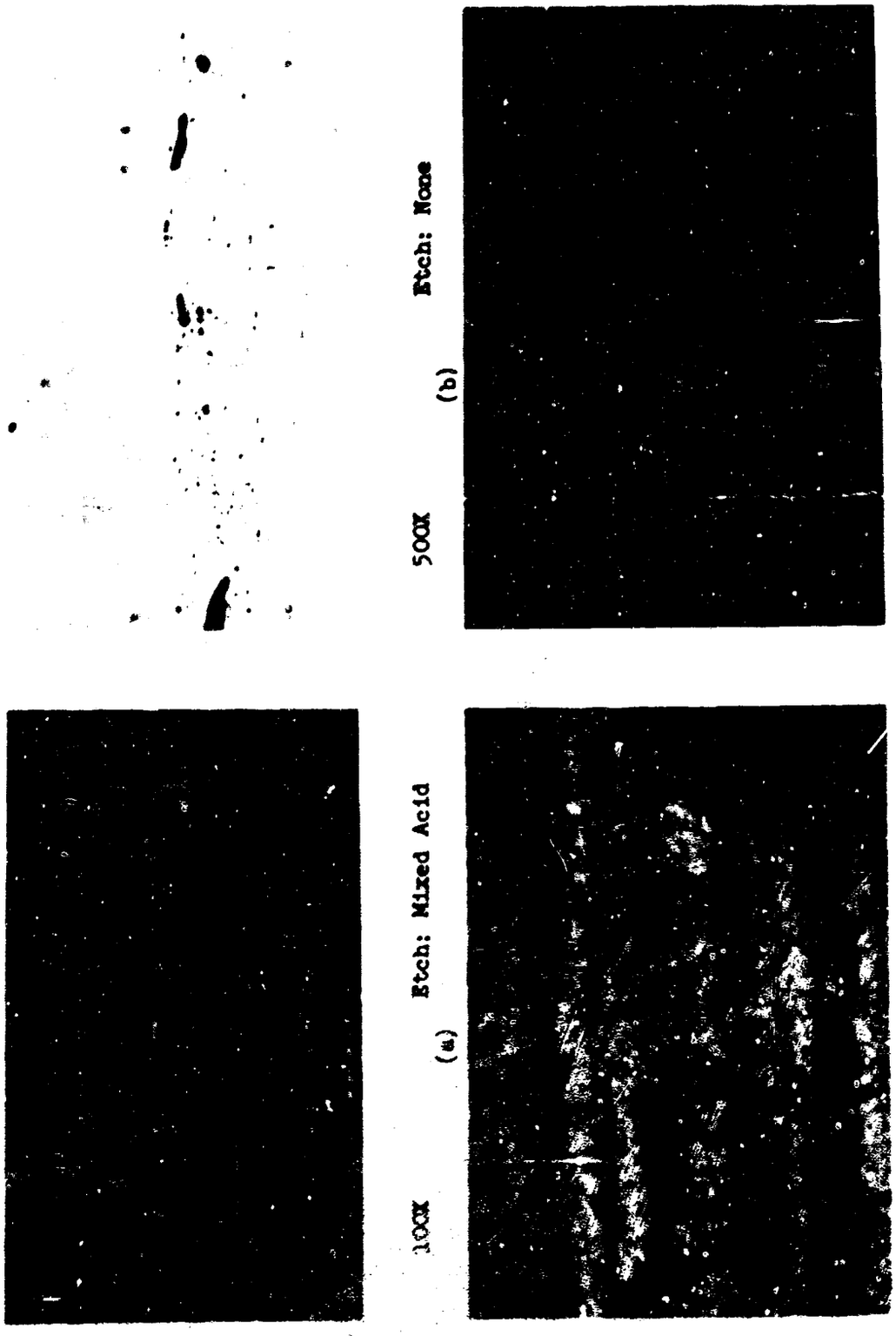

100X (a) Etch: Mixed Acid

500X (b) Etch: None

500X (c) Etch: Mixed Acid

500X (d) Etch: Mixed Acid

Figure 159 Photomicrograph Showing the Association of the Cracks with Banding (a) and Stringers of Secondary Phase Particles (b), (c) and (d) in Sample 4

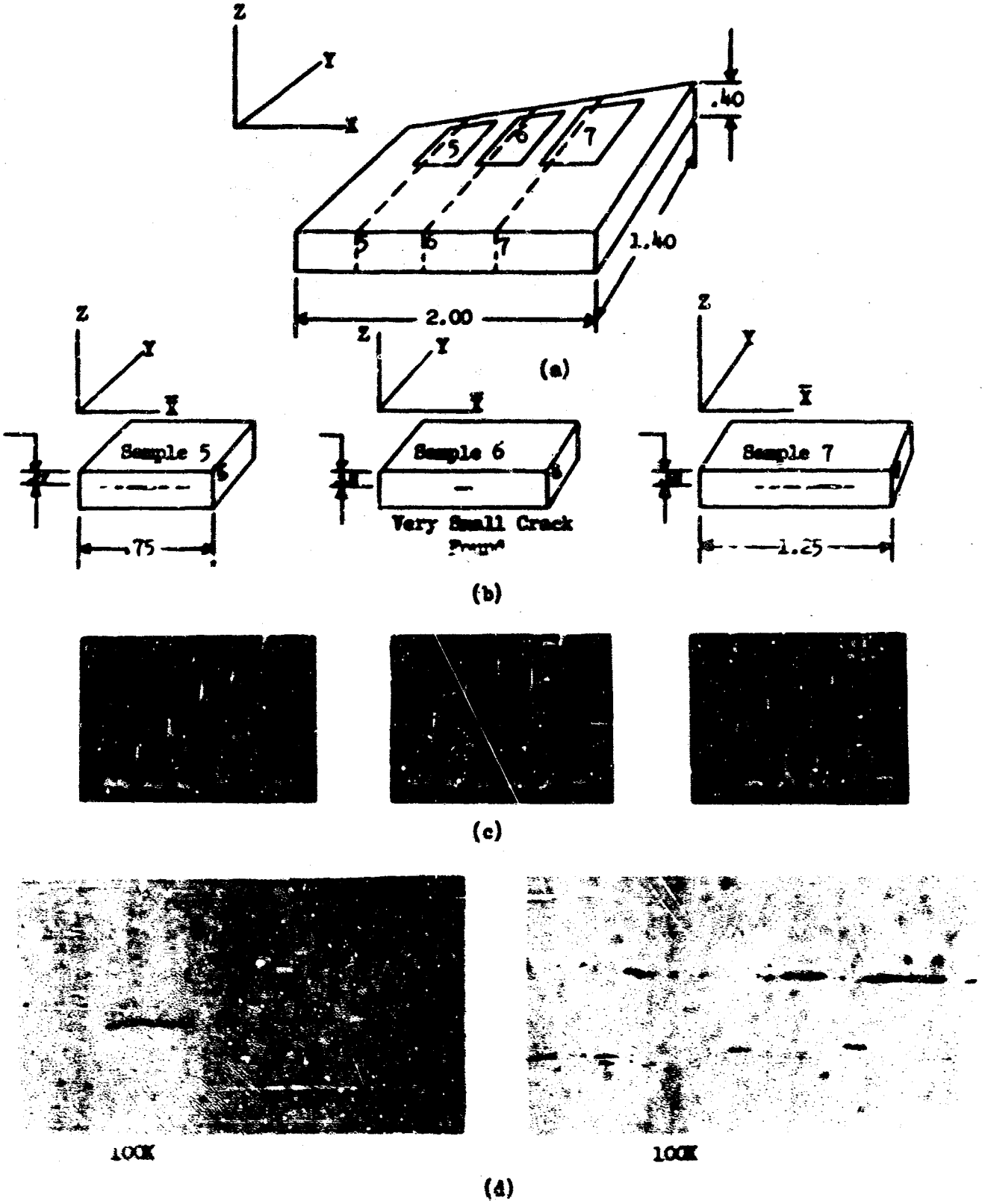

Figure 160 "Lead-Off" Page for Combination Sample 5, 6 and 7 Showing (a) a Sketch of the Sample, (b) Sketches of the Corresponding Metallographic Specimens, (c) an Oscillograph Display of the Defects, and (d) Photomicrographs of the "Most Open" Portion of the Cracks in Specimens 5 and 7, Respectively

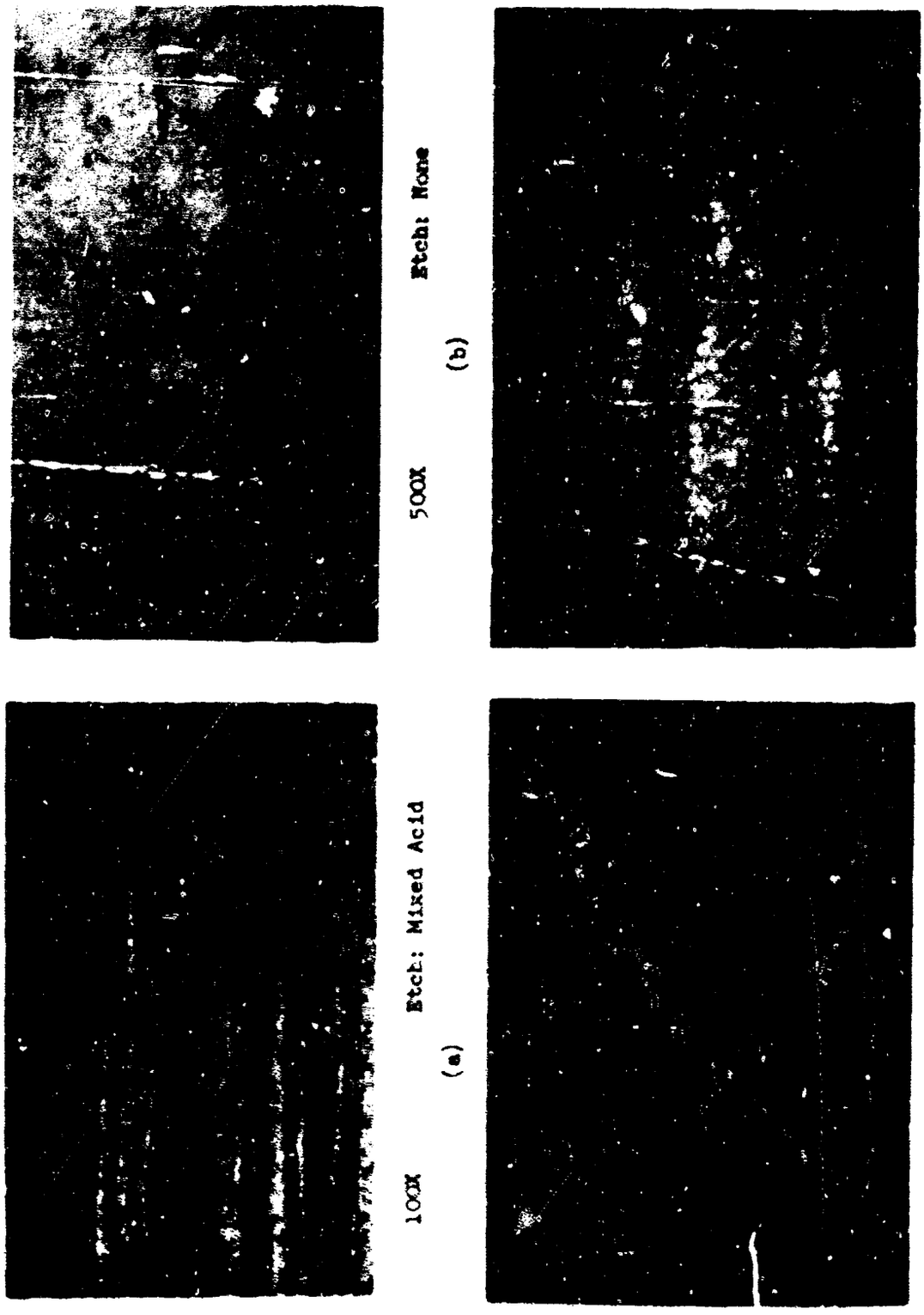

Figure 161 Photomicrographs Showing the Association of the Cracks with (a) Banding and (b), (c) and (d) Stringers of Secondary Phase Particles in Sample 5

100X Etch: Mixed Acid

(a)

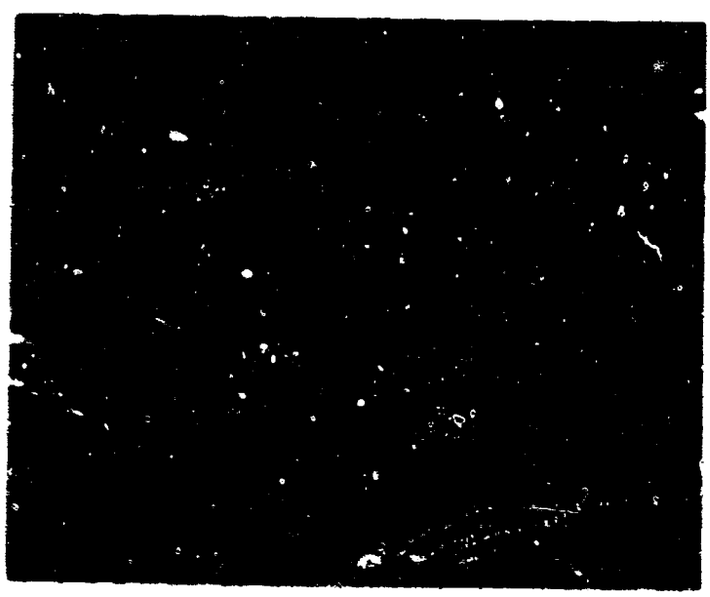

500X Etch: Mixed Acid

(b)

Figure 162 Photomicrographs Showing the Association of the Cracks with (a) Banding and (b) Stringers of Secondary Phase Particles in Sample 7

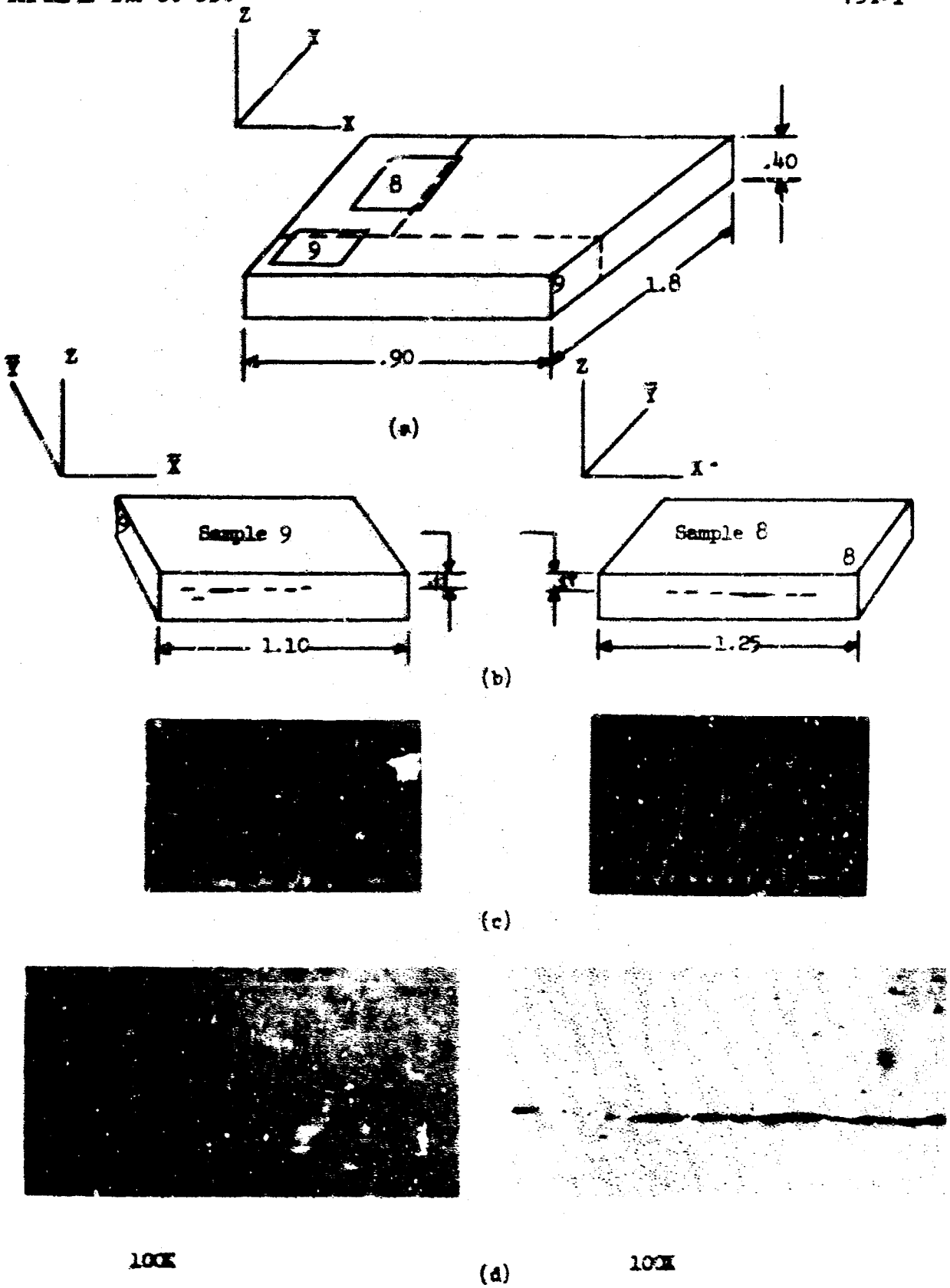

Figure 163 "Lead-Off" Page for Combination Sample 8 and 9 Showing (a) a Sketch of the Sample, (b) Sketches of the Sectioned Metallographic Samples, (c) an Oscillographic Display of the Defects, and (d) Photomicrographs of the "Most Open" Portion of the Crack in Samples 9 and 8, Respectively

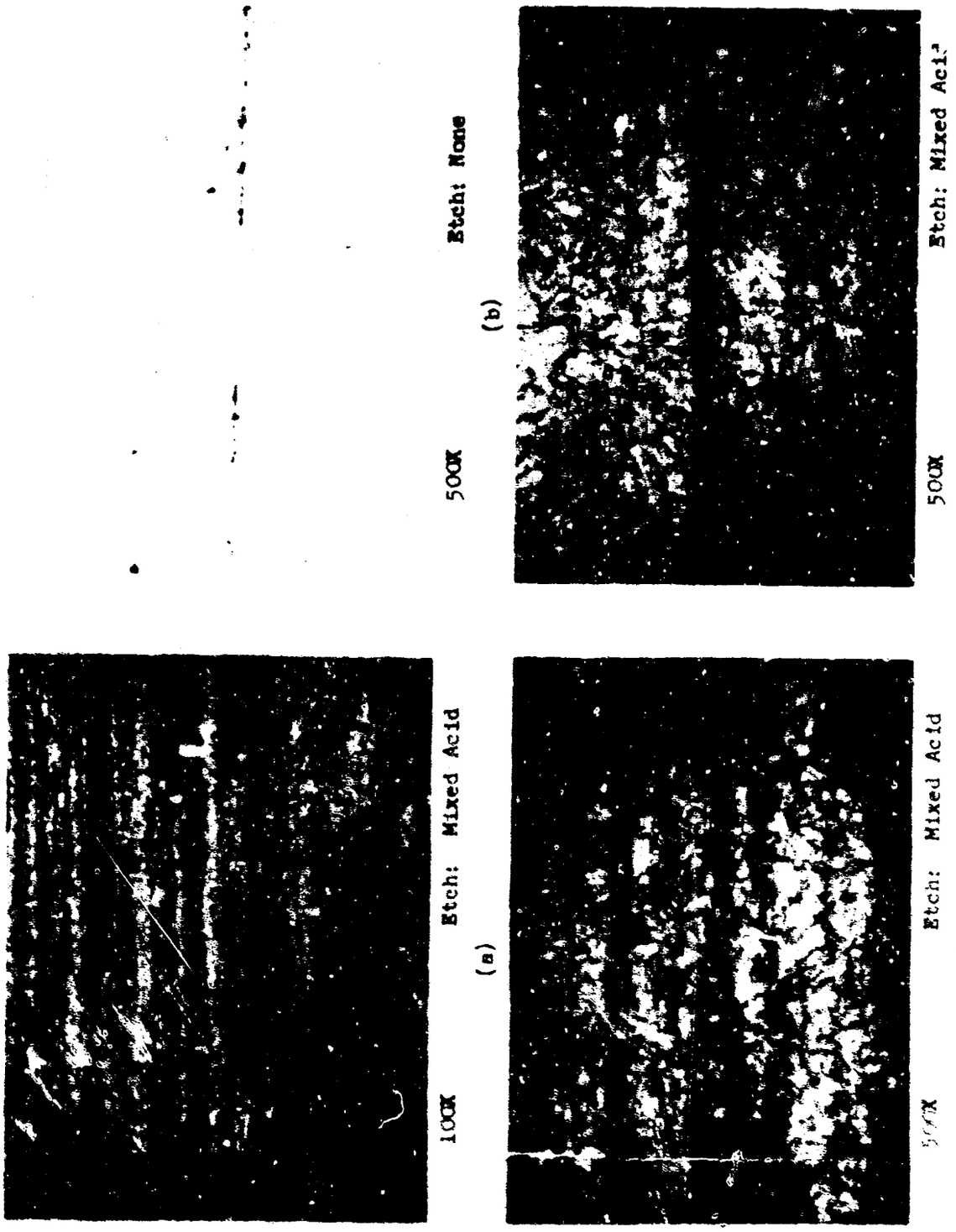

Figure 164 Photomicrographs Showing the Association of the Cracks with (a) Banding and (b), (c) and (d) Stringers of Secondary Phase Particles in Sample 9

LOCKHEED PROPULSION CORP

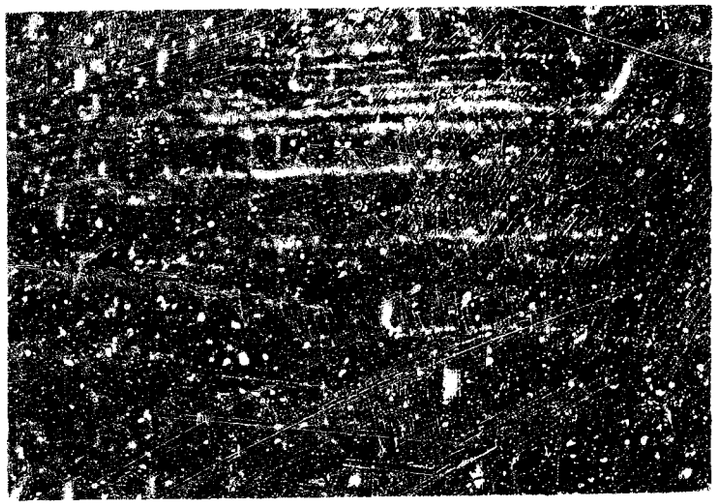

100X Etch: Mixed Acid

(a)

500X Etch: None

(b)

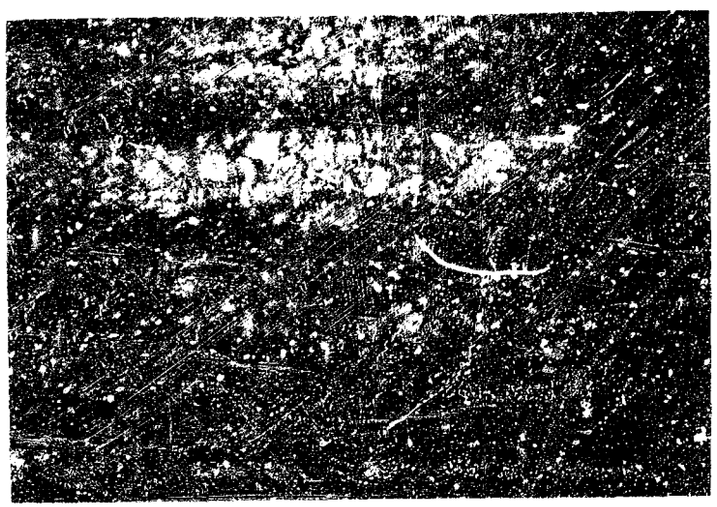

50X Etch: Mixed Acid

(c)

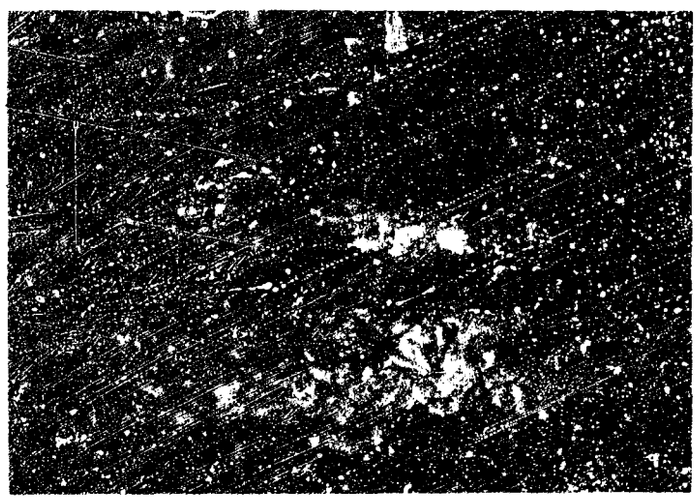

500X Etch: Mixed Acid

(d)

Figure 165 Photomicrographs Showing the Association of the Cracks with (a) Banding and (b), (c), and (d) Stringers of Secondary Phase Particles in Sample 8

LOCKHEED PROPULSION COMPANY

SECTION VIII

CASE CUTTING BY LINEAR SHAPED CHARGE

The motor case forward section was cut for scrap with linear shaped charges procured from Jet Research Center, Inc., of Arlington, Texas. Figure 166 illustrates the charge arangement. The 600 gr/ft charge was sufficient for obtaining a clean cut of the chamber, although the joint sections were precut by torch since the charge density was considered marginal for these regions. Charge stand-off distance was one-half inch. Figure 167 (1, 2, 3 and 4) depicts the cutting operation.

The motor case aft segment was cut up using a conventional cutting torch.

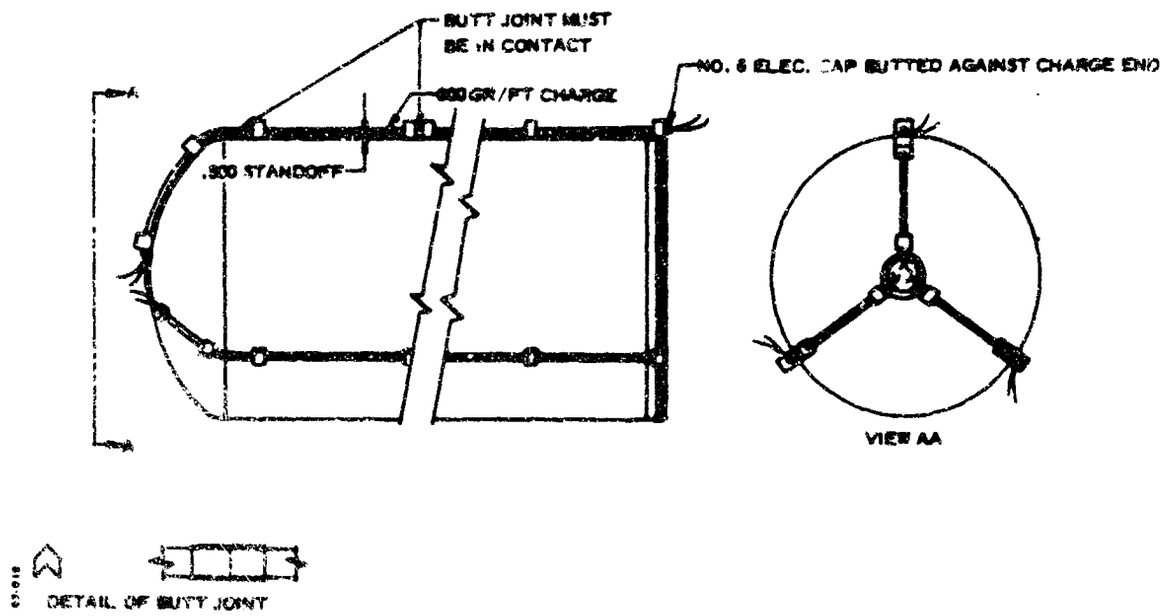

Figure 166 Sketch Showing Mounting of Linear Shaped Charge

Figure 157 Motor Case Forward Section Cuting Operation

APPENDIX

BOLT STRESS ANALYSIS

Lockheed Propulsion Company's Shell of Revolution Computer Program No. 124 was utilized for the bolt analysis. It performs an axisymmetric discontinuity stress analysis by formulating the equations for radial deflection and rotation in terms of internal pressure and the unknown bending moments and shears. Input for the program consists of a group of idealized geometric configurations such as cylinders, cones or elliptical elements, which comprise the basis of the design. The program equates at each end (cut) of these structural elements the respective equations for deflection and rotation and solves these equations for the discontinuity loads. The computer then calculates the rotations, deflections, and meridional and circumferential stresses at the inner and outer surfaces of the structural elements. This method of analysis is used primarily where discontinuities occur due to changes in the longitudinal geometry of the shell.

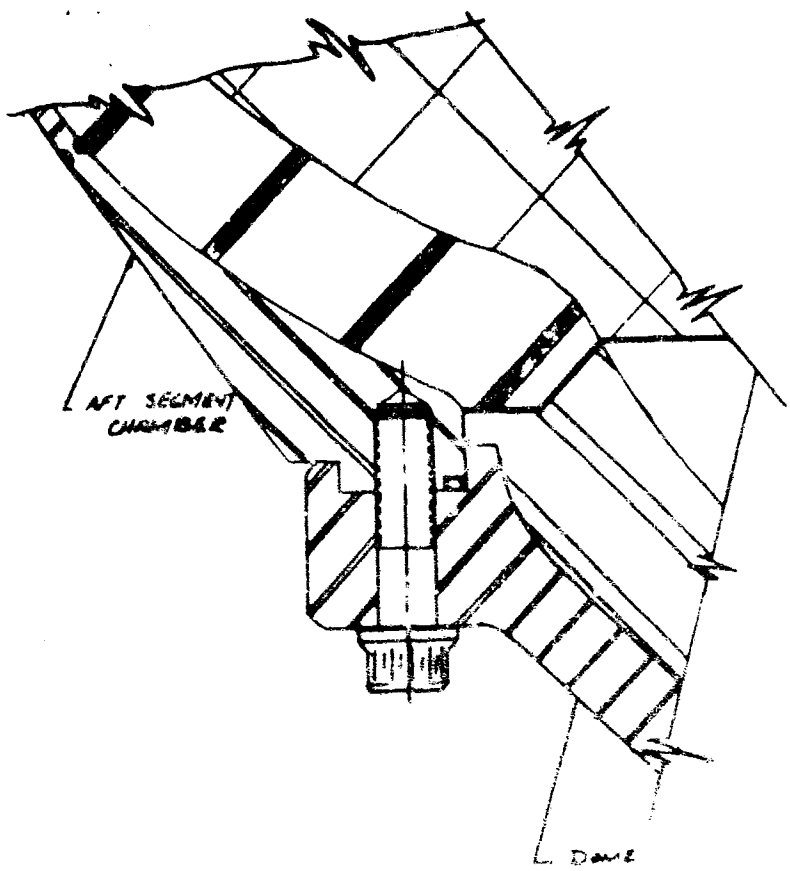

BOLT DETAIL

UNF $\frac{3}{4}$-16 -200 BRO'D

CHAMBER BOSS

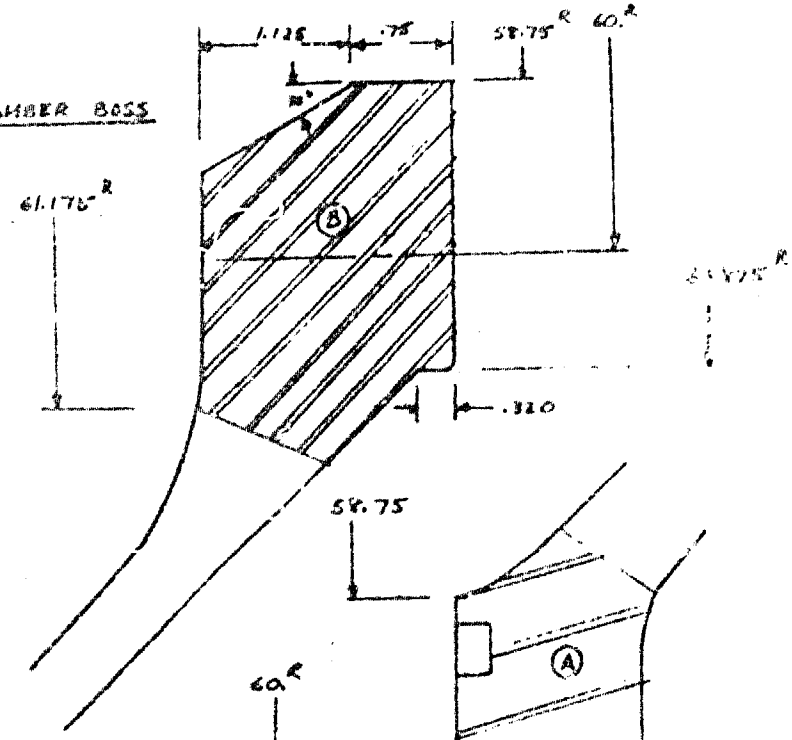

ADAPTER BOSS

ADAPTER BOSS, (A)

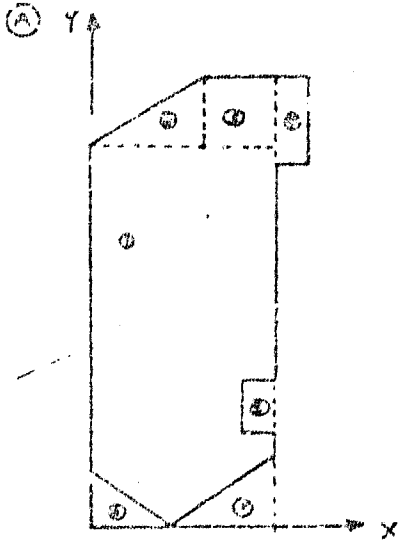

Ele #	Dimensions, x,y	x	Y	Area, A, in²	Ax	Ax²	Ay	I_{xy}
1	1.880 × 2.870	.640	1.420	3.7[illegible]70	2.78425	1.88573	5.56506	.62197
2	.840 × .905	.210	2.902	.26370	.11487	.06398	.41181	.04777
3	.840 × .785	1.110	3.093	.26190	.29071	.32268	.80979	.03615
4	.880 × .864	1.220	2.913	.[illegible]	.28642	.43821	.56403	.04190
5	.280 × [illegible]	1.277	1.424	-.[illegible]	-.09260	-.11824	-.07484	-.00045
6	.500 × .420	.200	.140	-.12600	-.02520	-.00504	-.01764	-.00252
7	.780 × .470	1.120	.140	-.22230	-.24889	-.27885	-.03112	-.00251
	Summation, Σ			4.15119	2.42867	2.28867	7.42523	8.42743

$$\bar{x} = \frac{\Sigma Ax}{\Sigma A} = \frac{2.42867}{4.15119} = .72969 \text{ in.}$$

$$\bar{y} = \frac{\Sigma Ay}{\Sigma A} = \frac{7.42523}{4.15119} = 1.789 \text{ in.}$$

$$I_{yy} = I_{xy} + \Sigma Ax^2 - \Sigma A(\bar{x})^2 = .42743 + 2.28867 - 4.15119(.72969)^2 = .704 \text{ in}^4$$

$$k_{c.g.} = 59.964 \text{ in.}$$

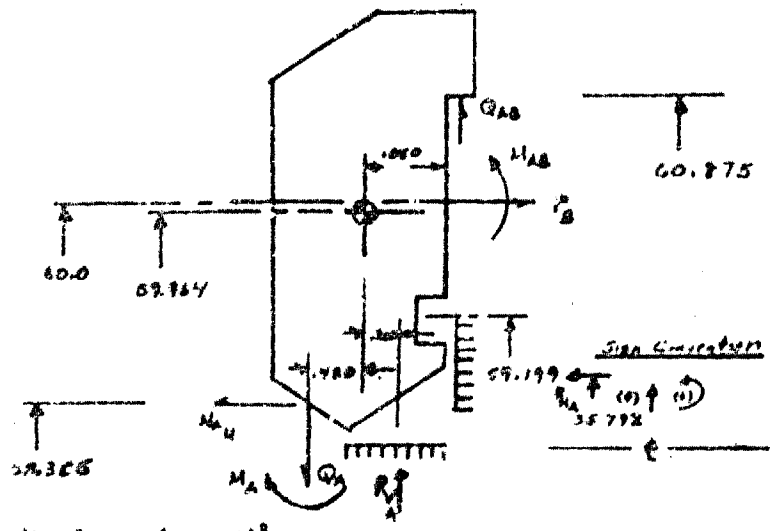

Let: $P_B = \frac{\pi(59.199)^2}{4\pi(60.0)}(1078) = 30,314$ lb/in.

$N_{A_H} = \frac{1078(58.365)}{2} = 30,302$ lb/in.

$P_{H_A} = 1078(59.199 - 58.365) = 895$ lb/in.

$P_{V_A} = 1078(.780) = 810$ lb/in.

$\Sigma M_{c.g.} = -\frac{58.365}{59.964}(30,302)(1.879) + \frac{59.960}{59.964}(810)(.020)$

$- \frac{35.792}{59.964}(895)(1.178) - \frac{60.000}{59.964}(30,314)(1.016)$

$\Sigma M_{c.g.} = -96,487 + 202 - 971 - 1,092 = -98,445$ in-lb/in.

$\Sigma P_{c.g.} = \frac{59.199}{59.964}(895) = 828.5$ lb/in.

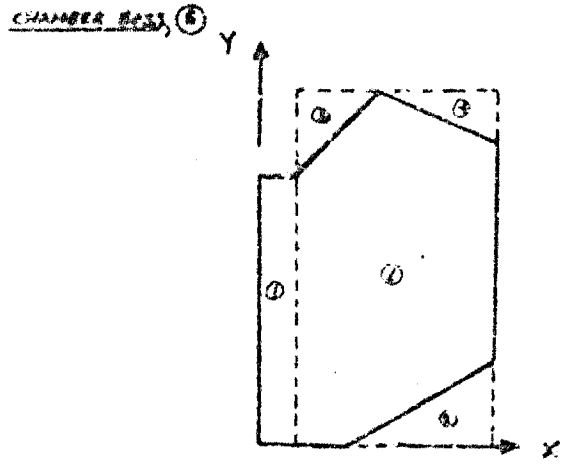

Elem.	Dimensions, x, y	x	y	Area, A, in²	Ax	Ax²	Ay	I_{xy}
(1)	.320 × 2.165	.160	1.083	0.69280	.11080	.01741	.75384	.00550
(2)	1.698 × 2.620	1.098	1.495	4.43175	4.86626	5.34973	6.31824	.89100
(3)	.600 × .700	.840	1.268	.21000	.17640	.25678	.26718	.00920
(4)	.916 × .400	1.857	2.717	.19160	.35599	.66302	.51835	.00947
(5)	1.126 × .650	1.600	.217	.36563	.58502	.93605	.07934	.01870
Summation, Σ				4.34512	4.01394	4.01799	5.73161	.95933

$\bar{x} = \frac{\Sigma Ax}{\Sigma A} = \frac{4.01394}{4.34512} = .92518$ in.

$\bar{y} = \frac{\Sigma Ay}{\Sigma A} = \frac{5.90261}{4.34512} = 1.358$

$I_{yy} = .95933 + 4.01799 - 4.34512(.92518)^2 = 1.158$ in⁴

$R_{c.g.} = 60.108$ in.

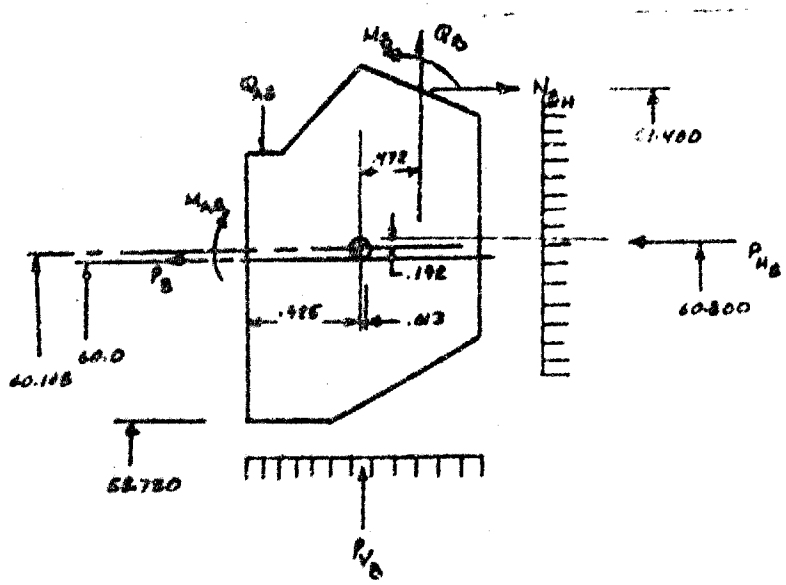

$P_B = 30,314$ lb/in.

$N_{BH} = \frac{1038(61.490)}{2} = 31,866.6$ lb/in.

$P_{H_B} = 1038(61.490 - 59.198) = 2,384.6$ lb/in.

$P_{V_B} = 1038(1.875) = 1,946.2$ lb/in

$$\Sigma M_{c.g.} = \frac{58.750}{60.108}(1,946.8)(.015) - \frac{60.001}{60.108}(30,314)(.108) + \frac{60.800}{60.108}(2,384.6)(.192) - \frac{61.490}{60.108}(31,866.6)(1.372)$$

$\Sigma M_{c.g.} = 24.7 - 3,2680 + 440.0 - 45,311.8 = -48,115.1$ in-lb/in.

$\Sigma Q_{c.g.} = \frac{58.750}{60.108}(1,946.8) = 1,902.3$ lb/in

FROM IBM COMPUTER OUTPUT DATA

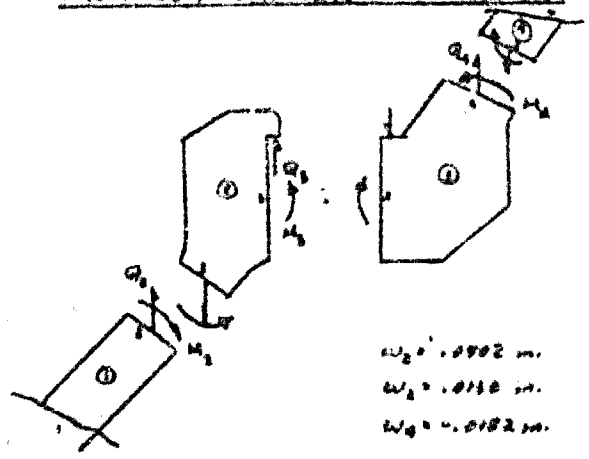

$w_2 = .0992$ in. $\theta_2 = -.0264$ rad.

$w_3 = .0118$ in. $\theta_3 = -.0124$ rad.

$w_4 = -.0182$ in. $\theta_4 = -.0224$ rad.

$Q_2 = 37,256$ lb/in $M_2 = 2,972.3$ in-lb/in

$Q_3 = 37,379$ lb/in $M_3 = 5,287.9$ in-lb/in.

$Q_4 = 36,825$ lb/in $M_4 = 2,810.3$ in-lb/in

Bolt Spacing $= \frac{2\pi R}{n} = \frac{2\pi(60)}{256} = 1.472$ in./bolt

Basic Bolt load $= 30,314$ lb/in. (1.472) in/bolt $= 44,625$ lb/bolt

Additional bolt load due to Interface Loads, P_D

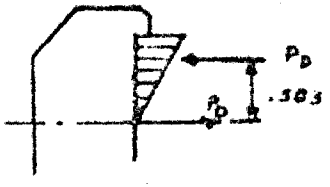

LOCKHEED PROPULSION COMPANY

$.585\ P_D = 5,537.9$

$P_D = 9,499.0$ lb/in or 13,975 lb/bolt

Total Bolt Load = 44,625 + 13,985 = 58,610 lb/bolt

$k = \frac{58,610}{44,625} = 1.313$

3/8 - 16 UNF BOLT

$F_{tu} = 260,000$ PSI (REF. 6)

$= 260,000 \times 0.395\ in^2$

$= 103,000$ lb/BOLT

3/8 - 16 UNF
BASIC MINOR DIA
= 0.7016 in
AREA = 0.396 in^2

$M.S. = \frac{103,000}{58,610} - 1$

$= \underline{0.76}$

c. Pin Joint Analysis

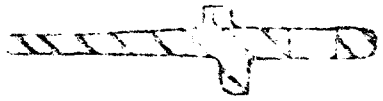

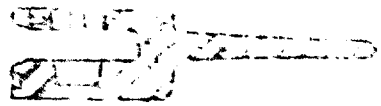

PIN JOINT, 156-INCH
DIAMETER MOTOR

Section Modulus at full cross section

$$Z = \frac{0.75)(0.25)^2}{6} = .00781 \quad in^3$$

$$M_y = (35 \times 10^3)(.00781) = 273 \text{ in lb}$$

$$M_{max} = (1.5 \cdot (55 \times 10^3) \cdot .00781) = 644 \text{ in lb}$$

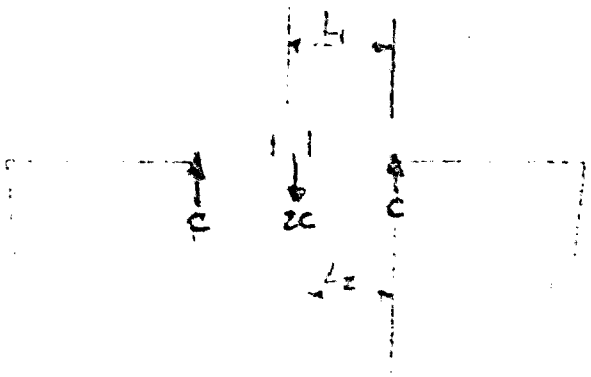

$L_1 = .680$

$L_2 = .680 - 218 = .462$

$$C = \frac{M}{L}$$

Minimum values based on strength of clamp at hole no bolt from hole

$$C_{y\,min} = \frac{M_y}{L_1} = \frac{114}{.680} = 168 \text{ lb}$$

$$C_{ult\,min} = \frac{M_{ult}}{L_1} = \frac{269}{.680} = 396 \text{ lb}$$

Maximum values based on strength of clamp at full cross section

$$C_{y\,max} = \frac{M_y}{L_2} = \frac{273}{.462} = 591 \text{ lb}$$

$$C_{ult\,max} = \frac{M_{ult}}{L_2} = \frac{396}{.462} = 857 \text{ lb}$$

Strength of 1/8 - 24 cap screw (assume f_{tu} = 200 [illegible]

$$F_{ult} = f_{tu} \cdot \frac{D^2}{4} = (200 \times 3)\pi \frac{.1200^2}{4} = 2280 \text{ lb} \quad (C_{ult} = 2040 \text{ lb}$$

LOCKHEED PROPULSION COMPANY

$\sin\alpha = .087156$
$\cos\alpha = .996219$ $\tan\alpha = .087489$

μ	sin-phase	cos-phase	C
0	.087156	.996219	1.106
0.05	.037546	1.00055	5511
0.07	.017423	1.00289	2604
0.075	.012843	1.00273	1859
0.080	.007461	1.00316	1114
0.085	.002430	1.00360	370
$\tan\alpha$	0		0

STRENGTH OF CLAMP 0.75 × 5.25 thick (.437 ø hole)

MATERIAL: SAE 1010 - 1020 (Dry [illegible])

Assume $F_{ty} = 35000$ psi (higher yield [illegible])

$F_{tu} = 55000$ psi

Section modulus at hole

$$Z = \frac{bd^2}{6} = \frac{(0.313)(0.75)^2}{6} = .00326 \text{ in}^3$$

Bending Moment to initiate yield (neglecting residual at cap [illegible])

$$M_y = F_{ty} Z = (35\times10^3)(.00326) = 114 \text{ in. lb.}$$

Maximum moment resistance (full plastic hinge at hole)

$$M_{max} = (F_{tu} Z)(1.5) = (55\times10^3)(.00326)(1.5) = 269 \text{ in. lb}$$

Best Available Copy

LOCKHEED PROPULSION COMPANY

156" HYDROBUCKET

PIN JOINT

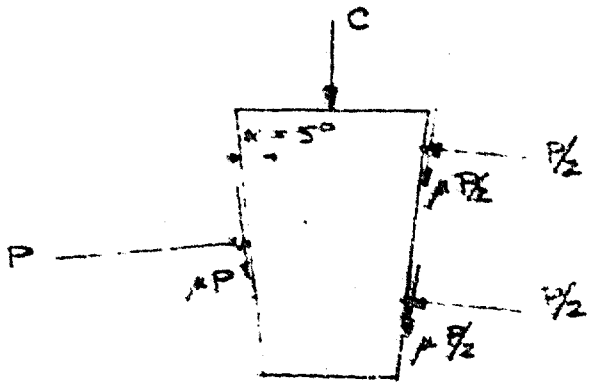

At 800 psi

Meridional load/pin (W = 200 pins)

$$H = \frac{p \pi R^2}{N}$$

$$H = \frac{800 \pi 77.255^2}{200} = \underline{74400 \text{ lb/pin}}$$

The normal force on the pin P =

$$P = \frac{H}{\cos\alpha + \mu \sin\alpha}$$

Summing Radial forces (neglecting reaction normal to contact of C)

$$C = 2P\sin\alpha - 2\mu P\cos\alpha$$

or

$$C = \frac{2H(\sin\alpha - \mu\cos\alpha)}{\cos\alpha + \mu\sin\alpha}$$

Best Available Copy

Unclassified
Security Classification

DOCUMENT CONTROL DATA - R&D
(Security classification of title, body of abstract and indexing annotation must be entered when the overall report is classified)

1. ORIGINATING ACTIVITY (Corporate author)
Lockheed Propulsion Company
A Division of Lockheed Aircraft Corporation
P.O. Box 111, Redlands, California

2a. REPORT SECURITY CLASSIFICATION
Unclassified

2b. GROUP

3. REPORT TITLE
156-Inch Diameter Maraging Steel Case Hydroburst and Materials Evaluation

4. DESCRIPTIVE NOTES (Type of report and inclusive dates)
Final Report, Covering period March 1966 through December 1966

5. AUTHOR(S) (Last name, first name, initial)
Coverdale, J.S., Wells, Norbert, Skopp, Gilbert, and Broker, George

6. REPORT DATE
January 1967

7a. TOTAL NO. OF PAGES
152

7b. NO. OF REFS
3

8a. CONTRACT OR GRANT NO.
AF 04(611)-11615

b. PROJECT NO.

c.

d.

9a. ORIGINATOR'S REPORT NUMBER(S)
LPC Report No. 751-F

9b. OTHER REPORT NO(S) (Any other numbers that may be assigned this report)

10. AVAILABILITY/LIMITATION NOTICES
CPIA Distribution

11. SUPPLEMENTARY NOTES

12. SPONSORING MILITARY ACTIVITY
Air Force Rocket Propulsion Laboratory
Research and Technology Division
Air Force Systems Command
United States Air Force, Edwards, Calif.

13. ABSTRACT
Activities in the hydroburst of a previously fired 156-inch diameter, maraging steel motor case are described. The program encompassed discontinuity stress analysis of the large, welded vessel, an evaluation of ultrasonic inspection methods by post-test sectioning, and a detailed failure analysis. The water-filled motor case, consisting of forward and aft case segments joined by a tapered pin joint, was pressurized from a gaseous-nitrogen source through a water accumulator. At 800 psi, 85 percent of the planned cyclic pressure level, the nozzle adapter-to-case bolts failed; secondary origins were found in the pin joint and the nozzle adapter forging. Concurrent examinations of the previously used bolts by LPC, Mellon Institute, and SPS Laboratories agreed in findings of evidence of stress corrosion in the 260,000-psi strength level H-11 bolts. The discontinuity stress analysis showed a forty percent indicated stress riser around the longitudinal welds caused by "sea-gulling" contour deviations. These findings were based on the use of a finite element, non'inear plane stress computer routine modified from a program written by Dr. L. R. Herrmann. Shear wave ultrasonic testing methods proved effective in detecting and defining parent metal and weld deposit flaws.

DD FORM 1 JAN 64 1473

Unclassified
Security Classification

Unclassified
Security Classification

14. KEY WORDS	LINK A ROLE	LINK A WT	LINK B ROLE	LINK B WT	LINK C ROLE	LINK C WT
156-inch diameter Maraging Steel Case						
Hydroburst						
Pre-test evaluation						
Post-burst analysis						
Nozzle adapter bolts						
Strain gage data						
Microstructure						
Tensile tests						
Hydrostatic test methods						
Discontinuity stress analysis						
Calculated stress and measured stress						

INSTRUCTIONS

1. ORIGINATING ACTIVITY: Enter the name and address of the contractor, subcontractor, grantee, Department of Defense activity or other organization *(corporate author)* issuing the report.

2a. REPORT SECURITY CLASSIFICATION: Enter the overall security classification of the report. Indicate whether "Restricted Data" is included. Marking is to be in accordance with appropriate security regulations.

2b. GROUP: Automatic downgrading is specified in DoD Directive 5200.10 and Armed Forces Industrial Manual. Enter the group number. Also, when applicable, show that optional markings have been used for Group 3 and Group 4 as authorized.

3. REPORT TITLE: Enter the complete report title in all capital letters. Titles in all cases should be unclassified. If a meaningful title cannot be selected without classification, show title classification in all capitals in parenthesis immediately following the title.

4. DESCRIPTIVE NOTES: If appropriate, enter the type of report, e.g., interim, progress, summary, annual, or final. Give the inclusive dates when a specific reporting period is covered.

5. AUTHOR(S): Enter the name(s) of author(s) as shown on or in the report. Enter last name, first name, middle initial. If military, show rank and branch of service. The name of the principal author is an absolute minimum requirement.

6. REPORT DATE: Enter the date of the report as day, month, year; or month, year. If more than one date appears on the report, use date of publication.

7a. TOTAL NUMBER OF PAGES: The total page count should follow normal pagination procedures, i.e., enter the number of pages containing information.

7b. NUMBER OF REFERENCES: Enter the total number of references cited in the report.

8a. CONTRACT OR GRANT NUMBER: If appropriate, enter the applicable number of the contract or grant under which the report was written.

8b, 8c, & 8d. PROJECT NUMBER: Enter the appropriate military department identification, such as project number, subproject number, system numbers, task number, etc.

9a. ORIGINATOR'S REPORT NUMBER(S): Enter the official report number by which the document will be identified and controlled by the originating activity. This number must be unique to this report.

9b. OTHER REPORT NUMBER(S): If the report has been assigned any other report numbers *(either by the originator or by the sponsor)*, also enter this number(s).

10. AVAILABILITY/LIMITATION NOTICES: Enter any limitations on further dissemination of the report, other than those imposed by security classification, using standard statements such as:

(1) "Qualified requesters may obtain copies of this report from DDC."

(2) "Foreign announcement and dissemination of this report by DDC is not authorized."

(3) "U. S. Government agencies may obtain copies of this report directly from DDC. Other qualified DDC users shall request through _____."

(4) "U. S. military agencies may obtain copies of this report directly from DDC. Other qualified users shall request through _____."

(5) "All distribution of this report is controlled. Qualified DDC users shall request through _____."

If the report has been furnished to the Office of Technical Services, Department of Commerce, for sale to the public, indicate this fact and enter the price, if known.

11. SUPPLEMENTARY NOTES: Use for additional explanatory notes.

12. SPONSORING MILITARY ACTIVITY: Enter the name of the departmental project office or laboratory sponsoring *(paying for)* the research and development. Include address.

13. ABSTRACT: Enter an abstract giving a brief and factual summary of the document indicative of the report, even though it may also appear elsewhere in the body of the technical report. If additional space is required, a continuation sheet shall be attached.

It is highly desirable that the abstract of classified reports be unclassified. Each paragraph of the abstract shall end with an indication of the military security classification of the information in the paragraph, represented as *(TS)*, *(S)*, *(C)*, or *(U)*.

There is no limitation on the length of the abstract. However, the suggested length is from 150 to 225 words.

14. KEY WORDS: Key words are technically meaningful terms or short phrases that characterize a report and may be used as index entries for cataloging the report. Key words must be selected so that no security classification is required. Identifiers, such as equipment model designation, trade name, military project code name, geographic location, may be used as key words but will be followed by an indication of technical context. The assignment of links, rules, and weights is optional.

Unclassified
Security Classification